



**HAL**  
open science

# Atomistic modeling of metallic nanoparticles on carbonaceous substrates and epitaxial graphene on metals

Georg Daniel Förster

► **To cite this version:**

Georg Daniel Förster. Atomistic modeling of metallic nanoparticles on carbonaceous substrates and epitaxial graphene on metals. Theoretical and/or physical chemistry. Université Claude Bernard - Lyon I, 2015. English. NNT : 2015LYO10150 . tel-01229111

**HAL Id: tel-01229111**

**<https://theses.hal.science/tel-01229111>**

Submitted on 16 Nov 2015

**HAL** is a multi-disciplinary open access archive for the deposit and dissemination of scientific research documents, whether they are published or not. The documents may come from teaching and research institutions in France or abroad, or from public or private research centers.

L'archive ouverte pluridisciplinaire **HAL**, est destinée au dépôt et à la diffusion de documents scientifiques de niveau recherche, publiés ou non, émanant des établissements d'enseignement et de recherche français ou étrangers, des laboratoires publics ou privés.

---

# Modélisation atomique de nanoparticules métalliques sur substrats carbonés et graphène épitaxié sur métaux

---

THÈSE DE L'UNIVERSITÉ DE LYON

Délivrée par

L'UNIVERSITÉ CLAUDE BERNARD LYON 1

École doctorale 52

Physique et Astrophysique de Lyon

DIPLÔME DE DOCTORAT  
en Physico-Chimie Théorique  
(arrêté du 7 août 2006)

soutenue publiquement le 30 septembre 2015

par

M FÖRSTER Georg Daniel

**Directeurs de thèse :**

Dr. Florent CALVO (LiPhy Grenoble)

Dr. Franck RABILLOUD (ILM Lyon)

---

**Jury :**

Président :

Prof. David RODNEY (ILM Lyon)

Rapporteurs :

Dr. Magali BENOIT (CEMES-CNRS Toulouse)

Dr. Johann CORAUX (Institut Néel Grenoble)

Examineurs :

Dr. Christophe BICHARA (CINAM Marseille)

Dr. Marie-Laure BOCQUET (ENS Paris)

Dr. Florent CALVO (LiPhy Grenoble)



# UNIVERSITE CLAUDE BERNARD - LYON 1

## Président de l'Université

Vice-président du Conseil d'Administration

Vice-président du Conseil des Etudes et de la Vie Universitaire

Vice-président du Conseil Scientifique

Directeur Général des Services

**M. François-Noël GILLY**

M. le Professeur Hamda BEN HADID

M. le Professeur Philippe LALLE

M. le Professeur Germain GILLET

M. Alain HELLEU

## **COMPOSANTES SANTE**

Faculté de Médecine Lyon Est – Claude Bernard

Faculté de Médecine et de Maïeutique Lyon Sud – Charles  
Mérieux

Faculté d'Odontologie

Institut des Sciences Pharmaceutiques et Biologiques

Institut des Sciences et Techniques de la Réadaptation

Département de formation et Centre de Recherche en Biologie  
Humaine

Directeur : M. le Professeur J. ETIENNE

Directeur : Mme la Professeure C. BURILLON

Directeur : M. le Professeur D. BOURGEOIS

Directeur : Mme la Professeure C. VINCIGUERRA

Directeur : M. le Professeur Y. MATILLON

Directeur : Mme. la Professeure A-M. SCHOTT

## **COMPOSANTES ET DEPARTEMENTS DE SCIENCES ET TECHNOLOGIE**

Faculté des Sciences et Technologies

Département Biologie

Département Chimie Biochimie

Département GEP

Département Informatique

Département Mathématiques

Département Mécanique

Département Physique

UFR Sciences et Techniques des Activités Physiques et Sportives

Observatoire des Sciences de l'Univers de Lyon

Polytech Lyon

Ecole Supérieure de Chimie Physique Electronique

Institut Universitaire de Technologie de Lyon 1

Ecole Supérieure du Professorat et de l'Education

Institut de Science Financière et d'Assurances

Directeur : M. F. DE MARCHI

Directeur : M. le Professeur F. FLEURY

Directeur : Mme Caroline FELIX

Directeur : M. Hassan HAMMOURI

Directeur : M. le Professeur S. AKKOUCHE

Directeur : M. le Professeur Georges TOMANOV

Directeur : M. le Professeur H. BEN HADID

Directeur : M. Jean-Claude PLENET

Directeur : M. Y. VANPOULLE

Directeur : M. B. GUIDERDONI

Directeur : M. P. FOURNIER

Directeur : M. G. PIGNAULT

Directeur : M. le Professeur C. VITON

Directeur : M. le Professeur A. MOUGNIOTTE

Directeur : M. N. LEBOISNE



## **Laboratoire d'accueil**

Institut Lumière Matière  
UMR5306 CNRS  
Université Claude Bernard Lyon 1  
Domaine Scientifique de La Doua  
Bâtiment Kastler, 10 rue Ada Byron  
69622 Villeurbanne CEDEX, France

---

## Résumé

Les applications des nanoparticules métalliques nécessitent la production d'assemblées mono-disperses et thermiquement stables sur un substrat. Des substrats carbonés tels que le graphène ou le graphite représentent des supports chimiquement inertes couramment utilisés. En particulier, le graphène en épitaxie sur métal (GEM) est étudié car il facilite l'auto-organisation des nanoparticules à sa surface. En effet, la différence entre les constantes de réseau du graphène et du métal conduit à un effet de moiré qui se traduit par la corrugation régulière du graphène sur une maille d'un ordre de grandeur plus grande que celle du graphène. Ce super-réseau comporte certaines régions privilégiées pour l'adsorption des nanoparticules. En fonction du support métallique, il existe une multitude de structures de moiré qui se différencient par leur taille, la déformation du graphène et la nature de l'interaction entre le métal et le graphène. Expérimentalement, des nanoparticules peuvent soit être déposées soit croître sur place par épitaxie par jets moléculaires.

Une monocouche de graphène en épitaxie peut conduire à la passivation chimique d'une surface métallique. Ces surfaces pourraient représenter un miroir pour des nouvelles techniques de microscopie basées sur des atomes ou molécules neutres. Des nanoparticules de métaux de transition habituellement en dépôt sur graphite mais aussi sur graphène ont des propriétés intéressantes en chimie de catalyse où le grand rapport surface sur volume de ces métaux rares est exploité : des nanoparticules de platine ont de nombreuses applications potentielles en catalyse, par exemple dans la technologie des piles à combustible où ils catalysent la réduction d'oxygène et l'oxydation d'hydrogène. Ces nanoparticules peuvent aussi augmenter la capacité de stockage d'hydrogène dans des milieux nano-poreux de carbone. De plus, des agrégats ferromagnétiques sont étudiés en vue de leur utilisation comme support d'enregistrement magnétique à haute densité. Cependant, toutes ces applications nécessitent en amont une compréhension fine des mécanismes physiques. Nous avons développé des modèles numériques permettant de simuler ces systèmes afin de comprendre à terme les mécanismes qui sont responsables de la formation d'un réseau de nanoparticules auto-organisées. A ce jour, les expériences sont largement basées sur l'empirisme et une compréhension détaillée de la physique prenant part dans ce système à température finie fait cruellement défaut. Ce travail est consacré surtout aux systèmes Ru-C et Pt-C où nous nous sommes intéressé au substrat du GEM nu, des agrégats du même métal y étant déposés, et des agrégats métalliques sur une surface de graphite. Quelques résultats concernant le système Ni-C seront également donnés ainsi qu'une discussion des difficultés particulières au système Ir-C.

Le potentiel à ordre de liaison de Brenner permet d'effectuer des études en dynamique moléculaire sur ce type de système. Couramment utilisé pour la description des semi-conducteurs et de carbone, mais aussi pour des métaux ainsi que des mélanges entre ce deux types d'atomes, ce potentiel tient compte de l'environnement local et des liaisons directionnelles. Dans le cas du système platine-carbone, nous basons les calculs sur une paramétrisation déjà existante. Cependant, pour le système Ru-C une paramétrisation dédiée était nécessaire. Pour ces deux systèmes la partie métallique du système est décrite par un potentiel basé sur l'approximation du deuxième moment dans le modèle des liaisons fortes (TB-SMA) dont une paramétrisation pour le Ru pur est disponible. Il a été montré que le TB-SMA peut être réécrit sous la forme du potentiel de Brenner, ce qui permet une description uniforme du système entier. Afin de trouver un jeu de paramètres pour les interactions Ru-C nous avons employé une approche à deux étapes : premièrement, une optimisation de paramètres avec un algorithme de Monte Carlo d'échange a été effectuée. Pendant cette procédure la fonction de coût à minimiser a contenu des géométries optimisées en théorie de la fonctionnelle de la densité (DFT) ainsi que l'énergie d'interaction de la couche de graphène ou des adsorbats éventuels. Dans une deuxième

---

étape les meilleurs jeux de paramètres ont été optimisés localement avec un algorithme de Levenberg-Marquardt, mais avec une fonction de coût raffinée comprenant des données concernant la géométrie et l'énergétique après optimisation structurale effectuée à chaque itération de l'algorithme. La même approche a été suivie pour la paramétrisation du champ de force pour le système Ir-C. Pour ce système, des calculs type DFT ont montré que le graphène n'est pas stable sur une surface Ir(111) sans prise en compte explicite de forces de dispersion et il s'avère qu'une description du graphène lié uniquement par physisorption faible représente une difficulté supplémentaire.

Basé sur l'approximation deuxième moment dans le modèle de liaisons fortes, le potentiel de Brenner néglige les interactions au-delà des premiers voisins, dont les forces de dispersion. Dans beaucoup de situations ces forces sont négligeables devant les liaisons chimiques traitées par ce potentiel interatomique. En revanche, à la surface d'un substrat étendu, elles contribuent d'une manière non-négligeable à l'énergie d'adsorption. Dans le cas du graphène sur Ru(0001) l'interaction est amplifiée d'un ordre de grandeur par l'interaction de dispersion. Bien qu'incluses conceptuellement dans les calculs de la structure électronique, les fonctionnelles d'échange-corrélation locales ou semi-locales courantes ne suffisent pas pour la description de forces de dispersion. Pour cette raison, plusieurs approches dédiées ont été développées afin de répondre à ce défaut. Les corrections de dispersion de Grimme modélisent empiriquement les interactions non-covalentes. La version D2 correspond à un potentiel de paires supplémentaire et la version D3 tient compte en outre de l'environnement local. Au niveau du temps de calcul, l'évaluation des forces de dispersion avec ces deux modèles est plus coûteuse que le calcul des forces covalentes et métalliques avec le potentiel de Brenner. Par conséquent nous avons cherché à développer une version implicite pour les forces non-covalentes. En s'inspirant des travaux de Steele, ce modèle gros grain basé sur le modèle D2 de Grimme exploite la géométrie du substrat qui consiste en une suite de couches presque planes et équidistantes. En négligeant la corrugation du substrat, nous intégrons rigoureusement la contribution d'une infinité de monocouches individuelles et ce sans introduire de paramètre supplémentaire. Ce modèle implicite décrit bien l'adsorption des agrégats sur graphite, or pour le graphène épitaxié les forces de dispersion issues de la partie métallique du substrat sont surestimées à cause des effets d'écrantage non pris en compte, pouvant néanmoins être importants car provenant d'électrons délocalisés. Pour combler ce problème nous avons suivi plusieurs approches tenant compte de ces effets empiriquement.

Basé sur ce champ de force nous montrons des propriétés statiques (structurales et énergétiques) à température nulle pour des nanoparticules de platine et de ruthénium sur substrats carbonés. Nous avons évalué le modèle implicite pour les forces de dispersion en comparant les calculs impliquant les modèles explicites Grimme D2 et D3. Par ailleurs, des comparaisons avec des calculs DFT avec ou sans traitement explicite de la dispersion montrent un bon accord. Des optimisations systématiques d'agrégats métalliques (Ru et Pt) réalistes (structures 2D et 3D de dizaines à milliers d'atomes) sur graphène et graphite ainsi que sur graphène en épitaxie sur métal [Pt(111) ou Ru(0001)] ont également été effectuées. Grâce à des simulations de dynamique moléculaire, la stabilité thermique des adsorbats ainsi que de la couche de graphène a été étudié dans le contexte de la dynamique vibrationnelle et de la diffusion globale. Le comportement thermique souligne ainsi le rôle clé des forces de dispersion pour la stabilité des adsorbats. Les propriétés vibrationnelles de graphène seul ou en contact avec le substrat métallique révèlent une forte sensibilité à la température et aux contraintes. En accord avec des expériences, la mobilité des adsorbats de ruthénium sur une surface de graphite a été trouvée très élevée. Le substrat du GEM a été étudié à température finie pour différentes commensurabilités [graphène/Ru(0001)] et différents angles entre le graphène et le réseau de la surface métallique [graphène/Pt(111)]. Ceci a rendu des comparaisons avec une multitude des

---

données expérimentales sur le GEM obtenues notamment par microscopie à force atomique ou diffraction des rayons X. Finalement, l'étude de l'effet de la température sur des adsorbats en dépôt sur graphène épitaxié a montré une grande stabilité vis-à-vis de la fusion et diffusion des agrégats par rapport à ceux en contact avec une surface de graphite.

**Mots clés:** Matériaux nanostructurés, Stabilité thermique des nanoparticules, Matériaux à base de carbone: graphène et graphite, Modélisation et simulations numériques, Diffusion d'agrégats

---

# Atomistic modeling of metallic nanoparticles on carbonaceous substrates and epitaxial graphene on metals

## Abstract

Applications of metal nanoparticles require the production of mono-dispersed assemblies that are thermally stable on a substrate. Because of their chemical inertness carbon substrates such as graphene or graphite are commonly used supports. In particular, epitaxial graphene on metal (GOM) facilitates the self-organization of nanoparticles on its surface. The lattice mismatch between graphene and the underlying metal surface leads to a moiré effect which results in the regular corrugation of the graphene leading to a nanomesh having a lattice constant one order of magnitude larger than that of graphene. This superlattice has certain areas, called registries, which favor the adsorption of nanoparticles. Depending on the metal support, there is a plethora of moiré structures that differ by their size, the deformation of the graphene and the nature of the interaction between the metal and the graphene. Experimentally, nanoparticles may be deposited onto this substrate or grown on site by molecular beam epitaxy.

A monolayer of epitaxial graphene can lead to chemical passivation of a metal surface. These surfaces may constitute a mirror for new microscopy techniques based on neutral atoms or molecules. Transition metal nanoparticles typically deposited on graphite, but also on graphene have interesting properties in catalyst chemistry where the large surface to volume ratio of these rare metals is exploited: platinum nanoparticles have many potential applications in catalysis in fuel cell technology where they catalyze oxygen reduction and hydrogen oxidation. These nanoparticles can also increase the hydrogen storage capacity of nanoporous carbon materials. In addition, ferromagnetic clusters may be used in high-density magnetic information storage technology. However, all these potential applications require a detailed understanding of the underlying physical mechanisms. We have developed numerical simulations to study these systems in order to understand the mechanisms that are responsible for the formation of a self-organized nanoparticle network. To date, experiments are only described empirically and a detailed understanding of the physics involved in this system at finite temperature is lacking. This work addresses the Ru-C and Pt-C systems by studying the bare GOM substrate, aggregates of the same metal deposited thereon and metal clusters on graphite surfaces. Some results concerning the Ni-C system are also presented, as well as a discussion of the specific difficulties related to the description of the Ir-C system.

The Brenner potential of bond order type allows performing molecular dynamics studies on this type of system. Commonly used for the description of semiconductors and carbon, but also for metals and mixtures of the two types of atoms, this model represents a bond-order potential that takes into account the local environment and directional bonding. In the case of the platinum-carbon system, we base the calculations on an existing parametrization. However, for the Ru-C system a customized parametrization was necessary. The metal part of the system is described by a potential based on the second-moment approximation in the tight-binding model (TB-SMA), where a parametrization for pure Ru is available in the literature. It has been shown that the TB-SMA can be rewritten under the form of the Brenner potential, which allows in turn a uniform description of the entire system. In order to find a parameter set for Ru-C interactions, we used a two-step approach: first, a parameter optimization was performed with the help of an exchange Monte Carlo algorithm. During this procedure the cost function to be minimized contained geometries obtained by density functional theory (DFT) calculations and

---

the interaction energy of the graphene layer or possible adsorbates. In the second step, the best parameter sets were optimized locally with a Levenberg-Marquardt algorithm on the basis of a refined cost function including geometric and energetic data of structural relaxations performed at each iteration of the algorithm. The same approach was followed for the parametrization of the force field for the Ir-C system. For this system, DFT calculations have shown that graphene is not stable on the Ir(111) surface without explicit account for dispersion forces and it turns out that graphene bound only by weak physisorption represents an additional difficulty for its description with a Brenner potential.

Based on the second-moment approximation in the tight-binding model, the Brenner potential neglects interactions beyond nearest neighbors and, therefore, long-ranged dispersion forces. In many situations, these forces are negligible compared to chemical bonds modeled by the Brenner potential. However, on the surface of an extended substrate, they contribute in a significant amount to the total adsorption energy. In the case of graphene on Ru(0001), the interaction is amplified by one order of magnitude by the dispersion interaction. Although conceptually included in electronic structure calculations, dispersion forces are not fully represented in local or semilocal exchange-correlation functionals. Several dedicated approaches have thus been developed to address this shortcoming. The Grimme dispersion corrections model empirically the non-covalent interactions. The D2 version is an additional pairwise potential and the D3 version takes into account also the local environment. The evaluation of the dispersion forces with these two models is computationally more intensive than the calculation of the bonding interactions with the Brenner potential. Therefore, we sought to develop a coarse-grained version for the description of non-covalent forces. Following the Steele approach, we base this coarse-grained model on the Grimme D2 dispersion correction and exploit the geometry of the substrate which consists of a sequence of almost flat and equidistant layers. Neglecting the corrugation of the substrate, we rigorously integrate the contribution of infinite individual monolayers and this without introducing additional parameters. This implicit model describes well adsorption of clusters on graphite, but in the case of epitaxial graphene, dispersion forces caused by the metal portion of the substrate are overestimated because of neglected screening effects due to delocalized electrons. To address this issue, we follow several approaches taking into account these effects empirically.

Using this model, we calculated static properties at zero temperature for platinum and ruthenium nanoparticles. We evaluated the implicit model for dispersion forces by comparing to calculations involving the explicit Grimme D2 and D3 model. Additional comparisons with DFT calculations with or without such explicit dispersion corrections show also good agreement. Systematic optimizations of realistic Ru and Pt clusters (2D and 3D structures of tens to thousands of atoms) on graphene and graphite as well as on epitaxial graphene on metal [Pt (111) and Ru (0001)] have been carried out. Using molecular dynamics simulations, the thermal stability of adsorbates and the graphene layer have been studied in the context of vibrational and diffusion dynamics. The thermal behavior underlines the key role of dispersion forces for the stability of the adsorbates. The vibrational properties of graphene alone or in contact with the metal substrate show a strong sensitivity to temperature and strain. In agreement with experiments, the mobility of ruthenium adsorbates on a graphite surface was found to be very high. The GOM substrate was studied at finite temperature for different moiré commensurabilities (graphene/Ru(0001)) and angles between the graphene and the metal surface lattice (graphene/Pt(111)). This allowed for comparisons with many experimental data on GOM obtained e.g. by atomic force microscopy or X-ray diffraction measurements. Finally, we studied the effect of temperature on adsorbates deposited on epitaxial graphene, where we found increased thermal stability against adsorbate melting and diffusion compared to clusters on a graphite surface.

---

**Keywords:** Nanostructured materials, Thermal properties of Nanoparticles, Carbon-based materials: graphene and graphite, Computer modeling and simulation, Diffusion of clusters

---

## Acknowledgements

The work of this thesis was carried out from October 2012 to September 2015 at the Institut Lumière Matière (ILM) in Lyon. I feel privileged for having had the opportunity of working there and wish to thank the successive directors, Christian Bordas and Marie-France Joubert.

First, I would like to thank Florent Calvo, the advisor of this thesis. He taught me a lot on many aspects of research, and I am very grateful for this knowledge of which I know that it will benefit me for a long time. Thanks to his impressive knowledge, he introduced me to a large variety of concepts and methods at ease. He also provided an excellent example for writing appealing scientific texts that I try to imitate as good as I can. I'm also indebted to Franck Rabilloud, who codirected this thesis. His advice was very encouraging and helpful. He always knew solutions to the worst problems that occurred to me during those last three years of research.

I also thank all the other members of the physical chemistry group for their kind welcome. Especially I would like to thank Abdul-Rahman Allouche for his help for all kinds of computer problems in the last three years, but also for his undergraduate informatics course that awakened my interest in numerical physics and for helping me to enter the Masters program. Many thanks also to Yann Magnin, who spent one year of postdoc in the physical chemistry group during which we shared many relaxed and enjoyable discussions and also a respectable number of pizzas. I am very happy to be able to spend now again some more time with him at CINaM in Marseille. A big thank you to Pierre Mignon, who contributed a great deal to make everyday work a lot more fun.

I would like to thank Jin Yu for initiating a nice research project on the formation of nanoparticles in a Laser ablation plume. I enjoyed working on this topic very much even if it is not part of this thesis.

A warm thank you also to our collaborators, Marie-Laure Bocquet kindly provided us with DFT reference data, which represent an essential prerequisite for this work. Thank you, Christophe Bichara for welcoming me one week at CINaM in Marseille and very fruitful discussions, especially on the screening of dispersion forces on a metal substrate. I am also grateful for giving me now the opportunity of a postdoc internship in his group in Marseille. I wish to thank Magali Benoit and Johann Coraux for their careful reading of this manuscript and the time and effort they put into this.

I would like to thank the PSMN (Pôle Scientifique de Modélisation Numérique) computing center of ENS de Lyon and its staff that made the calculations presented in this thesis possible.

Finally, I wish to thank family and friends for their support during this thesis, but also since a long time before. Thank you, Shangshang, for staying at my side and for your encouraging optimism.



# Contents

<b>Abbreviations</b>	<b>15</b>
<b>1 Introduction</b>	<b>17</b>
1.1 Nanoscience and metal nanoparticles (NPs)	17
1.2 Carbonaceous substrates	18
1.2.1 Graphene	19
1.2.2 Graphite	20
1.2.3 Epitaxial graphene on metal (GOM)	20
1.3 Commonly used modeling tools	22
1.3.1 Density functional theory (DFT)	22
1.3.2 Tight-binding model and empirical atomistic potentials	23
1.4 Outline of the manuscript	25
<b>2 Methodology</b>	<b>27</b>
2.1 TB second moment approximation	28
2.2 Brenner bond-order potential (BOP)	29
2.3 Brenner BOP and TB-SMA	30
2.4 Parametrization procedure	32
2.4.1 Problem of parameter optimization	32
2.4.2 Metropolis MC simulations in the canonical ensemble	33
2.4.3 Local optimization with MC simulations at zero temperature	34
2.4.4 Global optimization with parallel tempering Monte Carlo (PTMC) simulations	34
2.5 London dispersion forces	36
2.5.1 Grimme models	36
2.5.2 Implicit model for dispersion interactions	38
2.5.3 Intra-graphite dispersion interactions	40
2.5.4 Screening of dispersion forces on metal substrates	41
2.6 Simulation tools	42
2.6.1 Periodic boundaries	42
2.6.2 Moiré structures	43
2.6.3 Structural optimizations	45
2.6.4 Molecular dynamics	47
2.7 Observables	49
2.7.1 Lindemann indices and adsorbate shape	50
2.7.2 Surface diffusion coefficients and activation energy	50
2.7.3 Vibrational spectra	51

<b>3</b>	<b>The platinum-carbon system</b>	<b>53</b>
3.1	Introduction . . . . .	53
3.2	Computational details . . . . .	54
3.3	Pt NPs on pure carbon substrates . . . . .	55
3.3.1	Comparison of dispersion models: the adatom case . . . . .	55
3.3.2	Pt adatoms on defective graphite . . . . .	57
3.3.3	Interaction of larger adsorbates . . . . .	58
3.3.4	Comparison with DFT calculations . . . . .	60
3.3.5	Finite temperature dynamics of adsorbates on graphite . . . . .	61
3.4	NPs on epitaxial graphene/Pt(111) . . . . .	66
3.4.1	Modeling of supported graphene . . . . .	66
3.4.2	NPs on moiré substrates . . . . .	73
3.5	Conclusions . . . . .	74
<b>4</b>	<b>The ruthenium-carbon system</b>	<b>77</b>
4.1	Introduction . . . . .	77
4.2	Bond-order potential for Ru-C . . . . .	78
4.2.1	Parametrization . . . . .	79
4.2.2	Pauling relation . . . . .	80
4.2.3	Dispersion corrections . . . . .	82
4.3	Simulation details . . . . .	82
4.4	Results . . . . .	83
4.4.1	Static properties . . . . .	83
4.4.2	Finite temperature dynamics . . . . .	90
4.5	Conclusions . . . . .	98
<b>5</b>	<b>Other transition metal-carbon systems</b>	<b>101</b>
5.1	Iridium-Carbon systems . . . . .	101
5.1.1	Brenner BOP Ir-C parametrization . . . . .	101
5.1.2	Geometry of epitaxial graphene on Ir(111) . . . . .	105
5.1.3	Effect of temperature on graphene/Ir(111) . . . . .	106
5.2	Nickel-Carbon systems . . . . .	107
5.2.1	Tight-binding within the fourth moment approximation . . . . .	108
5.2.2	Simulation details . . . . .	110
5.2.3	Epitaxial graphene on Ni(111) . . . . .	110
5.2.4	Ni adsorbates on free and epitaxial graphene . . . . .	112
<b>6</b>	<b>General conclusion</b>	<b>115</b>
	<b>References</b>	<b>120</b>

# Abbreviations

AFM	atomic force microscopy
AES	atomic emission spectroscopy
BOP	bond-order potential
CN	coordination number
CTR	x-ray crystal truncation rod scattering
CVD	chemical vapor deposition
DFT	density functional theory
EAM	embedded atom model
EXRR	extended x-ray reflectivity
GGA	generalized gradient approximation
GOM	epitaxial graphene on metal
GPW	Gaussian and plane wave method
LDA	local-density approximation
LEED	low-energy electron diffraction
LJ	Lennard-Jones
MC	Monte Carlo
MD	molecular dynamics
MSD	mean square displacement
NP	nanoparticle
PAW	projector augmented wave method
PBE	Perdew-Burke-Ernzerhof
PTMC	parallel tempering Monte Carlo
RPA	random phase approximation
STM	scanning tunneling microscopy
SXRD	surface x-ray diffraction
TB	tight-binding
TB-FMA	tight-binding, fourth moment approximation
TB-SMA	tight-binding, second moment approximation
TEC	thermal expansion coefficient
TF	Thomas-Fermi



# Chapter 1

## Introduction

### 1.1 Nanoscience and metal nanoparticles (NPs)

Nanoscience deals with the production and analysis of nanoscaled systems. These are systems of typical sizes ranging from one up to hundreds of nanometers. These length scales may apply in one, two or three dimensions, such as in thin films, nanorods or nanoparticles (NPs), respectively. Commonly these materials consist of carbon [1–3], metals [4], semiconductors [5], oxides [6] or polymers [7]. The diversity in dimensionality, size, shape and composition of nanosystems allows for a vast scope of novel materials with unconventional properties. Nanosized objects may be created naturally during combustion, in volcanic eruptions or ocean spray [8]. The most complex nano-objects occur in biological systems for example in the form of proteins or viruses [9]. Without the awareness of their existence, NPs have been used since long time ago. For example gold NPs have been used in stained glass since the Roman ages [10]. Another example is carbon black that finds application as pigments in paints and inks [11]. More recent applications include titanium oxide NPs in sunscreens or paint, silver NPs for antimicrobial coatings [12] and nanostructured water and dirt repellent coatings [5]. Currently research is carried out on nano-composite high strength materials [2], NPs as catalysts [13] and a range of biomedical nanomaterials for targeted drug delivery, tissue engineering or biosensors [14], just to name a few potential applications. Research effort is also directed to the understanding and avoidance of nanosized air pollutants and the health and environmental impact of nanomaterials [8]. Nanoscience is about the understanding, characterization and deliberate elaboration of these materials.

Concerning the fabrication of NPs, two main approaches can be followed. First, starting of from the bulk material, the top-down methods reduce the object size. This can be achieved by milling and grinding, but also more sophisticated techniques such as laser ablation, photolithography or electron beam lithography fall into this category. The second approach relies on building up the nano-objects from their atomic constituents. This can be achieved by chemical synthesis in the liquid phase or chemical vapor deposition (CVD) on a substrate that possibly favors self-organization of NPs. The physical and chemical processes involved in the formation of NPs are subject of active research [15]. The aim is to gain control over the size and shape that determine other properties of the NPs as practical applications usually require the avoidance of coalescence and uniform sizes of the NPs.

A major interest in NPs originates from their distinct properties compared to the bulk material or single atoms, making them a distinctly new type of material. The properties of the NPs depend strongly on their size. This is the case for basic properties such as shape and stability, but also for optical effects (surface plasmon resonances), magnetic anisotropy or chemical activity, which is studied with the objective of rational catalyst design. Growth

and catalytic activity take place at the surface of the NPs and therefore at increased rates compared to the same mass of material in larger particles due to their high surface to volume ratio. Chemical activity is also influenced by the shape of the NPs and the nature of their surface. For example the (111) surface of platinum is several times more active than the (100) surface for the catalysis of aromatization reactions [16].

In the so-called scalable regime applicable to larger particles, properties such as interatomic distances and cohesive energies depend monotonically on the number of atoms and converge to the bulk values. For smaller particles, where the number of atoms at the surface is comparable to those at the inner part of the particle, quantum-mechanical effects become important and the dependency of the particles' properties follows non-monotonic trends with clusters size [13]. In particular, the chemical properties of lowly coordinated sites at the edges and corners of the particles gain relative importance. Noble gas or metallic clusters are found to form regular polyhedra built up by concentric atomic shells and thus contain certain preferred numbers of atoms known as magic numbers [13]. Using the Wulff construction, such regular NPs with well-defined crystal facets can be geometrically built by minimizing the surface Gibbs energy, which is assumed to be known for macroscopic crystal surfaces as a function of lattice planes. Conforming to the jellium model, other magic numbers occur in small alkali metal clusters where the electronic structure dominates and therefore high stability is found in the case of full electronic shells. In this model the electrons are delocalized over the entire cluster, while the atomic cores provide a uniform background of positive charge [13].

The range of properties of metallic NPs can be strongly increased by considering mixtures of different metals, referred to as nanoalloys. Their properties may be tuned via the composition and varying chemical ordering in addition to cluster size. Several types of structures can be identified according to their mixing patterns: Core-shell structures are composed of a core of a certain atomic species surrounded by a shell of atoms of another type. Additional shells may be added to form multi-shell nanoalloys with an onion-like structure. Mixed structures represent another type of nanoalloys where the different atomic species occupy random sites or follow ordered patterns similar to macroscopic alloys [17].

It should be noted that free NPs are idealizations from the experimental reality where these objects are produced in a solution or on a support and are possibly covered by stabilizing agents. Clearly, the environment may strongly affect the equilibrium structure of the NPs [18]. However this is not necessarily a drawback as the environment may be used to change the properties of the NPs in a controlled way. In addition, nano-patterned substrates may make the control over their size and shape more easy, help to avoid coalescence and even favor self-organization [19]. These ideas are the motivation for this work where we studied transition metal NPs deposited on carbonaceous substrates. In the next section, we give an overview of this class of substrates.

## 1.2 Carbonaceous substrates

The use of NPs for practical applications requires stabilizing them against thermal motion and protecting them against possible degradation and reactions due to the external medium, e.g. through appropriate coating with surfactant molecules. In surface science, the particles are either grown on the substrate from the atoms, or deposited after their initial formation in the gas phase [20–22]. Owing to their high versatility, relative chemical inertness and reasonable production costs, carbon materials are often employed as substrates for NP deposition [19, 23–28]. Even without NP decoration, these substrates represent an entire field of research. The following paragraphs briefly present the scope of these materials.

### 1.2.1 Graphene

Graphene is the two-dimensional allotrope of carbon where the atoms are arranged in a honeycomb lattice consisting of two equivalent triangular sublattices. The carbon-carbon bond length in graphene is  $1.42 \text{ \AA}$  [29]. Since it was shown to be obtainable by mechanical exfoliation of graphite [3], the material has attracted much research interest: On the one hand, graphene can be regarded as a model system in fundamental physics due to its linear dispersion relation in combination with its sublattice symmetry (amongst others). On the other hand graphene has also promising practical applications for example in nanosized ultrafast transistors [30]. Furthermore, graphene can be seen as the building block for a number of other ( $sp^2$ ) nanomaterials represented in Fig. 1.1. Graphite is built up by stacked graphene layers on top of each other. Carbon nanotubes can be understood as graphene rolled up into cylindrically shaped, one dimensional nano-objects consisting of one or several layers (single- and multi-walled nanotubes) [31]. They are superior in terms of stiffness, strength and resilience to any other current material and also have interesting electronic properties which can be either metallic or semi-conducting, depending on tube chirality [2]. Finally, buckminsterfullerenes also consist solely of  $sp^2$  hybridized carbon arranged in pentagonal and hexagonal rings [1].

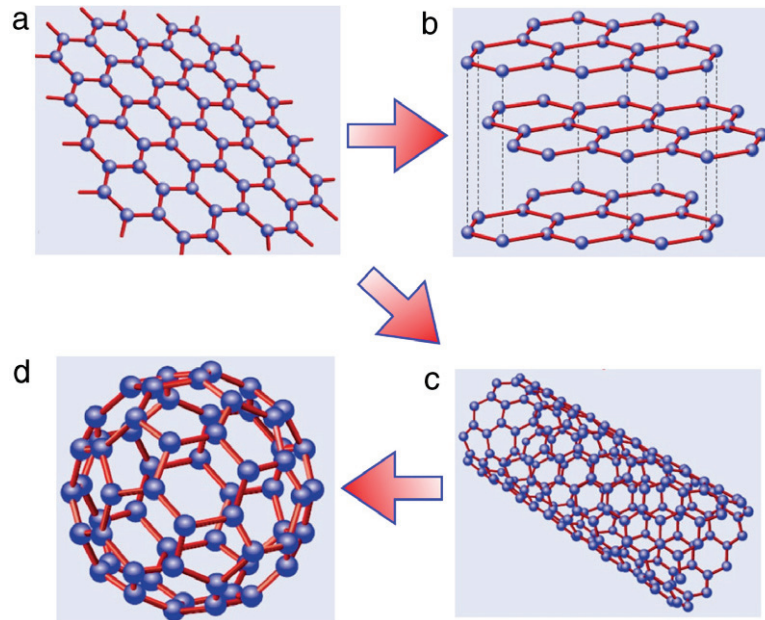


Figure 1.1: Graphene as the conceptual building block of other  $sp^2$  carbon allotropes: (a) graphene, (b) graphite, (c) carbon nanotube, (d) buckminsterfullerene. Figure from Tetlow and coworkers [32].

The graphene unit cell consists of two carbon atoms with four valence electrons each. Three of these electrons are  $sp^2$  hybridized and form in-plane  $\sigma$ -bonds with the three nearest carbon atom neighbors. The remaining two valence electrons in the unit cell (one for each of the mentioned sublattices) are delocalized into a bonding  $\pi$  and an anti-bonding  $\pi^*$  band (valence and conduction band, respectively). The two bands touch at the  $K$  and  $K'$  points of the first Brillouin zone making graphene a zero band gap semiconductor. Using a tight-binding (TB) model, Wallace showed that the dispersion relation turns out to be linear close to these points, which are referred to as Dirac points [29]:  $E = \hbar k v_F$  with  $\hbar k$  the norm of the momentum and  $v_F$  the Fermi velocity which amounts to about  $1/300$  of the speed of light. This unusual dispersion relation of its charge carriers makes them behave like massless Dirac fermions, which is interesting because it allows to study the effects of quantum electrodynamics governed by

the relativistic Dirac equation with comparably simple experimental setups [33]. Together with the sublattice symmetry, this is related to the observation of an anomalous half-integer quantum Hall effect [33] and high charge carrier mobility with a ballistic transport regime for submicrometer distances up to room temperatures [3]. Also related to the two-dimensional structure and the gapless electronic spectrum, graphene absorbs a fraction of 2.3% of the light in the range of the near infrared and visible electromagnetic spectrum, which is surprisingly high considering that it is only one atom thick [34].

The strong inplane  $\sigma$ -bonds between the carbon atoms make graphene the material with the highest tensile strength and the largest Young's modulus ever measured [35]. However, in practice, the strength of macroscopic graphitic materials is limited because of defects and grain boundaries. Despite the large research effort put into graphene recently, other basic material properties such as the thermal expansion coefficient (TEC) are still under debate [36, 37].

Graphene monolayers prepared by mechanical exfoliation have good quality and reached sizes of up to 10  $\mu\text{m}$  already since 2004, which made them useful for various investigations [3]. However, this method of preparation is not practical for large-scale production. A promising alternative is the epitaxial growth of graphene, which can be achieved by CVD, temperature programmed growth or segregation based methods [32]. We discuss epitaxial graphene in a separate section below as this material has been studied in this work as a substrate for NP deposition.

### 1.2.2 Graphite

Graphite consists of graphene layers following different sequences, both stackings ABAB (Bernal stacking) and ABCABC (rhombohedral) occur in nature. Those planes are bound to each other by weak van der Waals forces that originate from the delocalized  $\pi$  electrons of the individual layers. The spacing between the layers is about 3.35 Å [38] which is much more than the inplane nearest-neighbor distance of carbon atoms. Parallel to the graphite layers, the material is a good electrical and thermal conductor, which is not the case perpendicular to the layers. The weak van der Waals intralayer interactions allow for sliding of the layers with respect to one another which makes graphite a good lubricant [38]. The modeling of graphite requires often special care for the interlayer interaction, because they are not described correctly in empirical or DFT calculations without explicit account for van der Waals forces.

Graphite is studied as a relatively cheap substrate for cluster deposition in view of applications in catalysis [39, 40]. In particular, it has been shown that NP coalescence can be avoided despite surface diffusion, which are two key factors for NP self-organization [23]. In comparison to NPs on epitaxial graphene on metal (GOM), metal clusters on graphite may experience high surface diffusion rates [41, 42] following a Lévy-type stick-slip mechanism [42]. Interestingly, this behavior is only observed for clusters but not for single adatoms [42]. Such processes are also investigated in the present work.

### 1.2.3 Epitaxial graphene on metal (GOM)

Discovered at least 50 years ago [43, 44], GOM has attracted growing interest during the last decade [32, 45]. Epitaxially grown graphene monolayers provide sufficient amounts of carbon to chemically passivate a metal surface, and such surfaces could provide a mirror for future neutral atom or molecule microscopes [46]. Due to the mismatch between the lattice constants of the two materials, moiré structures of different sizes are observed upon contact, with different geometries and relative stabilities. Those moiré patterns constitute two dimensional nanoscale meshes that can serve as a template for depositing small clusters [19] with potential applications

in high-density information storage [4, 19, 47]. The self-assembly of metal clusters on epitaxial graphene has been observed experimentally [19, 48–52] and modeled by kinetic Monte Carlo (MC) simulations [53, 54].

Depending on the underlying metal, the deformation of the graphene monolayer (and, to a lesser extent, of the metal itself) varies, as the result of the different interactions ranging from physisorption (platinum, iridium or copper) to stronger chemisorption (ruthenium, nickel or cobalt) [32]. In the case of weak interaction, the interaction energy and the spacing of the graphene layer is similar to the interaction energy and spacing of the topmost layer in graphite. The spacing of epitaxial graphene in the strongly interacting systems on the other hand resembles the spacing between two metal layers of the bulk crystal. The size of the moiré structure depends on the commensurability that may change with temperature due to unequal TECs of the two materials [55]. In addition, an inplane angle between graphene and metal surface may decrease the size of the moiré structure. Non-zero inplane angles are more common in weakly interacting systems [32].

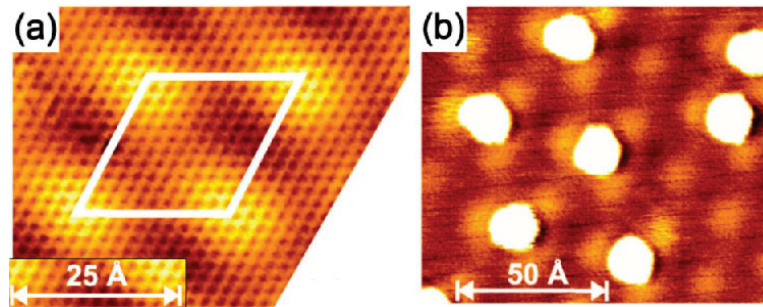


Figure 1.2: STM topograph of: (a) graphene/Ir(111), (b) Ir clusters on graphene/Ir(111). Figure adapted from N'Diaye and coworkers [19].

Due to its nanostructuration, epitaxial graphene may favor self-organization of metal adsorbates at their surface [19]. This can be achieved by on site growth using atomic deposition [19] or by the deposition of preformed clusters in the gas phase [37]. In comparison to adsorbates on graphite, clusters on epitaxial graphene are very stable and show reduced diffusion propensity [56, 57]. Fig. 1.2(a) shows a scanning tunneling microscopy (STM) topograph of the graphene/Ir(111) moiré. The small scale structures correspond to the graphene lattice while at a larger length scale of about 25 Å (as highlighted by the white lines) the moiré pattern is clearly visible. Panel (b) shows Ir clusters deposited onto the moiré structure.

There is a considerable number of complementary experimental techniques suitable for investigations on these systems. Apart from STM, most common are atomic force microscopy (AFM), low-energy electron diffraction (LEED), Auger electron spectroscopy (AES), X-ray diffraction measurements and Raman spectroscopy. Some of the cited techniques may require ultra high vacuum or low temperatures achieved by liquid helium cooling, which may be experimentally challenging. A comprehensive review of these methods and related ones can be found in Ref. [32]. Reliable experimental techniques are key for the classification and measurement of nanoscaled systems, while numerical simulations offer a complementary approach to experiments allowing detailed studies of idealized systems. The next section introduces some common techniques.

## 1.3 Commonly used modeling tools

In the following we give a brief overview of the most widely used simulation methods which have successfully been employed for the modeling of adsorbates on carbonaceous systems. In principle all observables can be derived from the solution of the full many-body Schrödinger equation. However this proves intractable for systems comprising more than several electrons. The systems of graphene on metal moiré structures that we wish to model contains about  $10 \times 10$  graphene unit cells with 2 carbon atoms each. The model needs to include at least three metallic layers for a distinction between ABAB and ABC stackings, which adds about  $10 \times 10$  metal atoms per layer with about 20-80 electrons each. Furthermore, possible adsorbates amount to another typically 10–100 metal atoms. In order to be able to simulate systems of this size, especially at finite temperature, approximate theories have been developed. In the following, we give an overview over the most common.

### 1.3.1 Density functional theory (DFT)

DFT is one of the most widely used methods for quantum chemical modeling in material science. Allowing to study the electronic structure of systems containing a large number of electrons and nuclei, the method has comparably high predictive power as it contains no (or few) empirical ingredients. DFT methods express the total energy  $E$  of a configuration of electrons in the ground state at zero temperature as a functional of the electronic density  $\rho(\vec{r})$  at position ( $\vec{r}$  units) [58] (assuming atomic units):

$$E[\rho] = \int V_n(\vec{r})\rho(\vec{r})d\vec{r} + \iint \frac{\rho(\vec{r})\rho(\vec{r}')}{2|\vec{r} - \vec{r}'|}d\vec{r}d\vec{r}' + G[\rho], \quad (1.1)$$

where  $V_n(\vec{r})$  represents an external potential created by the atomic nuclei, which are assumed to be fixed (Born-Oppenheimer approximation) and the second term the Coulomb interactions between electrons  $V_H$ . The functional  $G$  contains the kinetic, exchange, and correlation energy and is universal, meaning that it is independent of the nature of the system. Unfortunately it is not known, Kohn and Sham developed self-consistent expressions which map the system of interacting electrons onto a system of non-interacting electrons thus treated by an effective potential  $V_{\text{eff}}(\vec{r}) = V_n(\vec{r}) + V_H(\vec{r}) + V_{xc}(\vec{r})$ , with  $V_{xc}$  the exchange-correlation potential [59]. This makes the kinetic energy dependent only on the one-electron orbitals  $\psi_i$ , which can be obtained by the variation of the total energy:

$$\left[ V_n(\vec{r}) + V_H(\vec{r}) + V_{xc}(\vec{r}) - \frac{1}{2}\Delta \right] \psi_i = \epsilon_i \psi_i. \quad (1.2)$$

In practice self-consistency is reached iteratively, starting from an initial guess for the electronic density. Still, unfortunately there is no exact expression for the exchange-correlation term, however some approximations exist: In solid state physics the most popular are the local density approximation (LDA) and the generalized gradient approximation (GGA). LDA designates local functionals which depend only on the local electronic density while GGA methods also take the gradient of the electronic density into account and are therefore referred to as a semi-local. In order to facilitate practical calculations, normally only valence electrons are taken explicitly into account. This can be achieved by replacing the external potential by pseudopotentials.

Both local and semi-local functionals do not take into account long range correlations which give rise to dispersion interactions that are usually negligible with respect to the covalent or metallic interactions. However, for the interaction of adsorbates with bulk or semi-infinite sub-

strates, one important contribution is that of long-range dispersion forces [60–69]. To overcome this shortcoming, several dedicated approaches have recently been developed [70], relying either on electronic density-based corrections or on empirical pairwise approximations. The former class of methods includes both truly nonlocal functionals [71, 72] and the highly parametrized forms of meta-hybrid approximations [73, 74]. The second class of methods, which includes DFT-D, uses in its most basic form a pairwise atomistic additive correction of dispersion with a  $C_6$  coefficient and a damping function [75, 76] for which several parametrizations and expressions have been proposed [77–81].

Among the conclusions of those recent developments, dispersion forces were found to be significantly influenced by the local environment, appropriate  $C_6$  coefficients possibly varying by one order of magnitude depending on the size and shape of the structure [66, 82, 83]. For instance, in order to model adsorption on metallic or semiconducting substrates, electron delocalization can also screen dispersion forces, which introduces some dependence on temperature and on the range, notably through retardation effects at longmost distances [84]. Such effects have been investigated also experimentally in the case of organic molecules in contact with a metal surface [85].

Using the Hellmann-Feynman theorem, forces on the atomic nuclei can be evaluated directly from the orbitals without the knowledge of their gradient with respect to atomic positions. This allows to carry local structural optimizations or even molecular dynamics MD simulations for studying temperature effects. However, especially with MD this task becomes computationally very intensive in the case of system sizes cited above, notably to obtain reasonable statistical averages. TB methods or empirical atomistic potential are in many situations more practical for such calculations.

### 1.3.2 Tight-binding model and empirical atomistic potentials

#### Tight-binding theory

While the DFT approach currently stands as the most realistic way of treating atomic and molecular interactions in complex systems, it is computationally limited in terms of size and time scales. The TB model still offers a quantum mechanical description at reduced computational cost. As its name suggests, the model assumes that electrons are tightly bound to the atomic cores, so that there is only limited interaction with neighboring atomic sites. However, there is no single model to describe the TB method [86] and the following introduces the general formulation by following the discussion of Ashcroft and Mermin [87].

The true Hamiltonian  $H$  is approximated by a sum of isolated atom Hamiltonians ( $H_{\text{at}}$ ) located at site  $i$ :

$$H = \sum_i H_{\text{at}}(\vec{r} - \vec{R}_i) + \Delta U(\vec{r}), \quad (1.3)$$

where  $\Delta U$  represents a small correction due to the presence of the other atomic sites. The eigenstates of the atomic Hamiltonian  $\psi_n$  are well localized on the atomic sites and are assumed to become small on neighboring sites. The  $\psi_n$  are referred to as atomic orbitals and the electronic state  $\Psi_i$  at a given atomic site can be expressed as a linear combination of them:

$$\Psi_i(\vec{r}) = \sum_n b_n \psi_n(\vec{r}), \quad (1.4)$$

with the expansion coefficients  $b_n$ . The Bloch theorem can be satisfied by combining these

states into the following form of a solution for the total  $N$  atomic sites located at  $\vec{R}_i$ :

$$\Phi(\vec{r}) = \sum_{R_i} \exp\left(i\vec{k}\cdot\vec{r}\right) \Psi_i(\vec{r} - \vec{R}_i), \quad (1.5)$$

where  $\vec{k}$  designates a reciprocal lattice vector in the range of the first Brillouin zone. Applying the Hamiltonian of expression (1.3) yields the Bloch energies  $E(\vec{k})$ :

$$H\Phi(\vec{r}) = H_{\text{at}}\Phi(\vec{r}) + \Delta U(\vec{r})\Phi(\vec{r}) = E(\vec{k})\Phi(\vec{r}) \quad (1.6)$$

Multiplying with an atomic wave function of  $\psi_m^*$  leads to the following matrix equation:

$$\sum_n A(\vec{k})_{m,n} b_n = E(\vec{k}) \sum_n B(\vec{k})_{m,n} b_n, \quad (1.7)$$

where the matrices  $A$  and  $B$  can be determined as:

$$A(\vec{k})_{m,n} = \sum_{R_i} \exp\left(i\vec{k}\cdot\vec{R}_i\right) \int \psi_m^*(\vec{r}) H \psi_n(\vec{r} - \vec{R}_i) d\vec{r} \quad (1.8)$$

$$B(\vec{k})_{m,n} = \sum_{R_i} \exp\left(i\vec{k}\cdot\vec{R}_i\right) \int \psi_m^*(\vec{r}) \psi_n(\vec{r} - \vec{R}_i) d\vec{r}. \quad (1.9)$$

Two integrals can be identified in the matrix elements:

$$s(\vec{R}_i) = \int \psi_m^*(\vec{r}) \psi_n(\vec{r} - \vec{R}_i) d\vec{r} \quad (1.10)$$

$$t(\vec{R}_i) = \int \psi_m^*(\vec{r}) \Delta U(\vec{r}) \psi_n(\vec{r} - \vec{R}_i) d\vec{r}, \quad (1.11)$$

which are commonly referred to as overlap and hopping integrals, respectively. Usually, in the so-called two-center approximation, only the nearest neighbors are taken into account in the hopping integrals  $t(\vec{R}_i)$ . In addition, the overlap integrals  $s(\vec{R}_i)$  are sometimes neglected (for  $\vec{R}_i \neq 0$ ), leading to orthogonal TB. If this second approximation is not made, the generalized eigenproblem can be solved by applying a Löwdin transformation [88]. In the TB method, the values of the matrix element are not calculated explicitly, but are modeled directly as a function of the atomic positions [86].

### Atomistic potentials

For calculations on larger systems and longer timescales, semi-empirical analytical potentials should be applied. In particular, MD necessitate the derivatives of the potential energy with respect to atomic coordinates. Their evaluation is particularly efficient when analytical expressions exist, as is the case for many empirical potentials. This is of course to the price of chemical accuracy and transferability. The analytical expressions of the potentials depend only on interatomic distances, but may be related to theory, TB for example. Nonetheless, they contain empirically adjusted parameters and empirical correction terms. Care must therefore be taken when employing such a potential in situations deviating too far from the training set on which they were parametrized. These force fields for modeling covalent or metallic materials also typically neglect dispersion forces altogether rather similarly to the way DFT approaches were neglecting those corrections until last decade (and still often do). Dispersion interactions

between metal adsorbates and extended substrates have been explicitly taken into account in some empirical models based on the Lennard-Jones (LJ) potential [89] but otherwise lacking chemical consistency.

In this work, we make use of such formulations in order to study temperature effects on adsorbates in contact with carbonaceous substrates. Following the Grimme (D2) strategy often used in combination with DFT calculations, we propose some analytical extensions taking into account the crystalline and semi-infinite natures of the substrate and, in the case of epitaxial graphene, the possible screening of the van der Waals interaction by the bulk underlying metal.

## 1.4 Outline of the manuscript

In the following chapter, we introduce in detail the methods that have been employed in this work. In particular, we introduce the semi-empirical atomistic potentials, their parameterization and extension to long-ranged dispersion forces, followed by the details of the simulation methods, in particular local structure optimization and MD simulations. Chapter 3 treats the system of Pt NPs on graphite and graphene/Pt(111). As graphene/Pt(111) is one of the weakly interacting systems, dispersion forces are particularly important, which makes the system a good testing ground of the dispersion models introduced in chapter 2. In addition a fully parametrized atomistic potential is available in the literature for Pt-C, which allowed to focus on the non-bonding interaction. Systems containing ruthenium and carbon *i.e.* Ru NPs on graphite and graphene/Ru(0001) are addressed in chapter 4. A parameterization of the semi-empirical potential for this system was applied with satisfactory success, which is the main goal of the chapter. Even though graphene/Ru(0001) is a strongly interacting system governed by covalent and metallic interactions, dispersion still plays an important role and is therefore included in a similar way as for the Pt-C system. Another parameterization of the semi-empirical potential, for the Ir-C system, is attempted in chapter 5. Due to problems specific to this system, less comprehensive calculations could be carried out. The chapter also presents a few calculations on the strongly interacting graphene/Ni(111) system based on a more sophisticated (but also more involved) potential. Finally, in chapter 6 we summarize and suggest other applications of the present methodology to related systems.



# Chapter 2

## Methodology

The calculation of the total cohesive energy of an atomic structure necessitates in principle the resolution of the Schrödinger equation. While the two-body system can be solved exactly, for larger systems numerical solutions become rapidly too difficult and time-consuming to obtain. Analytical interatomic potentials are approximations that provide simplified expressions for the quantum-mechanical interactions of electrons and nuclei. They allow the numerical simulation of much larger systems and on longer timescales. The elaboration of the functional form of a such potential requires a qualitative understanding of the nature the quantum-mechanical bonding of atoms. The functional form is the result of a number of empirical approximations and possible additional corrective terms. Unfortunately, no form has been found that could describe arbitrary systems. However, for several types of bonding, dedicated potentials have been developed and employed with great success, such as the LJ potential [90] for noble gases, the embedded-atom model (EAM) [91, 92] for metals or the bond-order potentials (BOPs) for semiconductors [93]. Generally, semi-empirical interatomic potentials depend on a number of parameters that need to be adjusted in order to make them practical for a particular application. This corresponds to a nontrivial optimization problem, where the adjustable parameters are varied in order to reproduce reference data from a training set. These databases may contain for example interatomic distances, cohesive energies or elastic constants. Once a potential is appropriately parametrized, it may be used for the calculation of structural, statistical and dynamical properties of a system. This can be achieved by methods such as local geometry optimization, MC and MD simulations for which the specific methodologies are detailed in this chapter.

The following sections 2.1-2.3 present the interatomic potentials that have been used for the modeling of the generic system of transition metal adsorbates on extended carbonated substrates. The global optimization approach followed in order to obtain a parametrization for the specific cases of the ruthenium-carbon and the iridium-carbon systems is given in section 2.4. The covalent interatomic potential has further been extended by an empirical correction for dispersion interactions, which may play an important role for adsorption phenomena on extended substrates. Based on the Grimme D2 approach this correction is integrated as a coarse grained contribution into the description of the system as detailed in section 2.5. Section 2.6 discusses the basis of the numerical simulation methods mentioned above and section 2.7 presents the observables employed for the characterization of the system.

## 2.1 Tight-binding theory in the second moment approximation (TB-SMA)

The TB theory represents one of the most simple quantum mechanical methods for describing semiconductors, simple and transition metals. Applying several further approximations to this theory allows to derive an analytical expression for the band energy, leading to an explicit potential known as TB in the second moment approximation (TB-SMA). The purpose of this section is to give an overview of these approximations and to present the form of the TB-SMA potential.

The binding energy in transition metals and their alloys is mainly due to the  $d$ -band electronic density of states [94]. If only one atomic orbital is taken into account, the total binding energy  $V_B^i$  for atom  $i$  can be expressed as [95]:

$$V_B^i = \int_{-\infty}^{E_f} (E - \varepsilon_i) N_i(E) dE, \quad (2.1)$$

where  $N_i$  is the electronic density of states at atomic site  $i$  and  $E_f$  the Fermi energy. For the next step, the electronic density of states is approximated by its average value and effective width  $W_i$ . Its average value would then be  $10/W_i$  for a full  $d$ -band. The interaction will therefore be restricted to first neighbors only. Further assuming local charge neutrality, the bond energy can be expressed as [96]:

$$\tilde{V}_B^i = -\frac{1}{20} W_i N_d (10 - N_d), \quad (2.2)$$

with  $N_d$  the number of electrons in the  $d$ -band. Note that  $\tilde{V}_B^i$  is proportional to the effective width of the electronic density of states in this approximation. With the average value for the electronic density of states, its second moment  $\mu_i$  can be calculated as

$$\mu_i^2 = \int_{-\infty}^{\infty} E^2 N_i(E) dE = \int_{-W_i/2}^{W_i/2} \frac{10}{W_i} E^2 dE = \frac{10}{12} W_i^2. \quad (2.3)$$

Comparing to its value expressed as a function of the two-center hopping integrals  $h_{ij}$

$$\mu_i^2 = 10 \sum_{j \neq i} h_{ij}^2, \quad (2.4)$$

this leads to  $W_i^2/12 = \sum_{j \neq i} h_{ij}^2$  [96]. Because  $\tilde{V}_B^i$  is proportional to  $W_i$ , the binding energy can be written as

$$\tilde{V}_B^i = \text{const.} \cdot \sqrt{\sum_{j \neq i} h_{ij}^2} \quad (2.5)$$

where  $h_{ij}^2$  can be identified with the electron density  $\rho_i$  [96]. Assuming a typical exponential form for the dependence  $\rho_i$  on the interatomic distance  $r_{ij}$  and adding an empirical repulsive pair potential  $\tilde{V}_R^i$  also of the exponential form (Born-Mayer repulsion) leads to the expression of the TB-SMA potential:

$$E = \sum_i \sum_{j \neq i} A^{ij} e^{-p^{ij}(r_{ij}/\tilde{r}_0^{ij} - 1)} - \left[ \sum_{j \neq i} \xi_{ij}^2 e^{-2q^{ij}(r_{ij}/\tilde{r}_0^{ij} - 1)} \right]^{1/2} \quad (2.6)$$

where  $A^{ij}$ ,  $\xi_{ij}$ ,  $p^{ij}$ ,  $q^{ij}$  and  $\tilde{r}_0^{ij}$  take the role of adjustable parameters. The square root dependence of the band energy is of quantum-mechanical origin and conveys the many body character of the potential. The functional form of the potential is very similar to the one employed within the EAM [91, 92], however the TB-SMA derivation makes the physical basis more transparent and the approximation that were necessary for its derivation help to understand its limitations.

The next section introduces BOPs that have been routinely used to model a broad variety of metallic and covalent materials. Their ability to describe both types of bonding has motivated us to choose such a potential to model metallic NPs on carbon substrates. Furthermore, it turns out that the TB-SMA potential can be rewritten as a special case of a BOP [97], which allows for a uniform description of a system jointly using both potentials.

## 2.2 Brenner bond-order potential (BOP)

BOPs were developed in such a way that the bond strength would depend on the local environment according to the Pauling concept of bond order [98, 99]. In general, highly coordinated atoms form weaker bonds, which can stabilize lowly coordinated structures. This effect cannot be reproduced by pair potentials. In addition, three-body potentials such as the Stillinger-Weber potential [100] cannot achieve this environment effect, which in turn causes transferability problems. This means the potential cannot be used in situations for which it has not been explicitly developed. Adding more terms, such as four- or even five-body contributions would lead to a hardly traceable high number of parameters and unreasonably increased computational cost. To overcome these difficulties, Tersoff introduced a  $n$ -body potential that gives up on introducing higher order body-terms, but builds the relevant chemistry and physics directly into its functional form via a bond-order term [93]. This approach proved successful for increasing the transferability of the potential. The bond-order term decreases the interaction strength for higher coordinated atoms. If this term is strong it stabilizes lowly coordinated compounds such as diatomics and, if the dependence on the local environment is weak, it favors closed-packed lattices.

However, further analysis showed that the Tersoff potential is unable to reproduce several properties of carbon such as a proper description of radicals and conjugated versus non-conjugated double bonds [101]. For a correct description of these intermediate bonding situations, the Brenner potential was developed. Originally, it was used for diamond and graphene as well as for hydrocarbon molecules and is now widely used in materials science owing to its ability to model metals and covalently bound systems in a common framework [97] (see below). In the Brenner BOP the total binding energy of the system at the collective set of Cartesian coordinates  $\mathbf{R} = \{\vec{r}_i\}$  is expressed as a sum over individual bonds [101]:

$$E = \sum_i \sum_{j < i} f^{ij}(r_{ij}) (V_R^i - \bar{b}_{ij} V_B^i), \quad (2.7)$$

where the repulsive ( $V_R^i$ ) and attractive ( $V_B^i$ ) parts both take exponential expressions, so  $V_R^i - \bar{b}_{ij} V_B^i$  has a Morse-like form:

$$V_R^i = \frac{D_0^{ij}}{S^{ij} - 1} e^{-\beta^{ij} \sqrt{2/S^{ij}} (r_{ij} - r_0^{ij})}, \quad (2.8)$$

$$V_B^i = \frac{S^{ij} D_0^{ij}}{S^{ij} - 1} e^{-\beta^{ij} \sqrt{2/S^{ij}} (r_{ij} - r_0^{ij})}. \quad (2.9)$$

The parameters in these equations are set separately for each type of pairs of atoms, *i.e.*

carbon-carbon, metal-metal and metal-carbon.  $D_0^{ij}$  and  $r_0^{ij}$  correspond to the binding energy and equilibrium distance of an isolated diatomic,  $S^{ij}$  and  $\beta^{ij}$  denote six additional adjustable parameters that can be related to the dependence of the bond energy on the nearest neighbor distances and the harmonic vibrational frequencies of the diatomics, respectively. The bond order  $\bar{b}_{ij}$  carries the many-body character of the potential, and involves triplets  $(i, j, k)$  of atoms where both  $k$  and  $i$  are neighbors of  $j$ :

$$\bar{b}_{ij} = \frac{1}{2} (b_{ij} + b_{ji}) \quad (2.10)$$

$$b_{ij} = \left\{ 1 + \sum_{k \neq i, j} f^{ik}(r_{ik}) g(\Theta) e^{2\mu_{ijk} [(r_{ij} - r_0^{ij}) - (r_{ik} - r_0^{ik})]} \right\}^{-\frac{1}{2}}. \quad (2.11)$$

In the above equation we have introduced the bending angle  $\Theta = \widehat{jik}$  between atoms  $i$ ,  $j$  and  $k$ , and the angular dependence of the function  $g$  is explicated as

$$g(\Theta) = \gamma_{ijk} \left[ 1 + \left( \frac{c_{ijk}^2}{d_{ijk}^2} - \frac{c_{ijk}^2}{d_{ijk}^2 + (1 + \cos \Theta)^2} \right) \right], \quad (2.12)$$

where  $\mu_{ijk}$ ,  $\gamma_{ijk}$ ,  $c_{ijk}$  and  $d_{ijk}$  are additional adjustable parameters. The function  $f^{ij}$  finally provides a smooth cut-off between the distances  $R^{(1)}$  and  $R^{(2)}$ :

$$f^{ij}(r) = \begin{cases} 1 & r < R_{ij}^{(1)} \\ \frac{1}{2} \left[ 1 + \cos \left( \pi \frac{r - R_{ij}^{(1)}}{R_{ij}^{(2)} - R_{ij}^{(1)}} \right) \right] & R_{ij}^{(1)} \leq r \leq R_{ij}^{(2)} \\ 0 & r > R_{ij}^{(2)} \end{cases} \quad (2.13)$$

In the original publication the bond-order expression contains additional special terms for non-conjugated carbon and hydrocarbon molecules [101]. They were dropped here because they are not necessary for the description of graphene, for which the potential is used in this work. Brenner gives two parametrizations of the potential: one that reproduces better the bond lengths and vacancy formation energies and another that is more precise in reproducing bond rigidities at the expense of a degraded reproduction of the other quantities [101]. We chose the latter as it promises a better description of the behavior at finite temperature that we want to simulate with the help of MD.

## 2.3 Unification of Brenner BOP with TB-SMA

As mentioned above, the TB-SMA potential represents a special case of the Brenner BOP as shown by Brenner [97]. This makes the modeling of a system, where some interatomic interactions are described by the TB-SMA potential and others by the full Brenner BOP with angular terms that enable directional bonding where necessary, practical. The following algebra

steps are performed to express the TB-SMA potential under the Brenner form:

$$\tilde{V}_B^i = \left[ \sum_{j \neq i} \xi^2 e^{-2q(r_{ij}/\tilde{r}_0 - 1)} \right]^{1/2} \quad (2.14)$$

$$= \left\{ \sum_{j \neq i} \xi^2 e^{-2q(r_{ij}/\tilde{r}_0 - 1)} \right\} \left[ \sum_{k \neq i} \xi^2 e^{-2q(r_{ik}/\tilde{r}_0 - 1)} \right]^{-1/2} \quad (2.15)$$

$$= \left\{ \sum_{j \neq i} \xi^2 e^{-2q(r_{ij}/\tilde{r}_0 - 1)} \left[ \sum_{k \neq i} \xi^2 e^{-2q(r_{ik}/\tilde{r}_0 - 1)} \right]^{-1/2} \right\} \quad (2.16)$$

$$= \sum_{j \neq i} \xi^2 e^{-2q(r_{ij}/\tilde{r}_0 - 1)} \left[ \xi^2 e^{-2q(r_{ij}/\tilde{r}_0 - 1)} + \sum_{k \neq i, j} \xi^2 e^{-2q(r_{ik}/\tilde{r}_0 - 1)} \right]^{-1/2} \quad (2.17)$$

$$= \sum_{j \neq i} \xi e^{-q(r_{ij}/\tilde{r}_0 - 1)} \left[ 1 + \sum_{k \neq i, j} e^{-2q/\tilde{r}_0(r_{ik} - r_{ij})} \right]^{-1/2}. \quad (2.18)$$

This roots the Brenner bond-order formalism indirectly into the moments expansion of the TB model and allows for a uniform description for systems that contain interactions that are modeled partly by the TB-SMA and partly by the Brenner potential. However, this mapping of the TB-SMA onto the Brenner potential is only approximate since the cut-off function is applied in different ways in the two potentials. More importantly, the above derivation is valid only for potentials for one atomic species and it is not possible to transform a TB-SMA potential that describes more than one species into a Brenner BOP. This limitation is caused by the dependence of the parameter  $\mu$  on triplets of atoms, whereas the TB-SMA does not contain such a parameter. Therefore the indices of the parameters have been dropped in the above calculation.

Comparing the Brenner BOP presented in section 2.2 to Eq. (2.18) leads to the following identities that give the Brenner parameters as a function of those of the TB-SMA:

$$S = \frac{p}{q} \quad (2.19)$$

$$\beta = \frac{1}{\tilde{r}_0} \sqrt{\frac{pq}{2}} \quad (2.20)$$

$$D_0 = 2\xi \left( 1 - \frac{q}{p} \right) \left( \frac{Ap}{\xi q} \right)^{\frac{q}{q-p}} \quad (2.21)$$

$$r_0 = \left[ 1 + \ln \left( \frac{Ap}{\xi q} \right) \frac{1}{p - q} \right] \tilde{r}_0 \quad (2.22)$$

$$\gamma = 1 \quad (2.23)$$

$$c = 0 \quad (2.24)$$

$$d = 1 \quad (2.25)$$

$$2\mu = \frac{2q}{\tilde{r}_0}, \quad (2.26)$$

where it should be emphasized that  $r_0 \neq \tilde{r}_0$ . Obviously, the other direction of expressing a Brenner BOP under the form of a TB-SMA potential is not possible in general, because of the explicit angular terms contained in the BOP. The connection between the two forms is

basically a consequence of the similar bondings in semiconductors and in  $d$  transition metals in the TB-SMA approach [96].

## 2.4 Parametrization procedure

The Brenner BOP has already been parametrized for a number of combined elements such as C-H [101], Pt-C [96], Si-C [102], Zn-O [103], Fe-C [104] and even Be-C-W-H [105], among others. However, not for all of the systems that have been studied in this work do such parametrizations exist. We thus attempted to parametrize the BOP model for ruthenium and iridium in contact with carbon. Details about the specific interaction types are discussed in chapter 4 for the Ru-C system and in chapter 5 for the Ir-C system. This section describes the general approach that was taken for the search of appropriate parameter sets.

### 2.4.1 Problem of parameter optimization

The Brenner potential expresses the total cohesive energy as a function of several parameters that we collectively denote as

$$\mathbf{X} = \{S, \beta, D_0, r_0, R^{(1)}, R^{(2)}, \gamma, c, d, \mu\}.$$

These parameters were adjusted by optimizing an error function targeting several reference properties obtained from DFT calculations. More information about these DFT calculations which have been carried out by our collaborators are given in the sections dedicated to the specific interaction types. The error function  $\chi^2$  includes sums of square gradient components on the relaxed geometries (vanishing force at equilibrium) and the interaction energies of the graphene monolayer and of adsorbates on the same substrate:

$$\chi^2(\mathbf{X}) = \sum_i \sum_\nu |\partial V(\mathbf{R}_i)/\partial q_\nu|^2 + \sum_i \rho_i [\Gamma_i - \Gamma_i^{(\text{ref})}]^2, \quad (2.27)$$

where  $\mathbf{X}$  denotes the set of parameters to be adjusted, the first and last sum are over equilibrium configurations  $\mathbf{R}_i$ , the second sum over atomic positions  $q_\nu$ . In the last sum,  $\Gamma_i$  and  $\Gamma_i^{(\text{ref})}$  denote the interaction energy  $E_i^{(\text{int})}$  of the graphene layer or of possible adsorbates obtained with the BOP or acting as target for configuration  $\mathbf{R}_i$ , respectively. We also define the interaction energy  $E_i^{(\text{int})}$  as the energy difference between the two subsystems in contact and at infinite separation but kept at the same configuration. The factor  $\rho_i$  is introduced to assign certain weights to the deviations from the reference adsorption energies of geometry  $\mathbf{R}_i$ , relative to each other and relative to the sums of square gradient components. The fitness of a particular parameter set  $\mathbf{X}$  to reproduce the reference data can therefore be quantified by  $\chi^2$ .

The optimization of the error function by varying the potential parameters amounts to a global optimization problem. The fitting database comprised up to six geometries, and the evaluation of the error function for a particular set of parameters can take up to several seconds of CPU time. While the search range for some of the Brenner parameters such as the cut-off distances may be restricted to a rather small interval, other parameters may change over several orders of magnitude during the optimization process. Even though the number of parameters to optimize may seem small, the task of finding optimal numerical values for all of them is therefore far from trivial. Sampling the error function on a regular grid or at random values for the parameters is not feasible, and instead it is preferable to use a MC procedure.

The principle of MC optimization for minimizing the error function is not different from the

context of structural optimization of molecular geometries, as discussed below. MC simulations are widely used for this purpose of global optimization, but have also broad range of other applications, such as a tool for the calculation of thermodynamical averages. Other applications of MC methods include the simulation of the passage of particles through matter [106] or even for the weather forecast [107].

### 2.4.2 Metropolis MC simulations in the canonical ensemble

Originally, the MC method was introduced for simple numerical integration in high-dimensional spaces, which found a natural application in the numerical calculation of the equation of states of liquids with the advent of fast computers by Metropolis and coworkers [108]. We use the standard Metropolis-Hasting algorithm for calculating averages in the classical canonical (NVT) ensemble [108, 109].

In the canonical ensemble under constant number of particles  $N$  and volume  $V$ , the expectation value of observable  $A$  at temperature  $T$  is expressed as

$$\langle A \rangle = \frac{\int_{\Omega} A(x) e^{-\frac{\mathcal{H}(x)}{k_B T}} dx}{\int_{\Omega} e^{-\frac{\mathcal{H}(x)}{k_B T}} dx} = \int_{\Omega} W(x) A(x) dx \quad (2.28)$$

where the integration is over all accessible phase space  $\Omega$ , and  $\mathcal{H}(x)$  the Hamiltonian of the system at the phase space position  $x$  and  $k_B$  the Boltzmann constant. We consider only cases where  $A$  does not depend on the momenta and thus the integrals can be restricted to the configurational space and the Hamiltonian replaced by the potential energy. Still, due to the high dimensionality of the system, the number of configurations to consider for obtaining reasonable averages is astronomic and not practical for direct sampling. Most of these configurations would have high potential energies and therefore do not contribute to the average of  $A$  because of the very small Boltzmann weight associated to them. This can be exploited by the so-called importance sampling, where mostly configurations with significant Boltzmann weight are considered for the averaging. In this purpose, configurations according to the probability distribution of  $W(x)$  need to be generated. Other probability distributions have also proven useful, but this is the most straightforward case, as the average of  $A$  can then be simply estimated by

$$\langle A \rangle = \frac{1}{N} \sum_{i=1}^N A(x_i) \quad (2.29)$$

where  $x_i$  are  $N$  generated configurations that follow  $W(x)$ . This makes it also unnecessary to evaluate the denominator of the fraction in Eq. (2.28).

The configurations according to  $W(x)$  may be generated using a Markov chain where new states or configurations are created on the basis of random perturbations of the previous state. The chain must be ergodic, meaning that every state in the chain can be reached from any other state under a finite number of moves. A criterion that allows to determine whether to accept a newly randomly generated configuration as the next state of the chain is needed. The states generated on the basis of the criterion need to follow  $W(x)$ . At equilibrium, the probability of leaving a state is equal to the probability of reaching it (detailed balance). This is satisfied for individual microstates if

$$W(a)P(a \rightarrow b) = W(b)P(b \rightarrow a) \quad (2.30)$$

where  $P(a \rightarrow b)$  designates the probability for accepting a transition from microstate  $a$  to

microstate  $b$ . The Metropolis criterion

$$P(a \rightarrow b) = \begin{cases} \frac{W(b)}{W(a)} & \text{if } W(b) < W(a) \\ 1 & \text{otherwise} \end{cases} \quad (2.31)$$

fulfills Eq. (2.30). For an efficient sampling it is recommended that new configurations are generated such that about half of them are accepted on the basis of the above criterion. As it stands this algorithm is usually for the estimation of thermodynamical averages of  $A$ , which become increasingly accurate with the number of configurations that contribute to the average. More details about the Metropolis MC method can be found in Refs. [110] and [111].

### 2.4.3 Local optimization with MC simulations at zero temperature

In the special case where the temperature is set to zero, only configurations that decrease the potential energy are accepted. This allows to carry out simple local geometry optimizations. The very same approach can be taken for the optimization problem cited above, where an optimal parameter set for an empirical potential is researched. In this most simple form of MC optimization, a Markov chain is constructed starting from a reasonable point  $\mathbf{X}_0$  taken as parameters from the literature for similar atom types. For the transition from one state or parameter set to the next the parameters are slightly changed by a random amount. The probability that a new state is realized is one when the error function decreases and zero when it increases. The amount by which a parameter is changed is different for all of them, because they all have a distinct physical meaning and affect the error function in quite different ways. In order to determine suitable values for these variations, trial runs where only one parameter is changed at a time, are carried out before starting the main optimization. During the trial runs, the variations are gradually decreased starting from high values close to the interval that is physically acceptable, where most of the time the error function increases, down to variations for which about half of the transition moves are accepted.

### 2.4.4 Global optimization with parallel tempering Monte Carlo (PTMC) simulations

The problem with zero-temperature MC optimization is that the algorithm allows only to climb down the pseudoenergy surface of the error function, making it likely that a local minimum close to the original parameter set is obtained, which represents an absorbing state for the Markov chain. Several methods such as simulated annealing [112, 113] have been developed in order to overcome this problem and achieve efficient global optimization, allowing (in principle) the system to escape from local traps. Unfortunately, the simulated annealing method is not efficient against multiple funnel energy landscapes, and we chose instead the PTMC algorithm [114], which performs much better in such situations [115].

The idea of PTMC is to carry out simultaneously several MC simulations at different temperatures and to allow from time to time exchanges of configurations between neighboring thermostats. These exchanges allow to escape local minima for the chains at lower temperature, if at higher temperature a parameter set with a reasonable value of its error function was found. So the purpose of the chains at higher temperatures is to explore broader regions of the parameter space and exchanging parameter sets from promising parameter space regions down to the chains at lower temperatures. Their purpose is to probe narrower but potentially deeper regions of parameter space in more detail. This idea is schematized in figure 2.1.

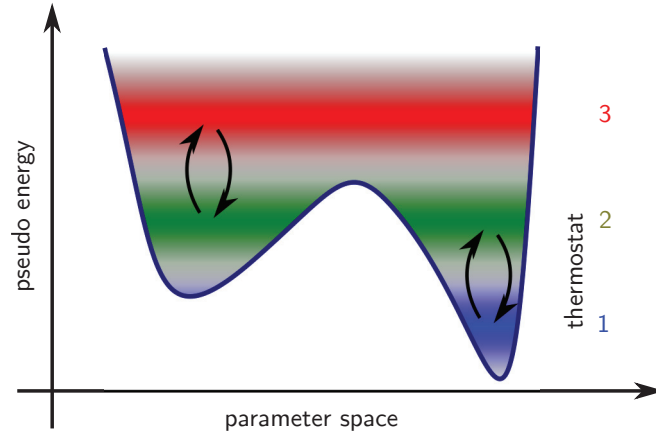


Figure 2.1: Principle of PTMC. Markov chains at high temperatures allow to explore broad regions of configuration space and help the chains at lower temperatures to escape local minima through successive swapping moves, resulting in a much faster equilibration. In the context of global optimization, the low temperature replicas can also discover previously unexplored regions much more efficiently.

In PTMC several Markov chains with transition probabilities corresponding to different statistical ensembles ruled by different temperatures are generated. Occasionally, swapping moves between the configurations  $\mathbf{X}_i$  and  $\mathbf{X}_j$  of trajectories at temperatures  $T_i$  and  $T_j$ , respectively, are attempted and accepted with probability that combines the two probabilities on both sides of the exchange:

$$P(\mathbf{X}_i \rightleftharpoons \mathbf{X}_j) = \begin{cases} \exp(-\Delta S) & \text{if } \Delta S > 0 \\ 1 & \text{otherwise,} \end{cases} \quad (2.32)$$

where  $\Delta S = [\chi^2(\mathbf{X}_i) - \chi^2(\mathbf{X}_j)] \cdot (1/T_j - 1/T_i)$ .

When performing parallel tempering simulations it is important to adjust the spacing between the temperatures so exchanges are accepted with a significant probability. At the same time it is not desirable to use a very fine grid in temperature, since it would not necessarily carry much more information and would slow down the communications between successive replicas. As in conventional MC, a 50% acceptance rate is close to ideal. In practice, 24 chains with geometrically distributed temperatures were propagated on a parallel computer, and two stages of PTMC optimizations were performed successively, reducing the temperature range during the second run. In a final step the error function was refined so that it contains properties of locally optimized geometries. These optimizations are carried out via a conjugate gradient method (see section 2.6.3) applied at each iteration of the algorithm. This new error function takes much more time to evaluate, but focuses on the more important equilibrium properties that we want to evaluate. In particular, because the forces calculated with a trial parameter set do never vanish exactly, the cohesive energy calculated during the PTMC procedure is always underestimated. Only with this refined error function, the cohesive energies of relaxed structures are evaluated. The Levenberg-Marquardt algorithm used for this final optimization requires only several tens of evaluations of the error function. This algorithm is able to locate the closest minimum of the error function in the parameter space that has been found by the parallel temperature procedure up to numerical precision.

## 2.5 London dispersion forces

Long-range dispersion forces are missing from the previously described BOP, and as such the model cannot properly describe adsorption phenomena on semi-infinite substrates. These nonbonding interactions are for instance almost exclusively responsible for the adhesion of a graphene layer on Pt(111) or Ir(111) [32]. However, the adsorption energy of graphene chemisorbed on Ru(0001) surfaces can also be enhanced by almost one order of magnitude by dispersion interactions [67]. A reasonable description of these nonbonding interactions represents therefore an integral part of the modeling of GOM and the adsorption of adsorbates thereon.

The description of physisorption phenomena on semi-infinite substrates by analytical potentials has been conveniently described by Steele [116] who integrated the LJ potential over a succession of crystallographic planes. We propose an extension of this approach to the case of metallic adsorbates on carbon substrates, taking into account the possibility of chemisorption as well. Our strategy is based on a Brenner BOP that is able to model both covalent and metallic parts of the system, and also mixtures of the two elements after appropriate parametrization [96]. We have enriched this potential with dispersion corrections in order to gain the ability of modeling correctly physisorption phenomena that are potentially essential for NPs in contact with extended environments. Those corrections follow the Grimme D2 model [76] employed for DFT calculations, as well as the Steele approach for integrating the van der Waals energy over the entire support. The Brenner force field has been further extended to include non-additive dispersion interactions in the case of electronically delocalized substrates, as present e.g. in GOM.

### 2.5.1 Grimme models

The approach we follow to include dispersion corrections is similar to the Grimme approach in DFT [76], and consists of adding a posteriori some dispersion energy to the covalent, metallic (and possibly ionic) contributions. In the fully atomistic Grimme D2 approach [76] the dispersion correction reads:

$$E_{\text{disp}}^{\text{D2}} = -s_6 \sum_i \sum_{j \neq i} \frac{C_6^{ij}}{r_{ij}^6} f_{\text{dmp}}^{ij}(r_{ij}) \quad (2.33)$$

where  $C_6^{ij} = (C_6^i C_6^j)^{1/2}$  are the parameters of the dominant van der Waals contributions,  $f_{\text{dmp}}^{ij}$  being a Fermi-type damping function so that dispersion only acts at long range and does not alter the covalent part:

$$f_{\text{dmp}}^{ij}(r_{ij}) = \frac{1}{1 + \exp \left[ -20 \left( \frac{r_{ij}}{R_6^{ij}} - 1 \right) \right]}. \quad (2.34)$$

Table 2.1 sums up the corresponding numerical values relevant for this work, which were extracted from the Grimme source code [76]. The prefactor  $s_6$  is to be adjusted depending on the functional. We adopt here the value  $s_6 = 1.05$  as indicated for the purely dispersionless functional BP86 [76]. In contrast to Grimme's original formulation, we consider dispersion interactions only up to the size of the simulation box neglecting interactions of the system with itself.

We have also tried the more recent and more realistic D3 version of Grimme's dispersion correction scheme [77, 78], in which the short-range damping takes another form and additional  $C_8$  terms are considered, the van der Waals coefficients being given further flexibility with some

Atomic species	$C_6$ (eVÅ <sup>6</sup> )	$R_r$ (Å)
C	18.1376	1.452
Ru	255.6890	1.639
Ir	842.0014	1.7721
Pt	842.0014	1.7721

Table 2.1: Grimme D2  $C_6$  coefficients and van der Waals radii for carbon and the different metals of relevance in this work.

Atomic species	$R_{\text{cov}}$ (Å)	$Q$ (Å <sup>2</sup> )
C	0.75	2.6996
Ru	1.13	9.4730
Ir	1.11	10.2650
Pt	1.12	9.7066

Table 2.2: Covalent radii as computed by Pyykkö and Atsumi [117] (values for metals decreased by 10%) and values for  $Q$  computed by Grimme and coworkers [77] for C and the various metals of relevance in this work.

dependence on the local coordination number (CN) of individual atoms:

$$E_{\text{disp}}^{\text{D3}} = - \sum_i \sum_{j \neq i} \sum_{n=6,8} s_n \frac{C_n^{ij}}{r_{ij}^n + f(R_0^{ij})^n}. \quad (2.35)$$

Here the function  $f(R_0^{ij}) = a_1 R_0^{ij} + a_2$  ensures the rational damping with  $R_0^{ij} = (C_8^{ij}/C_6^{ij})^{1/2}$ . The original authors gave parameters for  $a_1$ ,  $a_2$ , the  $s_n$  for various DFT methods for which this correction has been designed to work with. For our purposes, we choose again the parameters recommended for use with the BP86 functional ( $a_1 = 0.3946$ ,  $a_2 = 2.5673$  Å,  $s_6 = 1$  and  $s_8 = 3.2822$ ). The  $C_8^{ij}$  coefficients were obtained via  $C_8^{ij} = 3C_6^{ij} \sqrt{Q_i Q_j}$  with  $Q$  depending on electronic multipole expectation values (see Ref. [77] for more details). Numerical values for these parameters are given in Table 2.2. The  $C_6^{ij}$  and  $C_8^{ij}$  coefficients explicitly depend on the CN accordingly with [77]

$$\text{CN}^i = \sum_{j \neq i} \frac{1}{1 + \exp \left[ -16 \left( \frac{4}{3} \frac{R_{\text{cov}}^i + R_{\text{cov}}^j}{r_{ij}} - 1 \right) \right]}, \quad (2.36)$$

with  $R_{\text{cov}}$  the covalent radius of the corresponding atom [117]. The parameters for the D3 dispersion model were taken from Refs. [77, 78], the covalent radii from Ref. [117]. The corresponding numerical values are also shown in Table 2.2; note that the values for metals have been decreased by 10% in order to avoid excessively high CNs for these elements. Fig. 2.2 gives an idea on how much coordination may vary for a typical system studied here.

Grimme and coworkers [77] have computed values of  $C_6^{ij}$  for pairs of atoms of the 94 elements and several CNs. A Gaussian distance-weighted average was used for interpolation between different CNs. The authors applied a cutoff at 40 bohr for the CN and a cutoff at 95 bohr for the dispersion forces. In the case of periodic boundaries with box sizes smaller than the cutoff, they considered dispersion interactions of the system with itself until the cutoff is reached. This feature has not been implemented in the present work, instead we consider dispersion interactions only up to the size of the simulation box.

However, the added complexity of the D3 model produces a much less favorable scaling with

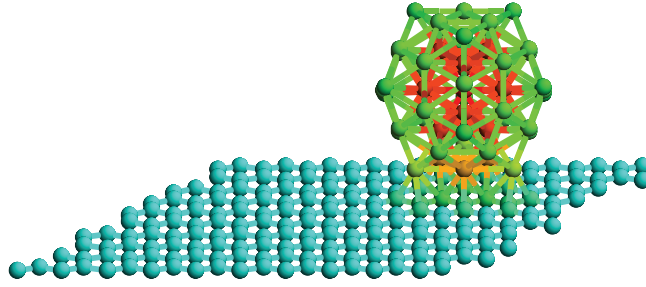


Figure 2.2: Typical initial configuration of a  $\text{Pt}_{55}$  cluster deposited on graphene, showing color-coded CNs ranging from teal (CN= 3.3) to red (CN= 11.3).

increasing number of atoms [in  $\mathcal{O}(n^3)$ ], even compromising the use of the BOP in the first place. The D3 dispersion model was thus used occasionally for comparison with the explicit D2 model and only for static properties, with explicit dispersion interactions being evaluated only up to the first periodic images of the system. Also, an adsorbate may influence the coordination of the substrate atoms in contact with it. This coordination-dependent dispersion model was therefore not pursued further in our attempt to construct a general coarse-grained model of dispersion forces on semi-infinite substrates.

## 2.5.2 Implicit model for dispersion interactions

We now consider the semi-infinite extension of the carbon substrate, assuming that the surface of the substrate lies perpendicular to the  $z$  axis. When using periodic boundary conditions, only the immediate contributions to the dispersion energy are explicitly included, and it may be necessary to integrate the missing contribution away from the primitive cell. These ideas were originally developed by Steele [116] who integrated the LJ potential for adsorption over an infinite stack of flat crystalline layers. One additional subtlety here is the presence of a short-range cut-off in the dispersion correction, which must be taken into account when carrying out the integration.

Aiming for a similar coarse-grained (implicit) model of the adsorbate-substrate dispersion interaction, we thus assume that the support can be described by a succession of flat layers with surface density  $\sigma$ . In the case of GOM,  $\sigma$  will denote the density of the topmost graphene layer, all metallic layers underneath having a possibly different surface density  $\sigma'$ . Although the following coarse-graining procedure can be used for integrating the many-body (but short ranged) component of the interactions [18], we use it here only for the long-range dispersion forces that are more sensitive to the infinite nature of the environment.

The interaction of the adsorbate with the first layer can be integrated as follows. We denote by  $d_i = z_i - \bar{z}$  the separation along the  $z$  axis of atom  $i$  of the adsorbate to the average layer position  $\bar{z}$  (see Fig. 2.4). For integration purposes we temporarily replace the Fermi-type damping function of the Grimme D2 model by a sharp short-distance cutoff placed where the original  $f_{\text{dmp}}^{ij}$  equals 1/2, namely at the position  $r_{ij} = R_r^{ij}$ :

$$f_{\text{dmp}}^{ij}(r_{ij}) \approx \begin{cases} 0 & r_{ij} \leq R_r^{ij} \\ 1 & \text{otherwise.} \end{cases} \quad (2.37)$$

The dispersion interaction of an adsorbate (ads) with a single substrate layer is then integrated

as

$$\tilde{E}_{\text{disp}}^{(1)} = \frac{-s_6\sigma C_6\pi}{2} \cdot \sum_{i \in \text{ads}} \begin{cases} R_r^{-4} & |d_i| < R_r \\ d_i^{-4} & \text{otherwise,} \end{cases} \quad (2.38)$$

where  $C_6$  is chosen appropriately to the atom-substrate under consideration and  $R_r$  denotes the cut-off of the dispersion interaction also chosen for the atom types in question. It should be noted that this requires the simulation box to be larger than  $2R_r$  in both lateral dimensions.

Due to the introduction of a sharp cut-off in  $f_{\text{dmp}}$ , this expression is not differentiable at  $d_i = R_r$ , hence we replace the constant part by an expression of the form  $ad_i^n + b$ , set to match the original expression at  $d_i = 0$  and to produce a continuously differentiable function:

$$\tilde{E}_{\text{disp}}^{(1)} = \frac{-s_6\sigma C_6\pi}{2} \sum_{i \in \text{ads}} \begin{cases} -\frac{4}{n} \left[ \left(1 + \frac{4}{n}\right)^{\frac{1}{4}} R_r \right]^{-4-n} d_i^n + R_r^{-4}, & |d_i| < R_r \left(1 + \frac{4}{n}\right)^{\frac{1}{4}} \\ d_i^{-4} & \text{otherwise.} \end{cases} \quad (2.39)$$

For  $n \rightarrow \infty$ , the original form is recovered. Choosing  $n = 50$  is a good compromise between an acceptable approximation and a sufficiently low curvature, as shown in Fig. 2.3.

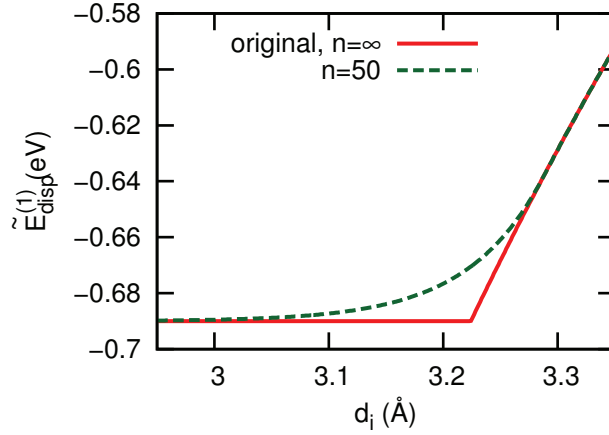


Figure 2.3: Dispersion energy  $\tilde{E}_{\text{disp}}^{(1)}$  of a Pt adatom as a function of the distance from a flat graphene sheet as computed with the original and its continuously differentiable version.

Eq. (2.39) is appropriate for describing the van der Waals contribution from the single graphene monolayer, but requires further summation for graphite. We thus sum the dispersion energy between the adsorbate and the infinite stack of layers of the substrate that we assume are distant from one another by a fixed quantity  $d_L$ . In summing up the above expression of Eq. (2.39) the condition  $|d_i| < R_r (1 + 4/n)^{1/4}$  is satisfied only up to a finite number of uppermost layers, as depicted in Fig. 2.4. In practice, this concerns the first two layers, for which Eq. (2.39) has to be explicitly used. For the remaining layers the summation leads to

$$\tilde{E}_{\text{disp}}^{(\infty)} = -\frac{s_6\sigma C_6\pi}{2} \sum_{i \in \text{ads}} \sum_{j=0}^{\infty} (jd_L + d_{i3})^{-4} \quad (2.40)$$

$$= -\frac{s_6\sigma C_6\pi}{2d_L^4} \sum_{i \in \text{ads}} \zeta \left( 4, \frac{d_{i3}}{d_L} \right) \quad (2.41)$$

where  $d_{i3} = z_i - \bar{z} + d_L^1 + d_L$  is the distance between an adsorbate atom and the third substrate layer and  $d_L^1$  the spacing between the first two substrate layers. For graphite,  $d_L^1 = d_L$ . In

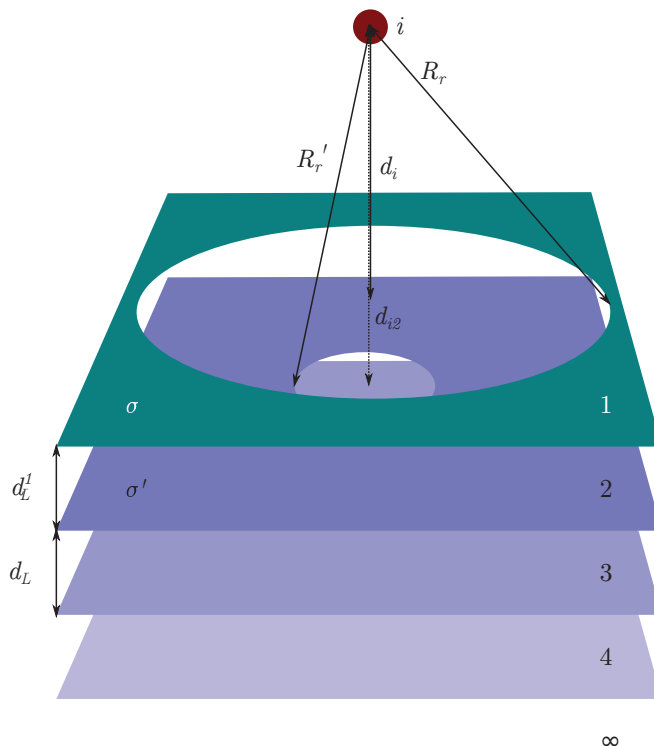


Figure 2.4: Interaction between an adsorbate atom  $i$  and a succession of planar layers, smoothly excluding regions within cut-off distances. See text for notations.

the previous equation,  $\zeta$  denotes the Hurwitz zeta function, which in practice was numerically evaluated using the `gsl_sf_hzeta` function of the GNU Scientific Library.

In the case of the substrates considered here, the first layer is always a graphene sheet with an atomic surface density of  $\sigma = 4/(\sqrt{3}a^2)$  of carbon atoms, where  $a = 2.51 \text{ \AA}$  is the graphene lattice parameter at 0 K (as computed with the present Brenner potential). The same surface density is used for all other layers in the case of the graphite substrate. For GOM, the metal layers all have the surface density  $\sigma_m = 2/(\sqrt{3}a_m^2)$  with  $a_m$  the first neighbor distance of the metal atoms in the triangular lattice at (111) fcc or (0001) hcp surfaces.

As a final comment for this section, it should be emphasized that the coarse-grained model for dispersion corrections assumes a planar substrate surface, in contrast with the original Steele potentials where binding is purely of the van der Waals type [116]. In the present models, lateral corrugation over the carbonated substrates is included through the bond-order contribution, which is always explicit. Lateral corrugation due to the periodic nature of the crystalline substrate is assumed to be much lower than the integrated contribution from the semi-infinite medium, and is therefore neglected.

### 2.5.3 Intra-graphite dispersion interactions

The original Brenner potential is not able to bind graphite layers together, and adding dispersion corrections of the Grimme type would not suffice because the covalent part does not operate at the experimental interlayer distance due to a too short cut-off. It is thus necessary to also modify the repulsive component of the potential. This problem was already pointed out by Tersoff who suggested to add a long-ranged pair potential in order to stabilize graphite [93]. This idea was taken up by Che and coworkers [118] and we follow their approach by addressing

these two issues simply by adding a LJ potential between atoms of different layers,

$$E_i^{\text{LJ}} = \sum_j' \frac{\varepsilon}{2} \left[ \left( \frac{\sigma_{\text{gr}}}{r_{ij}} \right)^{12} - 2 \left( \frac{\sigma_{\text{gr}}}{r_{ij}} \right)^6 \right], \quad (2.42)$$

where the primed sum indicates that the  $j$  atoms belong to a different layer than  $i$ . For this contribution we adopt the same parameters as in Ref. [118], namely  $\varepsilon = 3$  meV and  $\sigma_{\text{gr}} = 3.805$  Å. The LJ interaction is included in explicit models of graphite.

In order to derive a fully implicit model, we integrate Eq. (2.42) above over the flat monolayer to get the well-known result [116]

$$E_{\text{LJ},i}^{(1)} = \frac{\pi\sigma\varepsilon}{2} \left( \frac{\sigma_{\text{gr}}^{12}}{5d_i^{10}} - \frac{\sigma_{\text{gr}}^6}{d_i^4} \right) \quad (2.43)$$

in which  $d_i$  is the average distance between atom  $i$  and the layer.  $E_{\text{LJ}}^{(1)}$  is minimal for  $d_i = d_C^{\text{min}} = 2^{-1/6}\sigma_{\text{gr}} = 3.390$  Å at 25 meV/atom, which corresponds to the equilibrium spacing and binding energy a graphene bilayer. This has to be compared to the binding energy of 22 meV/atom at a bilayer separation of 3.32 Å computed by Gould and coworkers [119] with DFT in the LDA with dispersion corrections. Using a similar calculation, but with an infinite number of layers, we obtain for the equilibrium spacing a value of  $d_C = 2079^{-1/6}\pi\sigma_{\text{gr}}$ . With the values for  $\sigma_{\text{gr}}$  and  $\varepsilon$  of Che and coworkers [118], the interlayer distance and binding energy of graphite reported by Gould and coworkers are reasonably recovered (3.346 Å vs 3.34 Å and 57 meV/atom vs 48 meV/atom, respectively). The difference between  $d_C^{\text{min}}$  (for the bilayer) and  $d_C$  (for infinite graphite) is only of 1.3%, therefore the spacing of the uppermost layers of a half space of graphite is expected to be close to the value in bulk graphite.

The summation of Eq. (2.43) over a semi-infinite number of layers leads to the non-covalent interaction energy between one carbon atom and a half space of graphitic layers distant by  $d_C$ ,

$$E_{\text{LJ},i}^{(\infty)} = \frac{\pi\sigma\varepsilon}{2} \left[ \frac{\sigma_{\text{gr}}^{12}}{5d_C^{10}} \zeta \left( 10, \frac{d_i}{d_C} \right) - \frac{\sigma_{\text{gr}}^6}{d_C^4} \zeta \left( 4, \frac{d_i}{d_C} \right) \right], \quad (2.44)$$

thereby recovering again the results first obtained by Steele [116]. This expression represents an external potential on the only graphitic layer that is explicitly present in the implicit model for describing GOM.

## 2.5.4 Screening of dispersion forces on metal substrates

Dispersion forces on a metal substrate are screened at long distance owing to electron delocalization [120]. Such non-additive effects can be empirically accounted for by introducing an additional Thomas-Fermi (TF) screening factor into the Grimme D2 model in the case of the interaction with the metal part of the substrate [121–123]:

$$E_{\text{disp}}^{(\text{D2,scr.})} = \sum_{i \in \text{ads}} \sum_{j \in \text{subst}} \frac{-s_6 f_{\text{scr}}(d_i)}{1 + \exp \left[ -20 \left( \frac{r_{ij}}{R_{ij}^2} - 1 \right) \right]} \frac{C_6^{ij}}{r_{ij}^6} \quad (2.45)$$

$$f_{\text{scr}}(d_i) = \exp[-2(d_i/r_{\text{TF}})] \quad (2.46)$$

where  $r_{\text{TF}}$  is the screening length. In the previous equation, the layered structure of the substrate (subst) was explicitly taken into account through the additional and translationally invariant dependence on the distance  $d_i$  between atom  $i$  and the layer to which  $j$  belongs to.

Approximating the substrate by a series of equidistant uniform atomic monolayers with density  $\sigma'$  allows summing over entire layers as before, and the result reads

$$\tilde{E}_{\text{disp}}^{(\text{scr})} = -\frac{s_6 \sigma' C_6 \pi}{2d_L^4} \sum_{i \in \text{ads}} e^{-\frac{2d_i}{r_{\text{TF}}}} L\left(e^{-\frac{2d_L}{r_{\text{TF}}}}, 4, \frac{d_i}{d_L}\right), \quad (2.47)$$

where  $L(z, s, a)$  denotes the Lerch zeta function

$$L(z, s, a) = \sum_{k=0}^{\infty} \frac{z^k}{(k+a)^s}. \quad (2.48)$$

The case without screening of dispersion is recovered for  $r_{\text{TF}} \rightarrow \infty$ , whereas taking  $r_{\text{TF}} = 0$  corresponds to removing the dispersion correction entirely. As was the case previously, the two uppermost layers must be dealt with separately owing to distances shorter than the cut-off, and Eq. (2.39) with the additional screening factor has to be used instead. In this expression the  $C_6$  and  $R_r$  parameters must be chosen appropriately for the pair of subsystems in consideration, which can be adsorbate-graphene, adsorbate-metal substrate or graphene-metal substrate. In addition,  $\sigma$  needs to be replaced by  $\sigma'$  for the second layer. In practice, the Lerch zeta function was evaluated with the `lerch` function of the POLPAK library [124].

As a side note, we emphasize that Eq. (2.47) applies to the dispersion interactions exerted by the semi-infinite metallic substrate on both the metal adsorbate and the epitaxial graphene layer even in absence of any adsorbate.

## 2.6 Simulation tools

The atomistic potential presented in the previous sections was used to explore the structural and energetic properties of adsorbates and epitaxial graphene, and to determine the influence of temperature on its thermal stability and dynamical properties. In the following, we explain how to deal with laterally periodic systems (boundary conditions) and how to construct epitaxial graphene under different commensurability ratios. We also detail the basic methods to locate low-energy structures, and give the general principles of MD simulations.

### 2.6.1 Periodic boundaries

The generic system that has been studied in this work is a substrate with possible adsorbates on its surface. All calculation methods presented in the following for obtaining structural, statistical and dynamical information are used in combination with lateral periodic boundary conditions. The boundary above the surface is left free, while the atoms at the opposite boundary from the lowermost substrate layer are kept immobile. In most cases, three or four substrate layers have been taken into account explicitly.

For the lateral periodic boundaries a rectangular shape has been chosen, always as a multiple of the graphene unit cell with a lattice constant of  $a$ . This means that the height/width ratio naturally assumes  $\sqrt{3}/2$ . Two different ways of joining the simulation box with its periodic images have been employed: If not indicated otherwise, we used a rhombic shape, which is equivalent to a rectangular shape with a brick-like tiling, which is depicted in Fig. 2.5(a,b). Only for the calculations concerning the nickel-carbon system, simple rectangular lateral periodic boundaries were used as schematized on panel (c). The use of periodic boundaries avoids boundary effects, however finite size effects remain and it is always necessary to ensure that

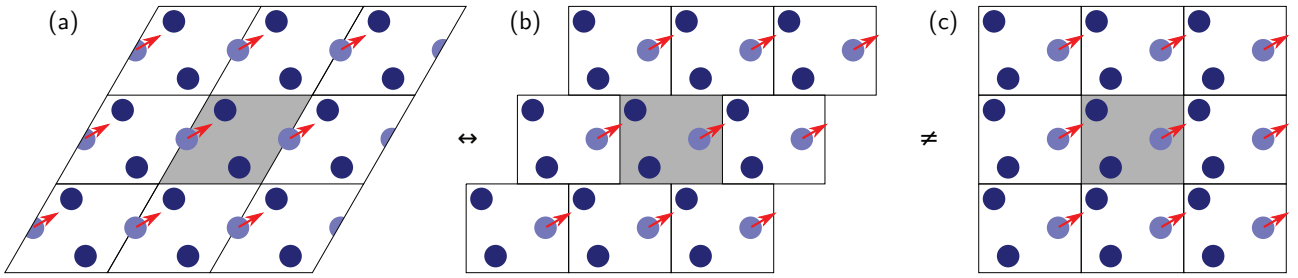


Figure 2.5: Schematic of the lateral periodic boundary conditions used in this work. (a) Rhombic shape chosen as a simulation cell in most cases. (b) Brick-like tiling of a rectangular cell which is equivalent to the rhombic shape. (c) Simple rectangular simulation cell used only in a few occasions for the Ni–C system.

the simulation cell is large enough so that the studied properties do not depend (too much) on the cell size. Especially for calculations involving isolated adsorbates, special care was taken that they do not interact with their periodic images via the Brenner BOP. Still, the use of periodic boundaries always influences the properties of the system because it reduces its spatial symmetries. Isotropy is lost in the directions in which the periodic boundaries are applied, furthermore the homogeneity of space is lost for fixed boundaries. This influences the number of degrees of freedom of the system and should therefore be taken into account notably when applying the equipartition theorem to evaluate the temperature from the averaged kinetic energy.

## 2.6.2 Moiré structures

### Moiré structure geometry of epitaxial graphene

In the context of epitaxial graphene, the use of periodic boundaries requires to find a common simulation cell for the underlying metal and the graphene parts. Many different materials have been experimentally used as a substrate for epitaxial graphene [32, 45]. The present work is restricted to the (111) fcc surfaces of platinum, nickel and iridium and the (0001) hcp surface of ruthenium. Those are all monatomic transition metal surfaces with a equilateral triangular motif. For a common simulation cell it is necessary that an integer number of graphene unit cells  $x \times x$  matches and integer number  $y \times y$  unit cells of the equilateral triangular surface lattice of the metal substrate. We designate a such structure as  $x$  on  $y$  moiré.

In general, it is impossible to find such a cell because the ratio between the lattice constants of the surface metal lattice and of graphene is not rational. This is even more relevant for simulations at finite temperature, since the TECs of the two subsystems are likely to differ. It is thus necessary to apply some strain on one of the two subsystems, which may influence some of the system properties. In particular, graphene has a high inplane stiffness and therefore reacts strongly to such strain by buckling. This paragraph discusses how a simulation cell for epitaxial graphene can be constructed for the general case where inplane angles between the graphene and the metal surface are involved.

### Epitaxial graphene with non-zero inplane angles

For those metal surfaces for which the interaction with graphene is rather weak, domains of different inplane angles are observed experimentally [125–127]. In addition, epitaxial graphene on polycrystalline surfaces leads to domains of different inplane angles even if the interaction is strong. Graphene contains two equivalent equilateral triangular sublattices. It is not possible

to connect one of these lattices to the other when crossing the periodic boundaries. Therefore it is sufficient to consider only one of the sublattices for establishing the simulation cell. The other will then fit automatically into the cell.

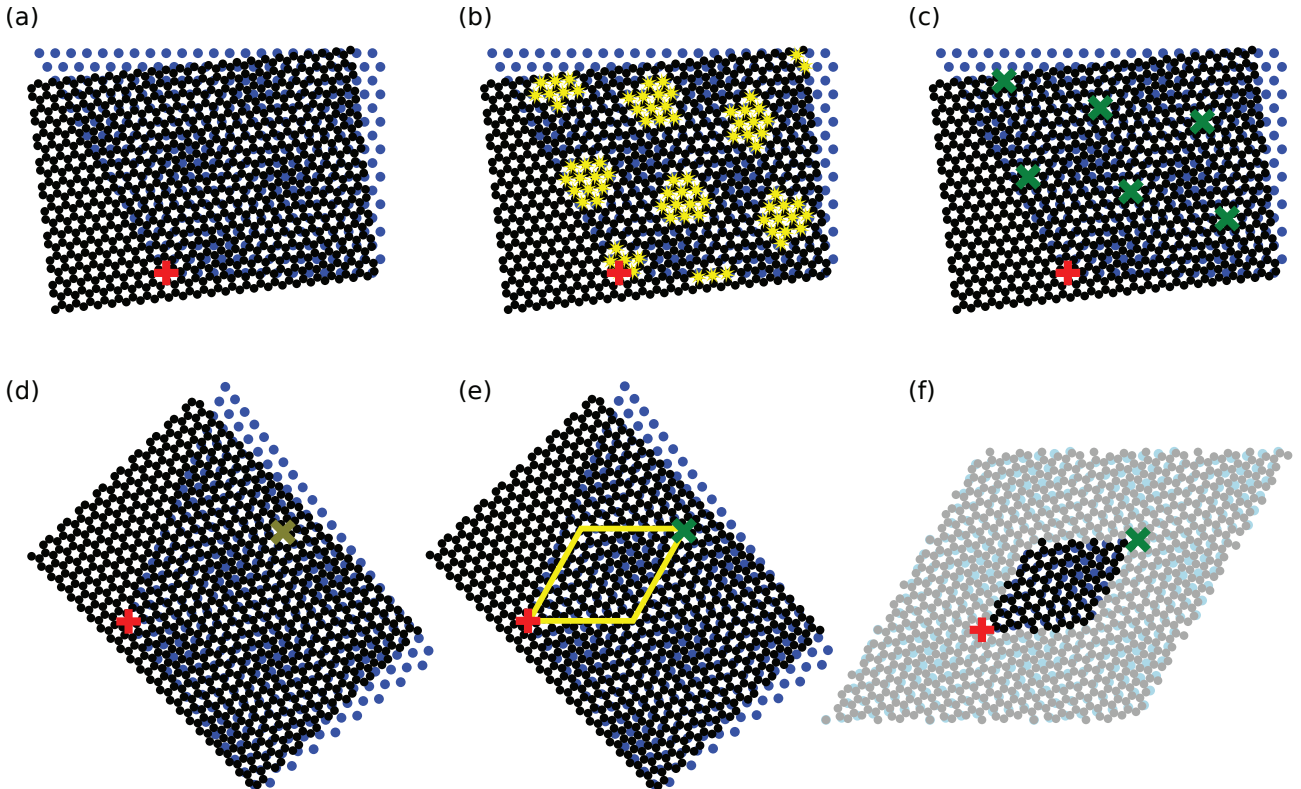


Figure 2.6: Moiré geometry of an epitaxial graphene sheet (represented by black circles) on metal (blue circles) with an inplane angle. The different panels illustrate the procedure that was adopted for the construction of an appropriate simulation cell, as described in the text. (a) Superposition of the hexagonal graphene lattice on a metallic triangular surface lattice at an arbitrary inplane angle. The lattices share a common origin indicated by a red plus; (b) Detection of carbon atoms that are nearly in direct superposition with metal atoms on the basis of a simple distance criterion. Such close concordances are highlighted by yellow stars; (c) The distance criterion is tightened until only one concordance per group is left. These concordances are indicated by green crosses. (d) The inplane angle is precisely adjusted so that the origin and the close concordances on both lattices at the opposite corner of the simulation cell (green cross) are aligned; (e) The graphene lattice is scaled so that the close concordance at the opposite corner of the simulation cell (indicated by yellow lines) becomes an exact one; (f) Final simulation cell surrounded by eight of its periodic images.

### Procedure for the determination of simulation cells for moiré structures

At arbitrary inplane angles, the system is not periodic and therefore no finite common simulation cell can be found. Panel (a) of figure 2.6 shows such a moiré structure at an arbitrarily chosen inplane angle by which the graphene has been twisted around the origin, as indicated by a red plus on the figure. Superficial visual inspection suggests a periodic moiré structure, however a second glance reveals that the structure is rather only quasiperiodic. Experimentally, such quasi-periodic structures may very well be observable, but calculations with periodic boundaries require a common simulation cell (and enforce periodicity anyway). Several authors

have also addressed the determination of commensurate moiré structures in the specific case of epitaxial graphene [128, 129]. In particular, Merino and coworkers [126] followed a similar numerical approach for addressing these issues as presented in the following. We have developed a procedure for the identification of inplane angles that produce truly periodic moiré structures up to a certain system size. Due to the symmetry of the problem (equilateral triangles), the inplane angle can be restricted to the range of  $0^\circ$  to  $30^\circ$ .

In a first step, close concordances of the two lattices, *i.e.* regions where the two lattices are in phase, are identified based on a simple distance criterion and highlighted by yellow stars in panel (b). In the graphene only carbon atoms belonging to the same sublattice as the atom at the origin are taken into account during this search. In a next step, the distance criterion is gradually tightened until only one close concordance per group is left [panel (c)]. These concordances are highlighted by green crosses. It appears that the concordances found this way do not form an exactly periodic superlattice. Therefore only the concordance that is closest to the origin is used for the construction of the simulation cell: the vector connecting the origin forms one of the basis vectors of the moiré and the second basis vector is of the same length but rotated by  $60^\circ$ . Adding both basis vectors to the origin leads to the opposite corner of the moiré on the graphene lattice. However, in general this carbon atom is not precisely superimposed on a metal atom, which would be required for perfect periodicity of the simulation cell. Consequently the inplane angle is adjusted to align this atom with its closest metal neighbor and the origin. Panel (d) shows the resulting new moiré structure with the opposite corner of the structure indicated by a green cross. In addition, the moiré has been rotated so that one of the basis vectors is horizontally aligned. This allows to identify two angles, namely the inplane angle  $\Theta$  between the graphene and the metal lattice and the angle between the graphene lattice and the now horizontally aligned moiré structure. This second angle  $\alpha$  is used in Wood's notation [130] that describes the moiré structure with respect to graphene as  $(k \times k)R\alpha$ , where  $k$  is the edge length of the moiré structure in terms of the graphene lattice constant. Note that there is no general relation between these two angles and they are both needed for the identification of a particular moiré structure. Exact periodicity can be reached in a final step where the graphene lattice is scaled as to superimpose the two lattices (that were already aligned in the previous step) at the corner of the simulation cell, which is highlighted by yellow lines in panel (e). This last step of scaling of the graphene lattice is not necessary if the lattice constants of the metal surface lattice and the graphene are the same, which is a good approximation in the case of graphene/Ni(111). Panel (f) shows the final moiré structure surrounded by eight of its periodic images.

For the determination of all possible such moiré structures the procedure is repeated for inplane angles in the range of  $0^\circ$  to  $30^\circ$ . The inplane angle increment from one trial geometry to the next is chosen small enough in order not to miss possible intermediate structures.

### 2.6.3 Structural optimizations

The problem of local optimization consists of finding the closest minimum in the potential energy surface of a given configuration. It is a relatively simple problem that can be solved by a number of algorithms such as the Nelder and Mead, the Levenberg-Marquardt algorithm and the MC method at zero temperature as discussed above when the gradient of the potential energy is not known. When the gradient is available, several more efficient algorithms exist such as steepest decent, the Broyden–Fletcher–Goldfarb–Shanno (BFGS) and the class of conjugate gradient algorithms. The search of the global minimum is a much more difficult task, because the typical number of local minima of a configuration even with a relatively small number of atoms is astronomic and there is no way of knowing whether a particular minimum is the global

one or not. Yet some methods such as parallel tempering as described above or other global minimizers such as basin hopping [131] or genetic algorithms [132] exist that can be employed for the search of the global minimum. The latter two in turn depend on local optimizers that they make use of in a systematic way.

In this section, we present the local minimization strategy used in this work for obtaining geometrical properties such as bond lengths and angles or differences of potential energies of two or more geometries. Compared to the evaluation of properties at finite temperature, this local geometry optimization is much faster and therefore commonly used in situations where the evaluation of the energy is time consuming, as is the case for calculations employing an explicit description of electronic structure.

The conjugate gradient method stands as one of the algorithms that are particularly efficient when the analytical expressions for the gradient of the potential energy are known, which is the case for the empirical potentials described above. When the algorithm is started, it searches a line minimum along the gradient  $g$  calculated for the initial geometry. Then, instead of following the gradient  $g'$  calculated at the new position (as in steepest-descent minimization), it is more efficient to update the search direction using a conjugate gradient formula, which allows to construct an approximation of the curvature of the energy surface close to the minimum. We use the Polak-Ribiere formula

$$p' = -g' + \beta p, \quad (2.49)$$

where

$$\beta = |g' \cdot (g' - g)| / |g|^2 \quad (2.50)$$

for the determination of the new search direction  $p'$ , as implemented in the `gsl_multimin_fdfminimizer_conjugate_pr` function of the GNU Scientific Library. If the potential energy surface is harmonic, the solution is found by repeating the line searches along updated search directions in a number of steps equal to the dimensionality  $N$  of the problem. However, in the case of local structure optimization, the energy surface is usually not harmonic and therefore the line search directions need to be reset to the gradient from time to time, at least after  $N$  iterations. This is repeated usually until the norm of the gradient is below a certain threshold. Further technical details about this method are discussed for example in Ref. [133].

In this work, the conjugate gradient method found application in several contexts: It allowed for comparison with literature results that employed more detailed models. Furthermore it was used for exploring quickly the energy surfaces of a large number of initial geometries as well as for determining geometric and energetic properties of larger systems. Additional applications include the preparation of initial geometries for MD simulations and the determination of suitable geometries for subsequent normal mode analysis.

In theory, the only minimum of interest is the global minimum, which corresponds to the only configuration that is classically realized at zero temperature. However, sometimes the global minimum is not the most physically relevant, because it might be separated by high energy barriers from the initial geometry (which is chosen to be similar to the experimentally observed structure). Depending on the barrier height, the system may never reach this geometry even on experimental timescales. Furthermore, the global minimum is not necessarily observed experimentally, because temperature effects may stabilize other higher-lying isomers (entropic stabilization).

### 2.6.4 Molecular dynamics

In order to derive physical properties at finite temperature from the interaction potentials, the method of MD may be employed when the gradients of the total cohesive energy are available. The advantage of MD over MC simulations is then that the former give access to the dynamical properties of the system, such as diffusion dynamics or vibrational spectra. The idea of classical MD is to integrate numerically Newton's equations of motion for all atoms in the system and to calculate the properties along the trajectory generated in phase space. Due to the Lyapunov instability, these trajectories are generally chaotic, *i.e.* trajectories of two systems with nearby initial conditions diverge exponentially in the course of time. This is not necessarily a problem since the aim is not to predict the precise trajectory for a given initial condition, but to sample a certain statistical ensemble. It can even be seen as an advantage, because due to this chaotic behavior the system may explore more of the phase space, which is demanded by the ergodic hypothesis [111]. This hypothesis states that the time averages that are calculated in MD are equal to the ensemble averages that are assumed to be observed experimentally. The idea is that if the system evolves long enough it will eventually reach all possible microstates.

Therefore, throughout a MD simulation a variety of quantities of interest that need to be expressed as a function of microscopic variables can be calculated as time averages. The long time average  $\langle A \rangle$  of observable  $A$  is expressed as:

$$\langle A \rangle = \lim_{t \rightarrow \infty} \frac{1}{t} \int_0^t A(t') dt' \quad (2.51)$$

Since the equations of motions are numerically integrated in a stepwise manner, this equation is replaced by a discrete sum and the averages become more and more precise as the number of integration steps increases and a sufficient number of representative configurations of the ensemble are generated.

#### Integration

Starting from a certain initial configuration, that is obtained as detailed below, MD simulations relies on the integration of Newton's equation of motion with respect to the time  $t$ :

$$\vec{f}_i = m_i \cdot \frac{d^2 \vec{r}_i}{dt^2} \longrightarrow \vec{r}_i(t) \quad (2.52)$$

The coordinates of atom  $i$  of mass  $m_i$  are  $\vec{r}_i$  and the force  $\vec{f}_i$  acting on it is calculated as the negative gradient of total potential energy  $V_{\text{tot}}$ .

The integration of Newton's equations of motion in the simulations is achieved by means of the velocity Verlet scheme. It is not only simple and fast, but it also displays long-term energy conservation. The latter is important, as this property ensures that the system stays in the intended microcanonical ensemble. Higher-order schemes may guarantee a higher short time precision, but often they produce a long-term energy drift, which makes them less valuable for MD. Another interesting property is that the generated trajectories are time-reversible (symplectic). This holds of course only within the numerical precision, but it is independent of the length of the time step [111].

The velocity Verlet integrator is given by the following set of equations, where  $\vec{v}_i$  designates the velocity vector of atom  $i$  and  $dt$  the time step.

$$\vec{r}_i(t + dt) = \vec{r}_i(t) + \vec{v}_i(t)dt + \frac{\vec{f}_i(t)}{2m_i}dt^2 \quad (2.53)$$

$$\vec{v}_i(t + dt) = \vec{v}_i(t) + \frac{\vec{f}_i(t + dt) + \vec{f}_i(t)}{2m_i}dt \quad (2.54)$$

The error is  $\mathcal{O}(dt^4)$  for both positions and velocities.

### Nosé-Hoover thermostat

Solving the equations of motion cited above leads to the conservation of energy and the sampling of the microcanonical ensemble. Now we consider a system in equilibrium with a thermostat that determines its temperature. In MD, various methods exist to achieve this goal of not only imposing a temperature, but also generating configurations that rigorously follow canonical statistics. For the simulations presented in this work the choice fell on the deterministic Nosé-Hoover thermostat. It allows to drive the system to an imposed temperature and maintain it there. More importantly, this type of thermostat generates configurations that follow the canonical distribution [111]. It should be noted that also in the canonical ensemble temperature fluctuations occur for finite systems. Therefore, in contrast to simple velocity rescaling thermostats, where the total kinetic energy is a conserved quantity, the instantaneous temperature of a system in contact with the Nosé-Hoover thermostat fluctuates. For the Nosé-Hoover thermostat these fluctuations follow the real canonical fluctuations.

In contrast to the Andersen or Langevin thermostats that also correctly reproduce canonical statistics, the Nosé-Hoover thermostat is time-reversible and deterministic [111]. An extra variable with a coordinate  $s$  and momentum  $p_s$  is added to model the heat bath, interacting with the physical system through a specific potential designed in such a way that the canonical ensemble at a given temperature is sampled. The Nosé-Hoover thermostat features one parameter which corresponds to the inertia  $Q$  of the heat bath that can be seen as a coupling strength. The numerical value of this coupling parameter is important for the efficiency of the thermostat and must therefore be chosen with care. The equations of motion for the system in contact with the Nosé-Hoover thermostat read [110]:

$$\frac{d\vec{r}_i}{dt} = \frac{\vec{p}_i}{m_i} \quad (2.55)$$

$$\frac{d\vec{p}_i}{dt} = -\frac{\nabla_i V_{\text{tot}}}{m_i} - \frac{p_s \vec{p}_i}{Q} \quad (2.56)$$

$$\frac{dp_s}{dt} = \sum_i \frac{\vec{p}_i^2}{m_i} - f k_B T \quad (2.57)$$

$$\frac{ds}{dt} = \frac{p_s}{Q} \quad (2.58)$$

The target temperature of the thermostat is designated by  $T$ , which appears together with the Boltzmann constant  $k_B$  and the total number of degrees of freedom of the system,  $f$ , while  $\vec{p}_i$  designates the momentum of atom  $i$ .

The entire system including the thermostat is again found to sample a microcanonical ensemble. This property allows the definition of a conserved quantity, namely the following extended

Hamiltonian [110]:

$$H_s = V_{\text{tot}} + \sum_i \frac{p_i^2}{2m_i} + \frac{p_s}{2Q} + fk_B T s. \quad (2.59)$$

The conservation of this quantity can therefore be used to validate the simulation code.

In practice, the integration scheme for this thermostat is also of the velocity Verlet form, and was taken from Ref. [134]. The main difference with the original microcanonical version is a slightly more complicated evaluation of velocities, owing to their explicit presence as a damping force in the equations of motion. They must be solved self-consistently given the thermostat variables.

## Initialization

The MD procedure usually begins with an initialization process where a configuration at equilibrium at zero temperature is prescribed and random initial velocities are assigned to each atom. The velocities are to be rescaled according to the equipartition theorem so that one can already impose at the beginning an approximate temperature to the system. However, in the microcanonical ensemble one should use a temperature about twice as high as desired, because about half of the kinetic energy will be transformed into potential energy in the equilibration part of the simulation. This is not strictly exact if the interaction potential is anharmonic, which is usually the case, but this method can put the system at least in the vicinity of the target temperature. Later on, in the course of the simulation the temperature can be determined also via the equipartition theorem, which assigns to a given total kinetic energy  $E_{\text{kin}}$  a temperature value  $T$  such that

$$E_{\text{kin}} = \frac{1}{2} \sum_i m_i (v_{ix}^2 + v_{iy}^2 + v_{iz}^2) = \frac{f}{2} k_B T. \quad (2.60)$$

Here  $v_{i\alpha}$  is the component  $\alpha$  of the velocity vector of atom  $i$ ,  $f$  is the number of degrees of freedom of the entire system. It should be noted that  $f$  depends on the presence of the substrate: For a system without interaction to the substrate there are  $3N - 6$  degrees of freedom,  $3N$  for the atoms minus six that are lost to the conservation of linear and angular momenta.  $3N$  degrees of freedom are found for the system in interaction with a fixed substrate layer, since in this case all spatial symmetries are broken.

## 2.7 Observables

Along the MD and MC simulations it is possible to extract quantities that are based on the microscopic variables of the system. In this work we were mainly interested in the effect of temperature on adsorbates in contact with carbonaceous substrates. This behavior is quantified by the following dynamical indicators, while the shape of the adsorbates was monitored by an asphericity index. Furthermore, in the case of MD simulations, the thermal stability of adsorbates was further characterized by surface diffusion coefficients. In addition, vibrational spectra were calculated in order to gain insight into the anharmonicities of the atomistic potentials and to allow, to a certain extent, for comparison with experimental Raman spectra.

### 2.7.1 Lindemann indices and adsorbate shape

The thermal stability of adsorbates may be evaluated based on the root mean square bond length fluctuation of selected atomic pairs. The intrinsic rigidity within the particles can be measured by

$$\delta_{\text{intra}} = \frac{1}{N(N-1)} \sum_{i \in \text{ads}} \sum_{\substack{j \in \text{ads} \\ j \neq i}} \frac{\sqrt{\langle r_{ij}^2 \rangle - \langle r_{ij} \rangle^2}}{\langle r_{ij} \rangle}, \quad (2.61)$$

where  $N$  is the number of atoms in the adsorbate and  $\langle \cdot \rangle$  a time average. Similarly the global mobility of the adsorbate relative to its substrate can be evaluated by the index

$$\delta_{\text{inter}} = \frac{1}{N \cdot M_1} \sum_{i \in \text{ads}} \sum_{\substack{j \in \text{subst} \\ 1^{\text{st}} \text{layer}}} \frac{\sqrt{\langle r_{ij}^2 \rangle - \langle r_{ij} \rangle^2}}{\langle r_{ij} \rangle}, \quad (2.62)$$

$M_1$  denoting the number of atoms in the upper layer of the substrate.

At low temperature, where both the substrate and adsorbate vibrate around their equilibrium positions, the interatomic distances only exhibit some minor fluctuations and the two indices keep low values, typically below a few percents. Conversely, an index exceeding approximately 10–15% indicates some qualitative motion of the atoms within the adsorbate (fluxional or liquid state detected on  $\delta_{\text{intra}}$ ) or relative to the substrate (global diffusion detected on  $\delta_{\text{inter}}$ ).

In addition to these dynamical indicators, the shape of the adsorbate was quantified from the principal momenta of inertia  $A \geq B \geq C$ , from which an asphericity index is defined as

$$\chi = 3(2A - B - C)/2(A + B + C). \quad (2.63)$$

The NPs deposited on the substrate are initially symmetric (truncated octahedra with  $\chi = 0$ ), and variations in shape are directly manifested on  $\chi$ . By construction,  $\chi$  is always positive and deviates from zero as the system increasingly deforms, values reached for oblate deformations ( $A \gg B \simeq C$ ) being higher than for prolate deformations ( $A \simeq B \gg C$ ). When interested in equilibrium properties that do not depend on time, the statistics for the quantity in question becomes better as the simulation time increases. A major change in the average of such a quantity in the course of the simulation would indicate that the system is not in equilibrium.

### 2.7.2 Surface diffusion coefficients and activation energy

In the case of MD simulations, the adsorbate mobility can be quantified further by the calculation of diffusion coefficients. Care should be taken when a thermostat is present as it is not clear how much the thermostat influences dynamical properties like diffusion constants. In order to minimize this effect, we never applied the thermostat directly to the adsorbates and in most cases, when several substrate layers were simulated, also the surface layer was not subjected to the thermostat. The surface diffusion coefficient  $D$  may be evaluated from the long time variations of the mean square displacement (MSD) of the adsorbate center of mass (com)  $\vec{r}_{\text{com}}$  as

$$D = \lim_{t \rightarrow \infty} \frac{1}{4t} \langle [\vec{r}_{\text{com}}(0) - \vec{r}_{\text{com}}(t)]^2 \rangle, \quad (2.64)$$

where the angular brackets specifically indicate here an average over equilibrated initial configurations at time  $t = 0$ . For the data presented in this work, the MSD was evaluated over time windows of 20 ps, and the long-time regime was considered to be reached over the last 40% of

the time window. Often the diffusion process follows the following Arrhenius type law:

$$D \approx D'_0 e^{-E_{\text{act}}/(k_B T)} \quad (2.65)$$

where  $E_{\text{act}}$  is the activation energy of the surface diffusion process,  $k_B$  the Boltzmann constant and  $D'_0$  a system specific constant prefactor.

### 2.7.3 Vibrational spectra

The vibrational spectrum was calculated from the Fourier transform of the velocity time autocorrelation function  $C_{vv}(t) = \langle \vec{v}(t) \cdot \vec{v}(0) \rangle$ . At low temperature, the system should behave as a collection of harmonic oscillators. The harmonic vibrational frequencies of the global system were calculated from the diagonalization of the mass-weighted Hessian matrix at the locally relaxed position. The second derivatives necessary for the determination of the matrix were obtained by numerical differentiation of the analytical gradient. Comparing the spectra obtained via the velocity autocorrelation function at low temperatures with the normal mode spectra thus provides a consistency check of the simulation code. The spectra contain all frequencies of the system, on the basis of the underlying potential, however without the knowledge of the dipole moments or polarizabilities, it is unclear which of the modes are active in an infrared or Raman spectrum.



# Chapter 3

## The platinum-carbon system

As a first application of the general methodology exposed in the previous chapter, these ideas are tested in the specific case of platinum NPs deposited on graphene, graphite, and graphene epitaxially grown on Pt(111). For the Pt-C system a BOP is already available, as parametrized by Albe and coworkers using a combination of experimental and theoretical data [96], so our contribution to the overall potential is to account for long-range dispersion forces.

The model thus obtained can be validated against electronic structure calculations available for several static structures. Using systematic optimizations at zero temperature, the relative stability of various NP shapes on their support could be determined for adsorbates containing several thousand atoms. At finite temperature, MD simulations shed light on the thermal behavior and emphasize the key role of dispersion forces on the stabilization of the adsorbates. The vibrational properties of graphene layers in contact with a Pt NP or epitaxially grown on Pt(111) could also be determined, revealing some clear sensitivity on temperature and strain.

### 3.1 Introduction

Platinum NPs interacting with carbon substrates have become an active field of research due to numerous potential applications in catalysis [26–28, 135] or in hydrogen-based technologies [136]. One motivation is clearly to exploit the high surface/volume of NPs in order to reduce the amount needed of this expensive metal. Platinum NPs have notably been used in fuel cells as catalysts for oxygen reduction but also for promoting hydrogen oxidation at low temperature [26, 27, 137]. Pt NPs have also been shown to enhance the hydrogen storage capacity of carbon porous nanomaterials [136]. By favoring dissociative chemisorption of hydrogen at their surface, NPs contribute to diffuse hydrogen toward adjacent surfaces, a process commonly referred to as hydrogen spillover. The selective permeability of graphene toward thermal protons but not to molecular hydrogen has recently been found to be further increased by platinum adsorbates [138]. All these applications need well distributed and stable assemblies of Pt clusters, which in turn requires that the mechanisms of formation and adsorption of such nanomaterials to be fully understood.

The aforementioned applications involve extended substrates, for which the problem of dispersion forces is particularly important. In this chapter we apply and evaluate the dispersion models evaluated in the previous chapter. For the Pt-C system a Brenner BOP parametrization is already available for modeling the metallic and covalent interactions, thus allowing us to focus on the specific role of dispersion forces. The purpose of this chapter is therefore to critically discuss the importance of dispersion interactions on the physical behavior of platinum NPs on a variety of ordered carbon substrates ranging from graphene to multilayer graphite

and epitaxial graphene on Pt(111). The various coarse-grained models we are proposing here were adapted to these different situations, and compared against all-atom calculations at zero and finite temperature on various observables such as adsorption energies, dynamical indicators of rigidity and the vibrational spectra. One main conclusion is that dispersion forces contribute significantly to the adsorption energy and that the uppermost layers of the substrate dominate this contribution.

Different variants of the dispersion model were compared on simple test cases and for more realistic adsorbates on graphite at finite temperature in section 3.3. The model was further extended in section 3.4 to describe the specific interactions of epitaxial graphene on Pt(111) possibly acting as a substrate for Pt NPs, and again at zero and finite temperatures. Our results here emphasize the importance of screening and non-additivity of the van der Waals interactions on the resulting dynamical behavior. Finally, in section 3.5 we summarize the most important conclusions.

## 3.2 Computational details

The different dispersion models presented in the previous section have been compared against each other for various adsorbates on several substrates. All simulations employed periodic boundary conditions along the two lateral dimensions. In the static limit, Pt NPs containing between 1 and several thousand atoms were locally optimized starting from high-symmetry morphologies such as multilayer icosahedra or truncated octahedra (Wulff shapes). For both types the NPs were initially deposited in epitaxy on the graphite substrate, exposing their (111) facets to the honeycomb lattice. From those structural optimizations, adsorption energies and geometry relaxations could be quantified.

In addition to these static investigations, MD simulations at finite temperature were conducted to assess the thermal stability and dynamical properties of adsorbates on their carbonated substrates. Here we used a combination of methods to simulate the real time dynamics, essentially MD at finite temperature imposed by coupling a Nosé-Hoover thermostat to the substrate. In order not to alter the time-dependent properties, thermostatting was not applied to the subsystem of interest (adsorbate or upper layer in the case of epitaxial graphene), but to the remaining substrate only.

MD trajectories for 64-atom NPs on substrates kept at a fixed temperature were initiated from locally relaxed structures occupying a two-layer configuration similar to experimentally observed NPs formed *in situ* on epitaxial graphene on (111) metal surfaces [19, 25, 139, 140]. Various observables were calculated in order to probe the intrinsic mobility of the NPs, their possible diffusion on the substrate as well as their spontaneous rearrangement toward lower-energy structures. Vibrational spectra were also evaluated from the Fourier transform of the velocity time autocorrelation function. Unless otherwise mentioned, all MD trajectories employed a time step of 1 fs and were carried out over 5.5 ns, the first 500 ps being discarded from the averages for equilibration purposes.

For the static computations of the smaller Pt adsorbates on graphite the periodic boundaries contained  $15 \times 15$  graphene unit cells, unless otherwise mentioned, and for the larger Pt adsorbates (from 923 atoms on)  $30 \times 30$  unit cells. In the case of the MD simulations of Pt<sub>64</sub> clusters on (possibly defective) graphite a simulation box of  $10 \times 10$  graphene unit cells was chosen. It was made sure that these simulation boxes are large enough for the adsorbates to not interact with their periodic images, *i.e.* the cell width is larger than the diameter of the adsorbate plus the cut-off of the covalent interatomic potential. Regarding epitaxial graphene on Pt(111), the size of the simulation cell is imposed by the periodicity of the moiré and varies as a function of

the inplane angle between the graphene and the Pt lattice, as discussed in section 3.4. At large inplane angles, larger sizes were simulated in order to circumvent the problem of small primitive cells. All calculations using explicit dispersion models such as Grimme D2 and D3 employed three graphene slabs in the case of graphite (ABA fashion), and three metallic slabs in the case of epitaxial graphene on Pt(111) (ABC fashion) independently of the dispersion model. Rigid boundary conditions were applied to the bottom layer in the MD simulations and local optimizations. In the implicit description of graphite, the rigid boundaries were released and only the uppermost graphene layer was included as it contributes to possible covalent interactions.

In order to determine the ability of the present dispersion models to describe the interaction of such particles on pristine graphite, we start by defining the adsorption energy of a general adsorbate or nanoparticle (np) on its substrate (sub) through  $E_{\text{ads}} = E_{\text{total}} - E_{\text{sub}} - E_{\text{np}}$ , where  $E_{\text{total}}$  is the energy of the entire system after relaxation,  $E_{\text{sub}}$  and  $E_{\text{np}}$  the potential energies of the relaxed substrate and nanoparticle, respectively.

### 3.3 Pt NPs on pure carbonated substrates

In this section we discuss the most straightforward case of purely graphitic substrates containing one (graphene) or an infinite number (graphite) of monolayers.

#### 3.3.1 Comparison of dispersion models: the adatom case

The performance of the different interaction models was first assessed on static properties involving the local relaxation of adsorbates on the substrates. In the simplest case of single Pt adatoms adsorbed on graphene and graphite, various interaction sites are illustrated in Fig. 3.1. The alpha and beta sites are found on top of a carbon atom and differ from each other only once multiple graphene layers are taken into account. Such differences are only relevant in the explicit models, however they were found to be negligibly small and the two sites will be considered as equivalent here. The bridge and hollow positions lie above the midpoint of a C-C bond and the center of a 6-membered carbon ring, respectively.

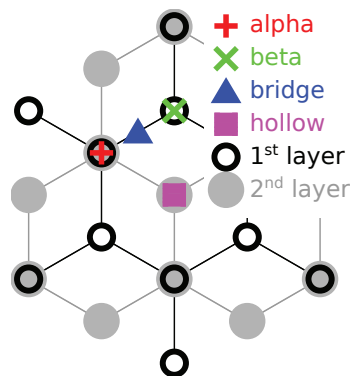


Figure 3.1: High-symmetry adsorption sites of adatoms on graphite: The atoms of the uppermost graphitic layer are represented as black rings, the atoms of the layer below as gray circles. In the implicit models the alpha and beta sites are equivalent.

Energy profiles were calculated for Pt adatoms approaching perfectly flat graphene and graphite surfaces containing laterally  $10 \times 10$  graphene unit cells vertically at these various sites. Here, the substrate atoms were kept fixed to their optimized positions without adatom.

It should be noted that the distance of the adatom to the graphitic layer differs from the smallest Pt-C separation in the case of the bridge and hollow sites.

The variations of the energy profiles with atom-substrate distance are represented in Fig. 3.2 for the three relevant adsorption sites and for the graphene and graphite substrates, with a reference energy assigned at infinite separation. For both substrates, correcting for dispersion

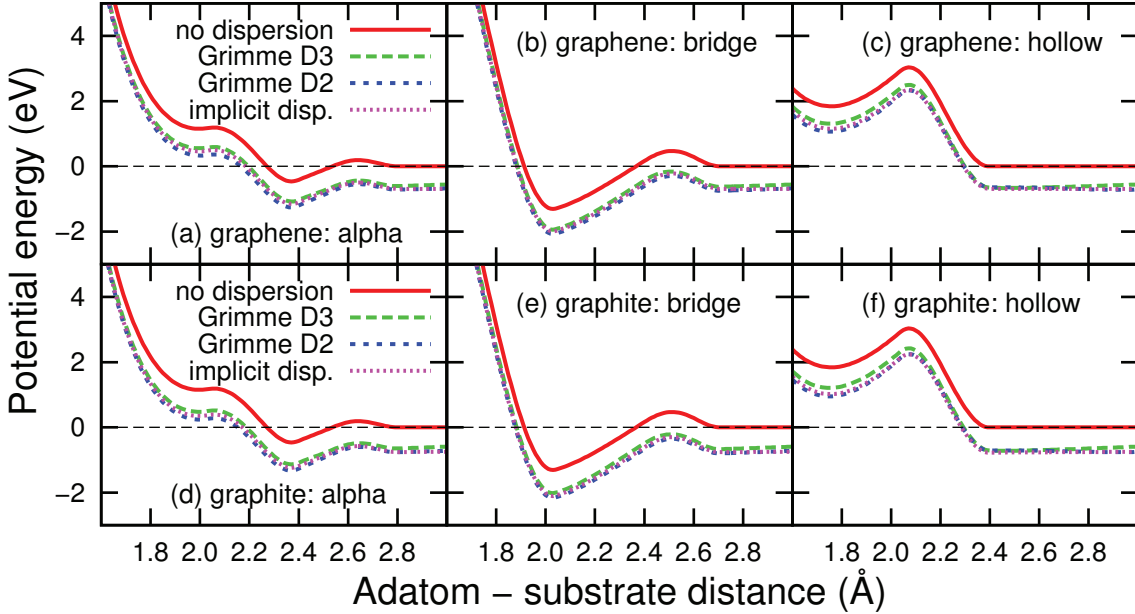


Figure 3.2: Energy profiles of a Pt adatom approaching flat graphitic surfaces along various sites, as obtained from the BOP corrected with different dispersion models. Upper panels (a-c): single-layer graphene; Lower panels (d-f): semi-infinite graphite.

forces further binds the adatom by 0.5–1 eV depending on the model, and introduces a shallow long-distance van der Waals minimum close to the cut-off of the covalent part of the potential, which is at 2.8 Å. This minimum should be considered as a physisorbed state.

Comparing the curves obtained with the Grimme D2 model and the implicit dispersion model, the implicit model appears to work particularly well in this simple test case where the assumption of an uncorrugated substrate surface is strictly satisfied. The minor discrepancies between the Grimme D2 and D3 models can be explained based on the varying coordination of the adatom as it approaches the substrate: adsorption on an alpha/beta site produces a singly coordinated Pt atom, whereas the adatom is two- and sixfold coordinated at the bridge and hollow sites, respectively. Within the D3 model, higher coordinations tend to decrease the  $C_6$  coefficients accordingly, which explains the slight attenuation of the van der Waals energy at short distances for hollow sites with respect to the D2 model. Those observations are valid for both substrates, and unsurprisingly the profiles obtained for graphene and graphite look very similar. Further inspection indicates that, as they should, the chemisorbed minima are slightly more bound in graphite by 86, 107, and 130 meV for the alpha, bridge, and hollow sites, respectively, as the result of additional dispersion forces. Those values for the implicit model are consistent with those obtained with the Grimme D2 model (namely 66, 88, and 111 meV), the 20 meV difference arising from the neglect of van der Waals forces beyond the simulation supercell in the Grimme approach.

The main conclusion of Fig. 3.2 is the very satisfactory performance of the implicit dispersion model to describe the global long-range London forces for Pt atoms on both graphene and semi-

	Single vacancy	Stone-Wales site A	Stone-Wales site B
No dispersion			
$E_{\text{ads}}$ (eV)	-6.46	-2.61	-2.63
$d_{\text{C,Pt}}$ (Å)	1.97	2.04	2.05
Grimme D2			
$E_{\text{ads}}$ (eV)	-7.10	-2.92	-3.06
$d_{\text{C,Pt}}$ (Å)	1.98	2.05	2.06
Grimme D3			
$E_{\text{ads}}$ (eV)	-7.18	-2.76	-2.91
$d_{\text{C,Pt}}$ (Å)	1.97	2.05	2.05
Implicit model			
$E_{\text{ads}}$ (eV)	-7.44	-3.33	-3.38
$d_{\text{C,Pt}}$ (Å)	1.97	2.04	2.05

Table 3.1: Adsorption of a Pt adatom on defective graphite: Adsorption energy  $E_{\text{ads}}$  and closest distance  $d_{\text{C,Pt}}$  between the Pt atom and a C atom. In the case of the Stone-Wales defect, adsorption sites A and B are indicated in Fig. 3.3(c).

infinite graphite, as well as the clear presence of chemisorbed and physisorbed minima separated by well defined barriers.

### 3.3.2 Pt adatoms on defective graphite

Defects on surfaces can have a significant influence on the structural and dynamical properties of adsorbates and can be tailored to trap them and even promote self-assembly [141]. The role of defects on the adsorption of a Pt adatom on a graphitic surface has been investigated with the present explicit (Grimme D2 and D3) and implicit dispersion correction models, as well as without any such correction. Two defects were considered here, namely a single vacancy and a topological Stone-Wales (5775) defect. For both defects the graphitic surfaces were locally reoptimized, and the adsorption of a Pt adatom above the defective substrate was monitored as a function of its lateral position, the distance of the adatom perpendicular to the surface being optimized in the process (but at fixed substrate geometry). For the static computations of Pt-adatoms on defective graphite a simulation box containing  $5 \times 5$  graphene unit cells was employed.

The resulting energy landscapes obtained with the explicit D2 and the implicit dispersion models are shown in Fig. 3.3 for both defects. In the case of the vacancy a strong minimum is found away from the uppermost graphitic layer, originating from the longer Pt-C bond compared to C-C bonds. For the Stone-Wales defect, four equivalent energy minima denoted A in Fig. 3.3(c) are found at a bridge position of the 7-membered rings connecting to hexagons, and four other equivalent minima denoted B can be defined at the alternative bridges connecting to pentagons.

To better evaluate the relative energies of the various adsorption sites, full relaxations of the substrate and adatom were carried out with the D2, D3, and implicit dispersion corrections. The results of these optimizations for the adsorption energy and lowest Pt-C distance are summarized in Table 3.1.

Regarding the Stone-Wales defect, site B turns out to be the most stable for all dispersion correction models. As was the case for adsorption on perfect substrates, additional dispersion in

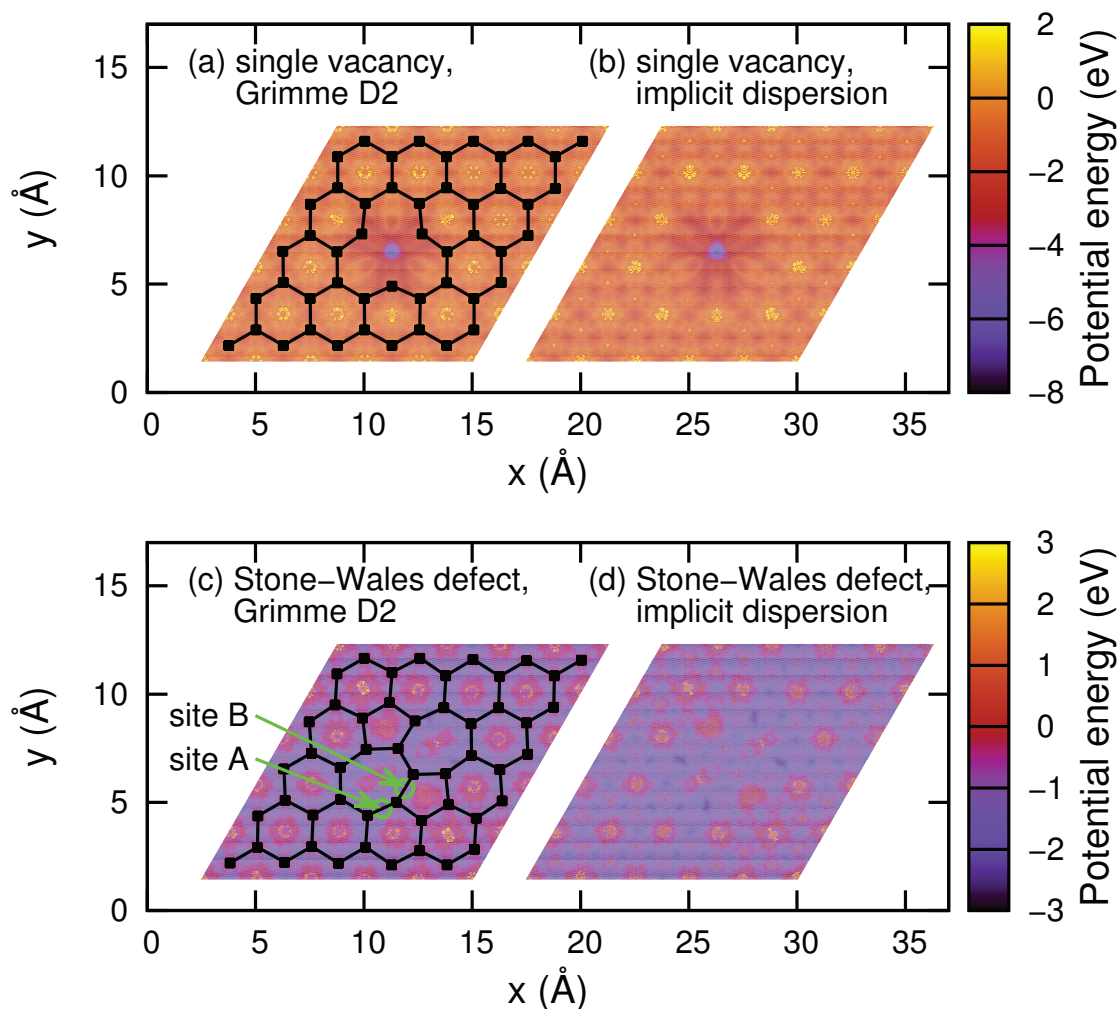


Figure 3.3: Potential energy of a Pt adatom on a graphite surface with a single vacancy (upper panel) or a 5775 Stone-Wales defect (lower panel) as obtained with the explicit D2 and implicit dispersion models. The defective carbon lattice is explicitly shown for the D2 model. For the Stones-Wales defect, two adsorption sites A and B are highlighted as defined in the text.

graphite relative to graphene further strengthens the interaction energies in presence of defects, by about 0.1 eV according to the implicit dispersion model. Based on those results, defects of both types at the uppermost graphite layer are expected to bind Pt adsorbates more strongly than pristine graphite.

### 3.3.3 Interaction of larger adsorbates

Metal NPs can be prepared in the gas phase before their subsequent transfer on substrates [37, 142–144]. Such particles can be quite large, and sustain a much more significant binding to the substrate than single adatoms. Regular icosahedral and truncated octahedral (Wulff) NPs display (111) facets that make them highly stable [145] and compatible with epitaxial deposition on ordered graphite substrates, although such a deposition involves some notable strain owing to the different lattice constants in platinum (bond distance of 2.8 Å) and in carbon (2.5 Å). Fig. 3.4 shows the adsorption energy of such NPs deposited on graphene and graphite and locally optimized from an initial configuration with the metal atoms lying on top of the most stable bridge sites, using different dispersion models. Adsorbates containing

between 13 and 3871 atoms, or between one and eleven icosahedral shell and as many as six truncated octahedral shells were considered here. In the original BOP without any dispersion

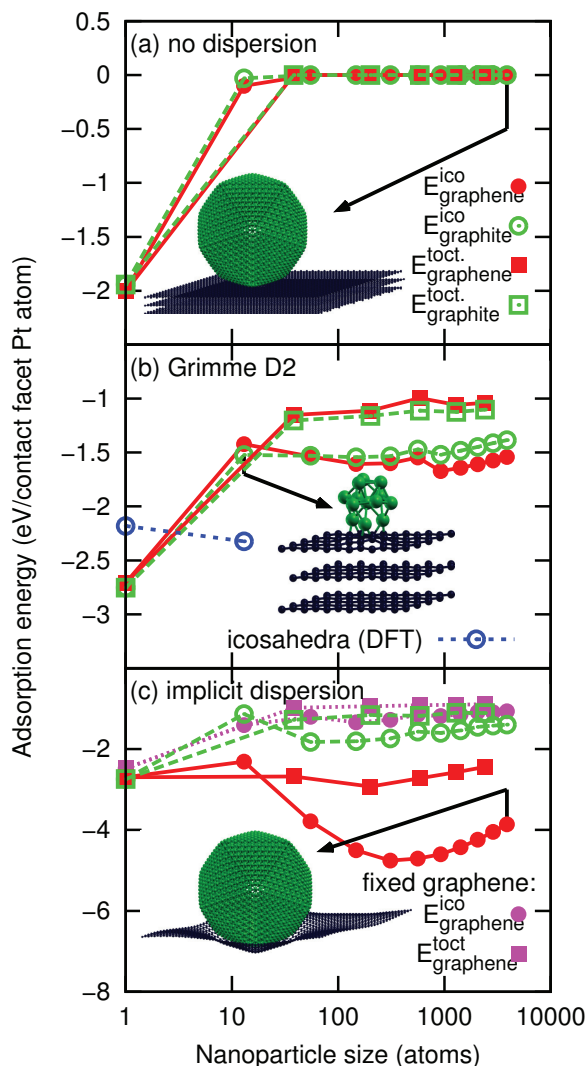


Figure 3.4: Adsorption energies of Pt NPs on graphene and graphite, computed for different treatments of dispersion forces, and normalized by the number of metal atoms in contact with the substrate. (a) No dispersion correction; (b) Explicit correction (Grimme D2); (c) Implicit dispersion model. The adsorption energies, as defined in the text, for graphene and graphite are denoted by full and empty symbols, respectively. Icosahedral (ico) and truncated octahedral (toct) adsorbates are indicated by circles and squares, respectively. Available DFT results have been superimposed in panel (b) [39].

correction, only the single adatom and the 13-atom icosahedron appear stable. The chemical interaction with the substrate distorts  $\text{Pt}_{13}$  significantly, the mutual distances between the three atoms in contact with the uppermost graphitic layer being increased from 2.7 Å for the free  $\text{Pt}_{13}$  to 3.3 Å upon deposition. Similar deformations are found if deposition occurs on alpha/beta sites, however no major distortion occurs at the hollow site. Those conclusions are essentially unchanged once dispersion corrections are accounted for. For this small 13-atom cluster the rather large distortion leads to a relatively small adsorption energy when compared to the larger NPs, because most of the interaction energy is consumed for deformation (about

42% for the Grimme D2 and 55% for the implicit model as compared to an average of 13% and 14% for larger icosahedra). The closest distance between the adsorbate and the substrate is in the 2.0–2.1 Å range in the case of the adatom and Pt<sub>13</sub>. This distance increases up to slightly below the cut-off of the Pt-C Brenner potential for the larger adsorbates, as a response to the repulsive part of the covalent potential close to the cut-off.

Epitaxial alignment on the bridge sites is essentially lost for the larger clusters, with a slight preference for the hollow site in the case of the 55-atom icosahedron. As the NPs become larger, the mismatch in the lattice constants between Pt(111) and graphite(0001) results in some excessive strain that the NPs cannot accommodate well. For these larger clusters, the adsorption energy is roughly proportional to the number of atoms at the facet in contact with the substrate. The slight weakening in adsorption seen in Fig. 3.4(b,c) is due to the decreasing fraction of less coordinated atoms at the edge of the facet in contact. We attribute the weaker interaction per interface atom in truncated icosahedra to their higher area exposed in contact with the substrate. If the implicit dispersion model uses the average position  $\bar{z}$  from the carbon atoms in the simulation cell, the planar approximation may break down for large adsorbates due to excessively large deformations and the tendency to minimize the global interaction. This in turn introduces some dependence of the results on the size of the simulation supercell. Therefore, a large box of  $30 \times 30$  graphene unit cells has been used for the implicit dispersion model. This issue, which is illustrated in the inset of Fig. 3.4(c), can be tackled by fixing vertically the graphene layer during the minimizations. Repeating the minimizations with the implicit model under this constraint leads to better behaved adsorption energies also shown in Fig. 3.4(c), however the need for this trick clearly indicates that the implicit models should be reworked for large NPs on graphene, despite their correct behavior for graphite owing to the interlayer repulsion. One straightforward correction specific to graphene could be to have the implicit model only act beyond the simulation box (*i.e.* to account for the non-primitive cells only), and keep an explicit description within the primitive cell, which incidentally would not cause a large computational overhead since the relevant distances are needed for the covalent/metallic contributions anyway.

For graphite, good agreement between Figs. 3.4(b) and 3.4(c) is reached independently of adsorbate size, indicating that the approximations underlying the implicit model are well fulfilled. In particular, the substrate corrugation due to the interaction with the deposited NP remains moderate enough for the assumption of a planar upper layer to remain valid. For the adsorption on graphene the agreement between the implicit and the Grimme D2 dispersion model is not as good due to high corrugation. As will be seen below from our dynamical simulations, significant structural rearrangements take place already in small adsorbates, and it is rather unclear as to what the optimal shape of the particles should be in such large NPs deposited on nonrigid substrates.

### 3.3.4 Comparison with DFT calculations

The predictions of the present semiempirical models can be compared against available electronic structure reference data obtained at the level of DFT. Ramos-Sanchez and Balbuena [39] investigated the interaction of a Pt adatom and small Pt adsorbates deposited on various sites of graphite by means of dispersion-corrected DFT employing the projector augmented wave (PAW) pseudopotentials and treating the electron-exchange correlation within the spin polarized GGA and the Perdew-Becke-Ernzerhoff (PBE) and the Revised Perdew-Becke-Ernzerhoff functionals. The adsorption energy for the adatom found by these authors amounts to  $-2.18$  eV at the bridge site with a shortest Pt-C bond of 2.03 Å, both quantities being in satisfactory agreement with the present calculations where values of  $-2.74$  eV (implicit model) and  $-2.75$  eV

(Grimme D2) are respectively obtained at a common closest Pt-C distance of 2.06 Å.

In the case of graphene, several other DFT data without dispersion corrections have been reported for the adatom, but the values are significantly spread out. The adsorption energies for a Pt adatom at the most stable bridge position thus range from  $-0.37$  [146] to  $-1.5$  [147],  $-1.57$  [148],  $-2.03$  [149],  $-2.17$  eV [150] and  $-3.2$  eV [151], with equilibrium distances that always exceed the values obtained with dispersion corrections, although the variations among the different authors are much smaller (2.148, 2.101, 2.10, 2.12, 2.08, and 2.15 Å, respectively).

Results for the icosahedral Pt<sub>13</sub> adsorbate are much more scarce, however Ramos-Sanchez and Balbuena [39] reported an adsorption energy (total, not per contact facet atom as in Fig. 3.4) of  $-6.97$  eV at the bridge site, which is noticeably larger than the values obtained here of  $-4.27$  eV and  $-3.40$  eV in the explicit and implicit dispersion models. Using a finite cluster model of the graphene substrate, Okamoto [152] computed an adsorption energy of  $-1.08$  and  $-2.08$  eV at two other adsorption sites, but with the same orientation of Pt<sub>13</sub> on a graphene sheet. Additional DFT results are available in the case of Pt adatoms on defective graphene [148, 153]. Our values for the adsorption of a Pt adatom on a vacancy in graphite reported in Table 3.1 are comparable to the adsorption energy of a Pt atom on a vacancy in graphene of  $-7.45$  eV at a Pt-C distance of 1.94 Å calculated at the DFT level without dispersion correction by Fampiou and coworkers [148]. These authors further reported an adsorption energy of  $-6.68$  eV obtained with the Albe potential at 1.98 Å Pt-C separation, which is in good agreement with our own values for graphite. Repeating the calculations for defective graphene yields an adsorption energy of  $-7.37$  eV at 1.98 Å separation. The difference with the aforementioned semiempirical energy of Fampiou *et al.* thus quantifies the additional dispersion interaction beyond the simulation cell.

Additional adsorption energies for larger Pt adsorbates containing up to 27 atoms have been reported by Qi *et al.* from DFT calculations without dispersion corrections [153]. Unfortunately, comparison with those results is not straightforward because the structures considered by those authors differ significantly from ours.

### 3.3.5 Finite temperature dynamics of adsorbates on graphite

#### Thermal stability of Pt adsorbates on graphite

One essential advantage of analytical potentials over methods based on an explicit description of electronic structure is their ability to address physical properties on much stronger statistical grounds. Here we discuss the thermal stability of two-layered Pt<sub>64</sub> NPs on graphitic substrates, using MD trajectories spanning the nanosecond regime. The two Lindemann indices introduced in chapter 2 were used to monitor the dynamical evolution of the adsorbates as a function of increasing temperature, where index  $\delta_{\text{intra}}$  monitors the internal rigidity of the adsorbates and  $\delta_{\text{inter}}$  the global mobility of the adsorbate relative to its substrate.

Figure 3.5(a,b) shows the variations of these order parameters with increasing temperature for the example of the Pt<sub>64</sub> adsorbate assumed to initially occupy a bilayer shape in near epitaxy with the graphite substrate at low temperature. The simulations were performed using the explicit (D2) and implicit models of dispersion corrections. Simulations neglecting dispersion corrections altogether were also performed, but produced unphysical results with the spontaneous desorption of the adsorbate already below room temperature. This behavior was actually anticipated as it is consistent with the vanishing adsorption energy of clusters larger than 13 atoms unless dispersion forces are accounted for [see Fig. 3.4(a)]. For both dispersive correction models, the adsorbed NPs undergo increasingly large vibrations as temperature is increased, and a progressive but clearly visible transition to a more disordered state with

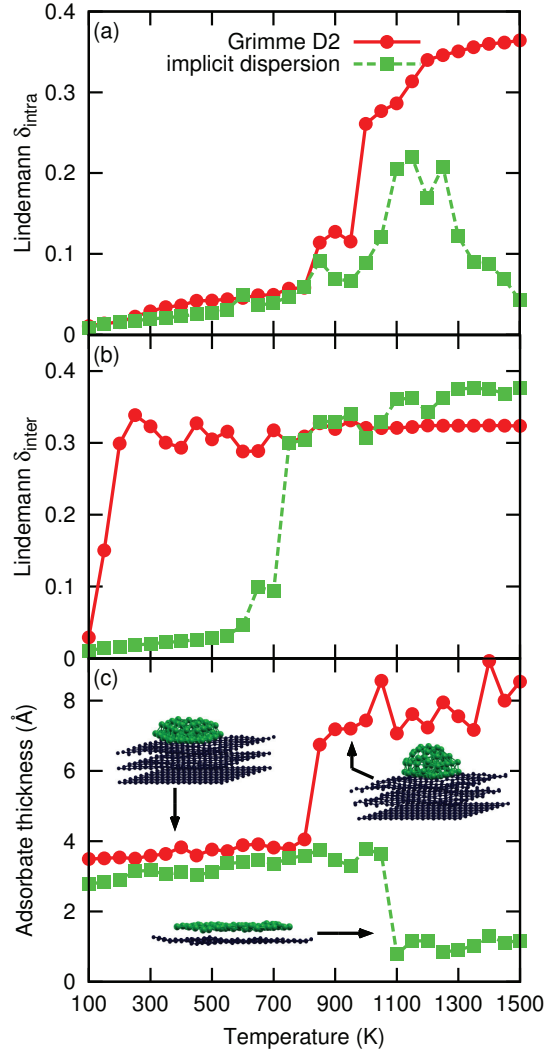


Figure 3.5: Temperature variations of the Lindemann indices measuring the internal rigidity of the  $\text{Pt}_{64}$  adsorbate ( $\delta_{\text{intra}}$ ) and the mobility of the adsorbate at the graphite surface ( $\delta_{\text{inter}}$ ), and average adsorbate height  $\sigma$  as obtained from the explicit (Grimme D2) and implicit dispersion models.

$\delta_{\text{intra}} > 0.15$  near 1000-1200 K. However, the other index  $\delta_{\text{inter}}$  reveals that the dynamics of the adsorbate on the substrate depends very sensitively on the model. In the explicit D2 description the NP moves relative to the substrate already above 200 K, whereas 750 K are necessary for such a motion to take place in the implicit model. These qualitative differences are quite significant, and reveal some contrasted energetic behaviors between the two approaches. We have examined the structural evolution of the adsorbate by calculating its geometric extension (or thickness)  $\sigma$  perpendicular to the substrate. Starting from a bilayer particle with  $\sigma \approx 2.7$ – $4.1$  Å, the variations of  $\langle\sigma\rangle(T)$  with temperature are shown in Fig. 3.5(c).

The different thermodynamical behaviors can now be related to different variations in the shape of the adsorbate, which becomes more spherical in the explicit D2 description ( $\langle\sigma\rangle \sim 8$  Å), but conversely much flatter ( $\langle\sigma\rangle \sim 1$  Å) if the dispersion correction is coarse-grained in the implicit model. The structural transitions here simply originate from the lower energy of those structures in their respective models, and the different temperatures of their onsets found in the

variations of  $\langle\sigma\rangle(T)$  roughly match the regions where  $\delta_{\text{intra}}$  increases in Fig. 3.5(a), albeit more smoothly due to the more regular one-layer structure of the adsorbate. Local minimization of the high-temperature structures confirms that the ellipsoidal isomer is much more stable in the explicit D2 model, by 5.6 eV, the flat isomer conversely lying 14.5 eV below the initial structure in the implicit dispersion model. These results motivate more systematic work on global optimization, which would shed more light onto the wetting behavior of the different dispersion models but lie beyond the present effort.

Although the present trajectories were carried out of equilibrium from a metastable state, they were able to locate low-energy minima shedding light onto different binding properties of the present dispersion models. The greater extent of wetting obtained with the implicit model thus reflects a stronger London interaction that is even comparable in magnitude to the metallic contribution holding the adsorbate together. From the purely energetic perspective, the dispersion corrections in the implicit model were expected to be stronger, simply because the explicit approach neglects the contributions from the semi-infinite substrate beyond the atoms from the simulation cell. What Fig. 3.5(b) further shows is that this stronger pinning of the adsorbate to the substrate also has dynamical consequences, the ability to diffuse being significantly suppressed. That the most stable structures of Pt adsorbates are so significantly affected by the nature and magnitude of dispersion interactions was itself not so obvious *a priori*, and constitutes one major finding of the present work that confirms the importance of those “corrections” on the global potential energy surface.

### Diffusion mechanism of adsorbates on graphite

The imperfect nature of the epitaxial contact between the metal adsorbate and the substrate causes some jiggling motion that was further investigated in details by following not only the center of mass, but also the global orientation of the adsorbate relative to the substrate. More precisely, we evaluated the angle  $\theta$  between the planar, horizontal projection of the bonds within the substrate and those at the contact facet of the adsorbate, defined by symmetry in the reduced range  $0 \leq \theta \leq 30^\circ$ , as a measure of alignment between the two lattices. A value  $\theta = 0$  corresponds to perfect epitaxial alignment, whereas maximal orientational mismatch is attained for  $\theta = 30^\circ$ . In the MD simulations, snapshots were taken every picosecond and the time series  $\theta(t)$  was analyzed.

At low temperature, the particle is stable on the substrate and vibrates. At sufficiently high temperature the diffusion motion starts to take place through some occasional jumps and jiggling. Fig. 3.6 illustrates the origin of this jiggling motion on a typical time series  $\theta(t)$  obtained for a trajectory at 900 K, together with the corresponding effective velocity of the center of mass of the adsorbate. The simulations were performed here with the implicit dispersion model. At this reasonably high temperature, most of the time is spent in good alignment between the adsorbate and the substrate, but misalignment occurs on short time scales and in correlation with sudden increases in the velocity modulus. Crossing these energy barriers gives the adsorbate enough velocity to travel rather long distances, the diffusion process showing properties similar to those of a (truncated) Lévy flight [154] with long residences between shorter jumps. Such processes have already been identified for NP diffusion on surfaces [42, 155, 156]. Fig. 3.7 illustrates this feature, showing the distribution of displacements of the center of mass of the adsorbate computed in time windows of 10 ps. In most time windows the adsorbate diffuses only little, while much larger displacements occur on rare occasions.

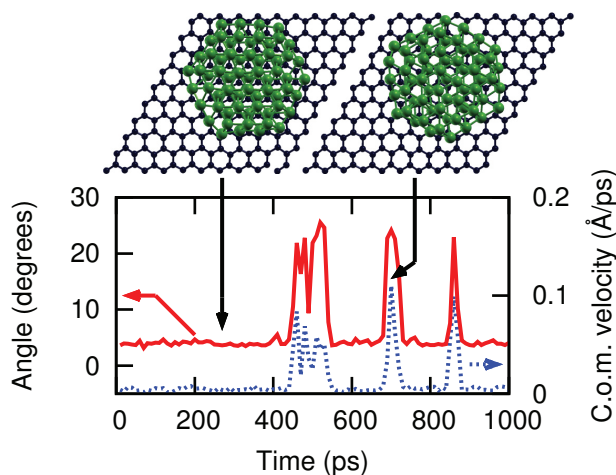


Figure 3.6: Short-time average angle between the  $\text{Pt}_{64}$  adsorbate and substrate lattices, and center of mass velocity of the adsorbate, as obtained from a MD trajectory at 900 K using the implicit model for dispersion corrections. Adsorbates under maximal (left) and minimal (right) alignment are also depicted.

### Surface diffusion constants and activation energy

The diffusion process has been further quantified by calculating the surface diffusion coefficient by linear regression of the long time regime of the MSD of the center of mass. Such diffusion coefficients are represented in Fig. 3.8 as a function of inverse temperature, as obtained from simulations with the Grimme D2 and the implicit dispersion correction. The alignment of the data points indicates that the diffusion follows Arrhenius behavior of eq. (2.65). As already pointed out, diffusion is reduced when the infinite extension of the substrate is taken into account via the implicit dispersion model. In the Arrhenius plot this has two consequences: the diffusion coefficients as obtained with the implicit dispersion model are lower and they increase faster with temperature relative to the calculations using the Grimme D2 dispersion. According to the Arrhenius law, this indicates higher activation energies for the diffusion process. As a side note, the data for the calculations with the implicit dispersion model are more dispersed. This is due to the lower values of the diffusion constant, which leads to higher relative uncertainties, but more importantly to the weaker convergence of the MSD due to the Lévy-type diffusion process as discussed previously.

MD simulations have also been carried out for smaller two layer adsorbates such as  $\text{Pt}_{19}$ ,  $\text{Pt}_{31}$  and  $\text{Pt}_{46}$ . As in the case of  $\text{Pt}_{64}$ , Arrhenius plots again give access to the activation energy of surface diffusion. These activation energies are shown as a function of adsorbate size in Fig. 3.9. The activation energy increases significantly with cluster size as the contact area with the graphite surface is also increased. This effect is less pronounced for larger adsorbates in the case of Grimme D2 dispersion, since in these cases a structural reorganization into a more ellipsoidal adsorbate shape may occur which reduces the contact with the substrate. The error bars indicate the quality of the linear regression carried out in the Arrhenius plots. As was the case for  $\text{Pt}_{64}$ , the stick-slip Lévy type diffusion induces greater uncertainty into the determination of the diffusion coefficients in the simulation using the implicit dispersion model.

Defects on surfaces can significantly alter the diffusion properties of adsorbates [157]. The influence of the vacancy and Stone-Wales defects in the uppermost graphitic layer on the diffusion propensity of  $\text{Pt}_{64}$  adsorbates was also addressed by MD simulations, using the implicit dispersion correction model. The results (not shown) indicate only a modest slowing down in

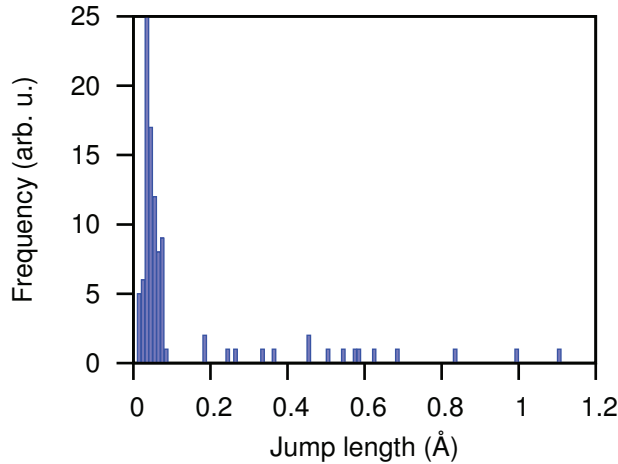


Figure 3.7: Occurrence of jumps of the center of mass of the  $\text{Pt}_{64}$  adsorbate in windows of 10 ps, as obtained from MD trajectories at 900 K using the implicit model for dispersion corrections. Most displacements of the adsorbate in this time window are well below 100 Å, while some are much larger.

the dynamics that amounts to a few percents reduction in the diffusion constant.

### Vibrational spectra

In addition to the long-time diffusion dynamics, the MD simulations provide a wealth of information about the vibrational dynamics occurring on shorter time scales. The vibrational spectrum was calculated from the Fourier transform of the velocity time autocorrelation function accumulated over windows of 4 ps at intervals of 1 fs from 1 ns long trajectories, which sets the spectral resolution to  $10 \text{ cm}^{-1}$  and a maximum detectable frequency of  $15 \cdot 10^3 \text{ cm}^{-1}$ . While the formula for  $C_{vv}(t)$  involves a further average over all atoms, the specific contributions of the adsorbate and substrate can also be evaluated separately.

The harmonic spectrum obtained from the dynamical matrix is expected to resemble the vibrational spectrum determined from the MD simulations only at low temperature, hence the comparison between the two types of calculations provides direct insight into anharmonicities and their manifestations at finite temperature in terms of band shifting and broadening.

The implicit dispersion model was again used for those static and dynamical calculations, the simulations at finite temperature being performed at 300 and 1000 K. Fig. 3.10(a) shows the vibrational spectra of the free graphitic surface and the free two-layered  $\text{Pt}_{64}$  at these temperatures as well as the normal mode frequencies of these two systems. All spectra exhibit similar features, with intense lines corresponding to grouped modes at low frequencies and reaching about  $1700 \text{ cm}^{-1}$ . The far-infrared range corresponds to the frequencies of the metal adsorbate, which fall into a rather continuous range below  $350 \text{ cm}^{-1}$ . For the adsorbate itself, deposition on graphite does not alter the vibrational properties very markedly. In contrast, the graphite substrate undergoes a more significant perturbation due to the adsorbate with clear band broadening and even merging of many small peaks up to  $700 \text{ cm}^{-1}$ . As expected, the spectral features corresponding to stretching C-C modes at higher frequencies are less affected. The perturbation exerted by the adsorbate on the vibrations of the graphitic layers appears more clearly at finite temperature, and we speculate that the extended range of these perturbations results from hot and combination bands.

Anharmonicities are also evidenced on the highest frequency band near  $1600 \text{ cm}^{-1}$ , which

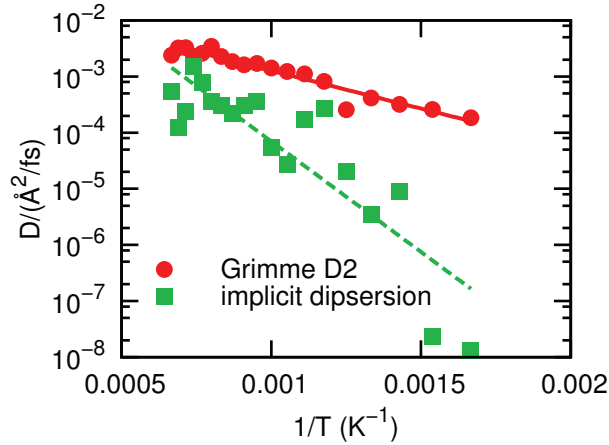


Figure 3.8: Surface diffusion coefficients of  $\text{Pt}_{64}$  and on graphite shown as an Arrhenius plot. The simulation data were obtained from MD trajectories at temperatures covering the range 500–1500 K using the Grimme D2 dispersion model and the implicit model for dispersion corrections, and linear interpolations are also shown.

displays some slight broadening but more importantly some red shifting as temperature varies from 0 to 300 K and finally 1000 K. This peak, which dominates the G band of graphite, has been further quantified below in the case of epitaxial graphene on fcc platinum.

### 3.4 NPs on epitaxial graphene on Pt(111)

The implicit dispersion correction model has been extended to describe epitaxial graphene on Pt(111) and Pt adsorbates on such substrates. Epitaxial graphene [32] on platinum has been experimentally studied by AFM [158] and by STM [159, 160] possibly coupled to other techniques such as local tunneling barrier height [161] or LEED [125, 162]. Though usually synthesised by CVD, epitaxial graphene on Pt(111) has also been produced by colliding carbonated molecules such as methane [163] or  $\text{C}_{60}$  [126], by subsurface segregation [164] and by liquid phase deposition [165].

#### 3.4.1 Modeling of supported graphene

##### Geometric properties of the moiré

The lattice constant of graphene is about 1/8 smaller than the equilateral triangular surface lattice of Pt(111) and therefore a moiré pattern can be produced if the two lattices are superimposed under the commensurate 9/8 size ratio. In comparison to other transition metals such as nickel, graphene interacts with platinum rather weakly, which further allows additional moiré patterns with different periodicities to be formed by varying the inplane angle  $\Theta$  between the two lattices [32].

Fig. 3.11 depicts the geometry of a typical moiré structure formed by epitaxial graphene and the relevant adsorption sites resulting from these two commensurate lattices in contact with each other. In addition to the aforementioned alpha, bridge, and hollow adsorption sites on bare graphene, there are several regions of alignment or misalignment between the two lattices. In the fcc region, the carbon atoms are on top of Pt atoms of either the first or second Pt layer. In the top region, the center of the 6-membered carbon rings is on top of the Pt atoms of the

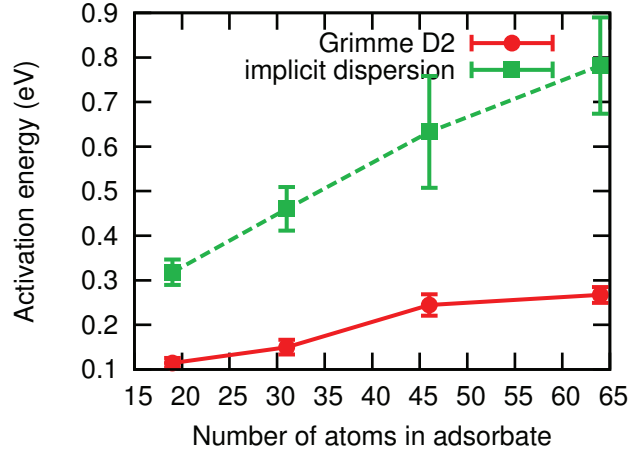


Figure 3.9: Activation energy for surface diffusion of bilayer Pt adsorbates as a function of their size in simulations using the Grimme D2 dispersion model and the implicit model for dispersion.

uppermost layer. Finally, the hcp region has those rings aligned with the atoms of the second Pt layer.

Using the dedicated procedure presented in chapter 2, possible moiré structures up to a certain predefined size can be listed. The edge length of the supercell obtained by this purely geometric procedure is illustrated in Fig. 3.12. The general decrease in the edge length of the moiré supercell with increasing  $\Theta$  is equivalent to an increase in periodicity (full circles in Fig. 3.12), except at low angles where the monotonic relation does not hold and where the periodicity is better represented by an approximate half value (empty circles in Fig. 3.12). The minor deviations from monotonic behavior arise from the slight adjustment made to graphene to match the common cell size.

A similar numerical approach for the determination of moirés was followed earlier by Merino and coworkers [126]. The names assigned by these authors to some specific structures are detailed in Table 3.4.1 and are also indicated in Fig. 3.12. Near the angle of  $1.71^\circ$  a structure very similar to the  $\lambda$  moiré reported by Merino *et al.* was found but with twice the size of the super cell. This structure is denoted as " $\lambda$ " in Table 3.4.1.

### Moiré structures and screening of dispersion

Using the present potentials, the moiré structures were locally optimized in order to determine the magnitude of corrugation  $\Delta z$  of the graphene layer and its separation with the metal. The adsorption energies averaged over all moiré structures and obtained with the Grimme D2 model (334 meV/carbon atom) or the implicit dispersion model (355 meV/carbon atom) are very similar to each other but significantly overestimate the recent predictions of 43 meV/carbon atom by Vanin and coworkers [167] based on vdW-DF calculations, which satisfactorily agree with earlier computations by Khomyakov and coworkers (38 meV/carbon atom for the  $\alpha$  moiré [166]) and by Gao *et al.* (38.6 and 39.8 meV/carbon atom for the  $\xi$  and  $\alpha$  moirés, respectively [125]).

The overestimation with the present models is due to the absence of screening in both explicit and implicit dispersion models, which is important owing to the delocalized nature of the electron cloud in the bulk metal. One empirical way of accounting for these screening effects consists of considering the contributions to the London interactions of the uppermost

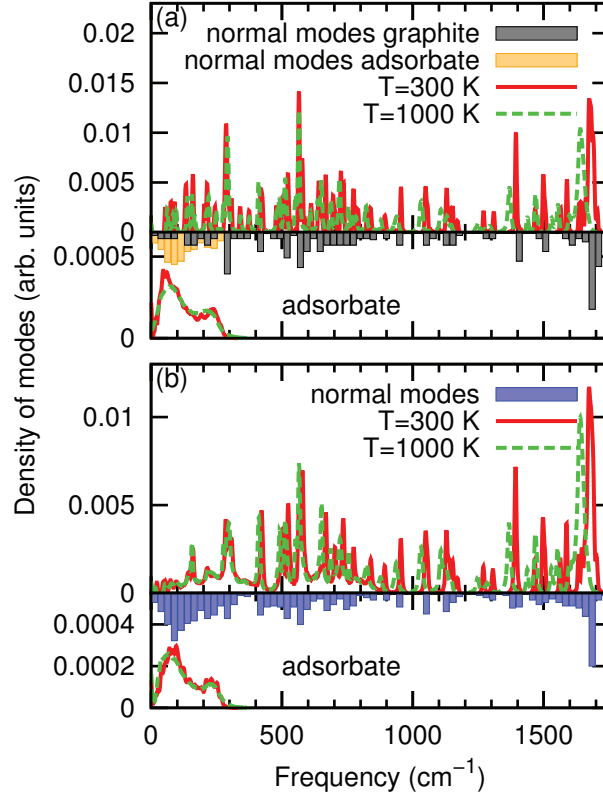


Figure 3.10: Vibrational spectra for a two-layer  $\text{Pt}_{64}$  adsorbate on graphite obtained from the velocity time correlation function at finite temperatures (continuous lines) and in the harmonic limit (histograms pointing downward). (a) Spectra of isolated substrate (upper part) and adsorbate (lower part); (b) Global spectra of the entire system (upper part) and of adsorbate alone (lower part) but interacting with the substrate. The calculations were performed with the implicit dispersion correction model.

layer only [61, 168]. Repeating the calculations under such conditions leads to a significantly reduced adsorption energy of 273 meV/carbon atom, still off by a factor 6 with respect to the reference data of Vanin *et al.* [167], the uppermost metal layer alone contributing to about 77% of the total dispersion energy.

Alternatively, introducing a TF screening factor as in Eq. (2.46) can achieve a similar effect, but to an even greater extent. Fig. 3.13(a) shows the variations of the adsorption energy of the graphene layer in epitaxial contact with Pt(111), as a function of the screening length  $r_{\text{TF}}$  and for three different inplane angles  $\Theta$  corresponding to the structures denoted as  $\xi$ ,  $\gamma$  and  $\beta$  in Table 3.4.1. The damping of the global London attraction is particularly prominent, and the vdW-DF reference value of 43 meV/carbon atom is recovered approximately for  $r_{\text{TF}} = 2.9 \text{ \AA}$ . The adsorption of epitaxial graphene is also found not to depend significantly on the type of moiré pattern, which is also true for the other dispersion models considered in this work (results not shown).

The natural corrugation of the graphene layer was evaluated from the locally relaxed structures and as a function of the screening length  $r_{\text{TF}}$ . Its variations, shown in Fig. 3.13(b), are found to be correlated to those of the magnitude of the adsorption energy, which is the expected behavior since stronger binding also tends to increase the natural corrugation due to incommensurability, and also corrugate the carbon monolayer.

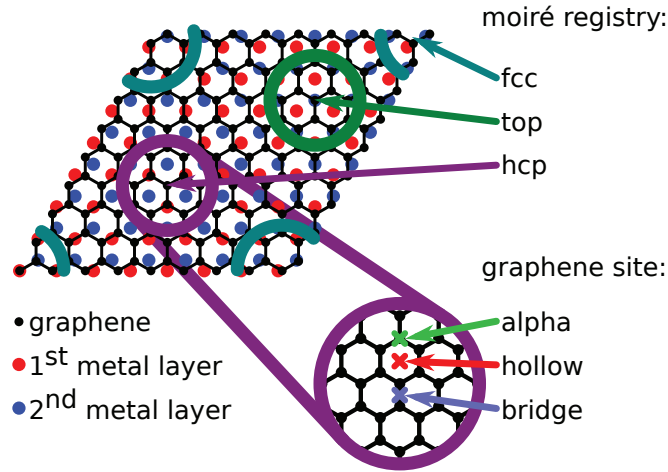


Figure 3.11: Inventory of moiré sites of the graphene/Pt(111) system with a vanishing inplane angle ( $\xi$  structure).

The interplay between corrugation and the strain exerted by the two materials in contact was further investigated by considering not only the magnitude  $\Delta z$  of the graphene corrugation, but also the average separation  $\delta z$  between the carbon sheet and the uppermost metal layer. Those properties were evaluated at 0 K from local minimizations of structures that were obtained via MD simulations at 300 K. The variations of these geometric properties with increasing inplane angle are represented in Fig. 3.14. As a general trend, corrugation decreases with increasing inplane angle, which can be understood from the natural increase of the moiré periodicity with the inplane angle. The average distance  $\delta z$  is fairly independent of the inplane angle and lies near the 2.8 Å cut-off of the covalent part of the BOP. Dispersion interactions affect the corrugation magnitude in a rather similar way as the adsorption energies in Fig. 3.13, where stronger dispersion lead to larger corrugations. However, this relation may be reversed when the graphene layer experiences comparably high compressive strain, which is the case for the  $\delta$  structure at  $\Theta = 10.9^\circ$ , and especially in the  $\xi$  moiré at  $\Theta = 30^\circ$  where the unscreened models yields extreme values for the corrugation ( $\Delta z = 2.7$  Å) and separation ( $\delta z = 3.5$  Å) due to excessive lateral compression that cannot be compensated by the attraction to the metal. Limiting the dispersion forces from the uppermost metal layer attenuates this problem but does not solve it entirely. This effect is essentially geometric and arises due to slight squeezing or stretching of the graphene sheet necessary for matching the moiré within a common periodic simulation box also for the other moiré structures. Although we took care to perform all simulations with sufficiently large system sizes, size effects could still affect the corrugation of the graphene when it is highly subjected to compressive strain. Since graphene is a highly stiff material [169], minor adjustments in the geometry produce relatively large effects especially when dispersion forces are weak or absent, as precisely occurs for the unscreened or top layer dispersion models.

### Effect of temperature on graphene/Pt(111)

Thermal effects were investigated for two specific moiré structures, namely the  $\xi$  and  $\gamma$  patterns at  $\Theta = 0$  and  $13.9^\circ$ , respectively. MD simulations were carried out at increasing temperatures, and the average magnitude of the corrugation and graphene-metal separation were both evaluated. They are reported in Fig. 3.15 for the four dispersion models. Once thermal effects are taken into account, the vibrational fluctuations make the graphene layer slightly shift away from the metal substrate for all models. According to Fig. 3.15 this shift amounts to approxi-

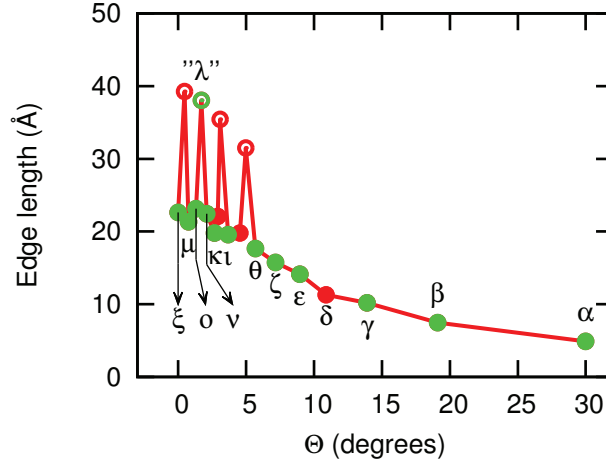


Figure 3.12: Edge length of moiré structures obtained for graphene on Pt(111) by varying the inplane angle between the two lattices obtained by geometric construction (red circles) and observed in experiments (green circles, see also Table 3.4.1 for the assignment of the different structures). Full and empty circles refer to simple commensurate lattices and to commensurate lattices of twice the size of the apparent moiré periodicity, respectively.

mately  $0.1\text{--}0.3\cdot 10^{-3} \text{ \AA K}^{-1}$ . Thermal fluctuations also tend to increase the corrugation by about  $0.3\text{--}1.4\cdot 10^{-3} \text{ \AA K}^{-1}$  depending on the model. The four descriptions of dispersion forces agree well with each other for the  $\xi$  moiré, but differ more sensitively for the other  $\gamma$  structure, the top layer dispersion model predicting some early increasing in both geometric properties but also some saturation already near room temperature.

For both values of the inplane angles, the graphene layer experiences no compressive strain, and thermal effects are rather similar. Notable differences are found in moirés characterized by high compressive strain such as the  $\delta$  or  $\alpha$  structures, with stronger slopes and greater variations among models (data not shown). It should also be kept in mind that the simulation results presented in Fig. 3.15 were obtained at constant density. However, the two materials in contact have different TECs and in practice simulations at finite pressure would be more appropriate. However, even then it would be rather difficult to find a common box size that is suitable for both materials, especially when their TECs differ. While those refinements lie beyond the scope of this work, our results indicate how structural properties as basic as corrugation amplitude or interlayer separation are sensitive to the details of the interactions for such complex materials.

Some comparison between the present results and available experimental measurements and electronic structure calculations can also be attempted. Corrugation of epitaxial graphene accessed through STM height profiles have been reported to lie in the  $0.3\text{--}0.8 \text{ \AA}$  range [125]. Those values are in good agreement with our calculations at 300 K. Similar measurements carried by Land and coworkers [159] specifically for the  $\xi$  structure have found that corrugation amounts to  $0.8 \text{ \AA}$ , however the authors indicate that part of this corrugation could be due to the tunneling current. In their DFT study of the  $\xi$  structure at 0 K (without dispersion corrections), Gao and coworkers [125] reported a buckling magnitude of  $0.53 \text{ \AA}$ , which agrees with our calculation only in the extreme case of unscreened dispersion.

The graphene-metal separation has been experimentally measured by Sutter *et al.* [164] using LEED who found a value of about  $3.3 \text{ \AA}$ . Similar values of  $3.3 \text{ \AA}$  [166] and  $3.1 \text{ \AA}$  [125] have been obtained in DFT calculations at 0 K and neglecting dispersion corrections, and surprisingly in their dispersion corrected DFT calculation Vanin and coworkers reported a significantly higher separation of  $3.67 \text{ \AA}$  [167], all these values again for the  $\xi$  moiré structure. Those values

Moiré in Wood's notation	$\Theta(^{\circ})$	Name [126]	References
$(9 \times 9)$ R0.00°	0.00	$\xi$	[125, 126, 159, 165]
$(\sqrt{244} \times \sqrt{244})$ R26.33°	0.46		
$(\sqrt{73} \times \sqrt{73})$ R5.82°	0.77	$\mu$	[126, 158]
$(\sqrt{84} \times \sqrt{84})$ R10.89°	1.32	$\omicron$	[126]
$(\sqrt{229} \times \sqrt{229})$ R16.63°	1.71	" $\lambda$ "	
$(\sqrt{79} \times \sqrt{79})$ R17.00°	2.11	$\nu$	[126]
$(\sqrt{63} \times \sqrt{63})$ R19.11°	2.68	$\kappa$	[126, 158]
$(\sqrt{76} \times \sqrt{76})$ R23.41°	2.92		
$(\sqrt{199} \times \sqrt{199})$ R7.05°	3.09		
$(\sqrt{61} \times \sqrt{61})$ R26.33°	3.67	$\iota$	[126, 158, 161]
$(\sqrt{61} \times \sqrt{61})$ R26.33°	4.54		
$(\sqrt{157} \times \sqrt{157})$ R3.96°	4.99		
$(7 \times 7)$ R21.79°	5.69	$\theta$	[126]
$(\sqrt{39} \times \sqrt{39})$ R16.10°	7.15	$\zeta$	[126]
$(\sqrt{31} \times \sqrt{31})$ R8.95°	8.95	$\varepsilon$	[126, 158]
$(\sqrt{21} \times \sqrt{21})$ R10.89°	10.89	$\delta$	[126]
$(4 \times 4)$ R0.00°	13.90	$\gamma$	[125, 126]
$(3 \times 3)$ R0.00°	19.11	$\beta$	[125, 126, 158, 160, 162–164]
$(2 \times 2)$ R0.00°	30.00	$\alpha$	[125, 126, 159, 166]

Table 3.2: Moiré patterns obtained from geometric considerations, referred to using Wood's notation for the geometry with respect to graphene and ordered with increasing inplane angle  $\Theta$ . When applicable, the name assigned to the structure by Merino and coworkers [126] is also reported. References where the corresponding structures have been studied for graphene on Pt(111) are given in the last column.

are thus slightly higher than those obtained in the present model calculations, even at finite temperature, but it is clear that separations much larger than the 2.8 Å cut-off of the covalent potential cannot be reached since the dispersion interaction is purely attractive.

### Vibrational properties of epitaxial graphene on Pt(111)

The vibrational properties of epitaxial graphene can be straightforwardly evaluated from MD simulations, allowing to demonstrate the potential of the present models to fully capture anharmonic properties as a function of temperature. The implicit dispersion model with screening length  $r_{\text{TF}} = 2.9$  Å was employed for moiré structures of the  $\xi$  and  $\gamma$  types, and for comparison additional simulations were performed for freestanding graphene. From the 1 ns long MD trajectories, the vibrational spectra were again obtained by Fourier transformation of the velocity time autocorrelation function. Similar to Fig. 3.10 one peak dominates the spectrum near 1600  $\text{cm}^{-1}$ , which we attribute to the G band in the Raman spectrum of graphite [170]. This attribution is supported by normal mode analyses performed for increasingly strained structures, as represented in Fig. 3.16. The corresponding frequency depends on strain linearly with a slope of about  $-70 \text{ cm}^{-1}$  per percent of strain. Very similar values of  $-63 \text{ cm}^{-1}/\%$  [171] and  $-70 \pm 3 \text{ cm}^{-1}/\%$  [172] have been reported at 300 K.

Having assigned the calculated peak to the Raman G band, we have evaluated its robustness against finite size effects by evaluating its variations with increasing size of the periodic cell in the simulation. Normal mode analysis indicates that convergence is reached already at  $3 \times 3$  unit cells, as expected for such strong inplane modes.

Because the moiré pattern depends sensitively on the lateral strain experienced by the epitaxial layer, it is expected that the vibrational signature of the G band should depend on

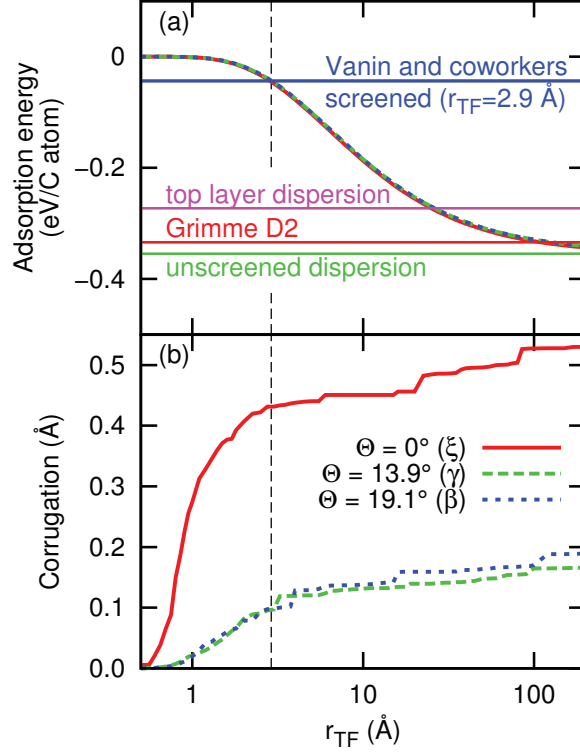


Figure 3.13: Variations of (a) adsorption energy and (b) corrugation of the graphene monolayer in epitaxial contact with Pt(111), as obtained from the implicit dispersion model as a function of the screening length  $r_{TF}$ . The curves were obtained for various moiré structures corresponding to different inplane angles  $\Theta = 0^\circ$  ( $\xi$ ),  $13.9^\circ$  ( $\gamma$ ) and  $19.1^\circ$  ( $\beta$ ) and based on local relaxations. In panel (a) the adsorption energies predicted by other dispersion models are also indicated as horizontal lines.

the inplane angle. This speculation is confirmed from our numerical results, which have been represented in Fig. 3.17 as a function of temperature. For the three systems, the peak positions exhibit some nearly linear red shifting with increasing temperature, which is the behavior known for pure graphite [173–175]. For pristine graphene, the variations show a slope of approximately  $-0.050 \text{ cm}^{-1}\text{K}^{-1}$ , in good agreement with Raman spectroscopy measurements [176–178].

In the case of epitaxial graphene, the G peak is not much altered in the  $\xi$  moiré structure with no inplane angle, whereas the  $\gamma$  moiré exerts some rather high stretching strain leading to a significant redshift of about 80 wavenumbers already at low temperatures. As temperature is increased, the additional redshift caused by anharmonicities is again manifested by nearly linear variations and slopes in the range  $-0.039$ – $-0.028 \text{ cm}^{-1}\text{K}^{-1}$  for the  $\xi$  and  $\gamma$  moirés, respectively. These results obtained for the  $\xi$  moiré are in agreement with the only Raman measurements that we know of, namely by Kang and coworkers [160] who reported some blue shift of the G band of epitaxial graphene on platinum relative to bulk graphite due to compressive strain. In contrast to the  $\xi$  structure, which undergoes some compressive strain at finite temperature, strain in the  $\gamma$  moiré is of the stretching type. Its manifestation as a redshift in the vibrational spectrum is thus also consistent with the measurements by Kang *et al.* [160].

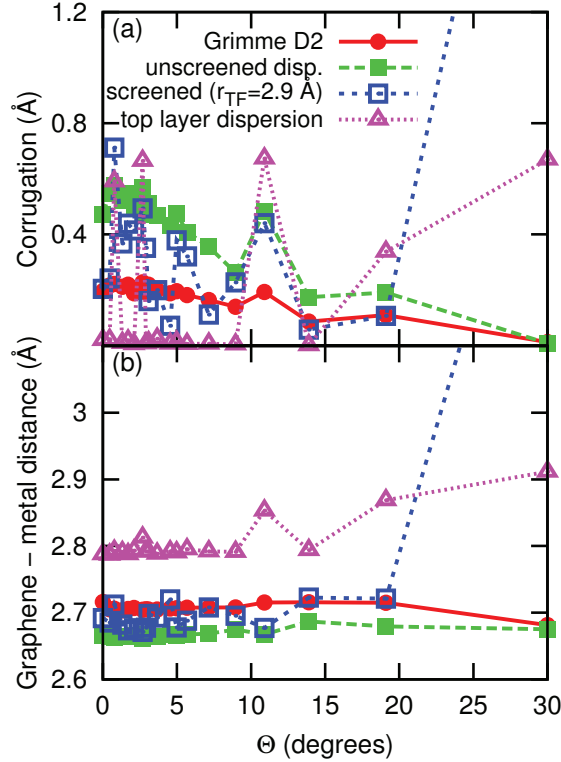


Figure 3.14: (a) Corrugation  $\Delta z$  and (b) interlayer separation  $\delta z$  of a graphene layer epitaxied on Pt(111) as a function of the inplane angle  $\Theta$ , as obtained from different dispersion models at  $T = 0$ . The values predicted by the model with screened dispersion forces lie beyond the respective upper values of the graphs at  $\Theta = 30^\circ$  (see text for discussion).

### 3.4.2 NPs on moiré substrates

The atomistic models developed so far are now applied to an even more complex situation of Pt adsorbates on epitaxial graphene on Pt(111). The two layer  $\text{Pt}_{64}$  adsorbate was deposited onto the  $\xi$  moiré structure initially at the fcc region and in the bridge epitaxial position and locally relaxed. We compare the predictions of the different dispersion correction models, namely the fully explicit (Grimme D2) approach and the implicit model without any screening or with  $r_{\text{TF}} = 2.9 \text{ \AA}$ . From the trajectories, the Lindemann indices of internal and adsorbate-substrate mobilities were calculated, as well as the adsorbate thickness used to monitor the possible structural transitions.

The variations of those indicators  $\delta_{\text{intra}}$ ,  $\delta_{\text{inter}}$  and  $\sigma$  with increasing temperature, as obtained with the three models, have been represented in Fig. 3.18(a-c). Interestingly, the fluxionality in the adsorbate as measured by  $\delta_{\text{intra}}$  shows similar variations among the three models, with a rather flat behavior until 1000 K where sudden jumps occur. The adsorbate-substrate mobility index,  $\delta_{\text{inter}}$ , is also similar between the explicit and unscreened implicit models, however adsorbate mobility is clearly found with the screened implicit model already above 550 K.

Inspection of the shape indicator  $\sigma$  reveals notable differences that are reminiscent of similar conclusions obtained in the case of the graphite substrate in Fig. 3.5, with a tendency of the explicit model to produce more spherical shapes, and conversely flatter shapes with the unscreened implicit model. At temperatures exceeding 1100 K, the adsorbate is highly disordered and no longer thermally stable. In addition, due to its low adsorption energy, the graphene

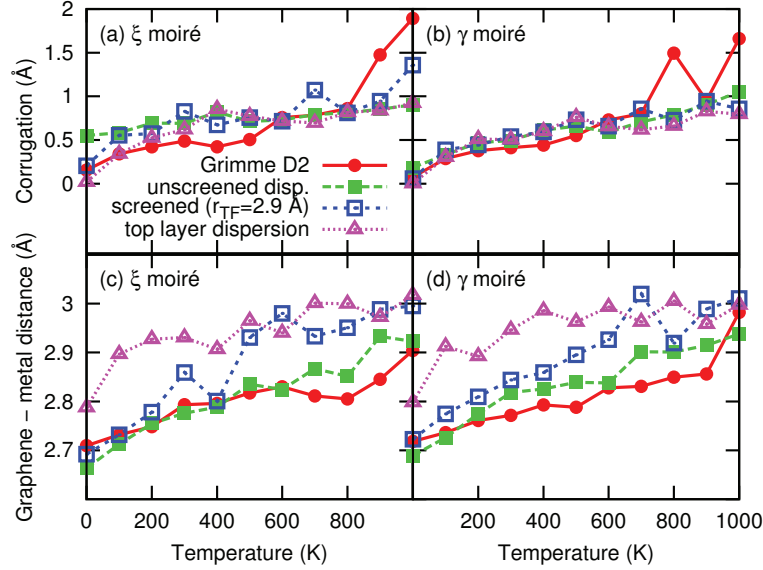


Figure 3.15: Thermally averaged corrugation  $\Delta z$  (upper panels) and graphene-metal separation  $\delta z$  (lower panels) of a graphene layer epitaxied on Pt(111) as a function of temperature, as obtained from different dispersion models for the  $\xi$  moiré (inplane angle  $\Theta = 0^\circ$ , left panels) and the  $\gamma$  moiré (inplane angle  $\Theta = 13.9^\circ$ , right panels).

sheet itself begins to thermally desorb above this temperature with the weakly binding screened dispersion model.

The diffusion dynamics can be probed from the MSD of the adsorbate more quantitatively than the index  $\delta_{\text{inter}}$ . Visual inspection indicates that even on this moiré substrate diffusion proceeds by a stick-slip mechanism with its Lévy flight properties. However, an additional mechanism is discernible in which the graphene layer slightly slides over the metal substrate (data not shown). This sliding process is found with all dispersion models, including the fully corrugated explicit treatment. Its contribution to the global diffusion is not obvious, nor its physical significance as such global motions could be markedly affected by size effects. In addition, the present approximation of a fixed density could also produce excessive strain in the substrate. Releasing this strain in constant-pressure simulations could well modify the diffusion behavior, although the problem of strain due to forcing the two subsystems in a common simulation box would remain.

## 3.5 Conclusions

In this chapter, we have extended the Brenner BOP by a dispersion correction for long-ranged forces. In a first approach this has been achieved by simply adding the Grimme D2 or D3 descriptions. Due to their long range these explicit descriptions of dispersion turned out to be computationally expensive in comparison to the BOP model for the covalent and metallic interactions. Therefore, in a second effort, we exploited the geometry of the system where an adsorbate is in contact with a layered substrate. Approximating the substrate layers by flat homogeneous atomic densities allows to integrate the contribution to the dispersion interaction of entire layers and summing up these contributions for a semi-infinite stack of substrate layers. This does not only significantly speed up the calculations, but more importantly this way the true semi-infinite nature of the substrate is included in the dispersion correction. However, it

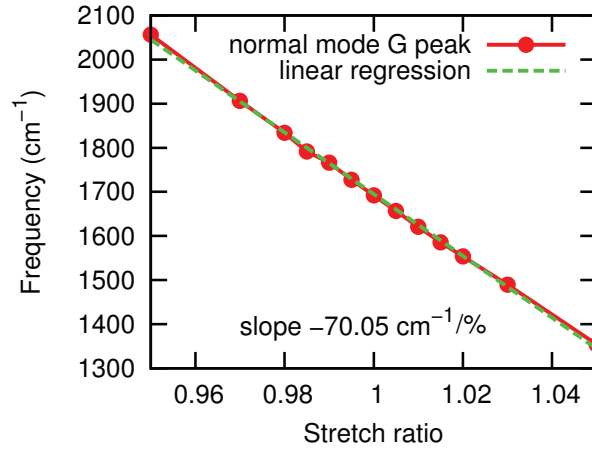


Figure 3.16: Position of G peak as a function of of the biaxial extension ratio as obtained from normal mode analysis of freestanding graphene.

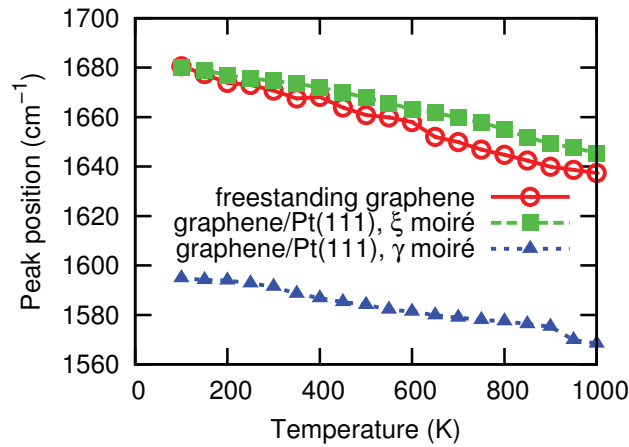


Figure 3.17: Position of the intense G peak as a function of temperature, as obtained from MD simulations of freestanding graphene and epitaxial graphene on Pt(111) forming  $\xi$  and  $\gamma$  moiré patterns. The simulations of epitaxial graphene used the implicit dispersion correction model with a screening length of  $r_{TF} = 2.9 \text{ \AA}$ .

turns out that in the case of the metallic substrates, the dispersion interaction may be screened rather efficiently by delocalized electrons. This problem could be addressed by the introduction of an additional empirical screening factor into the implicit model for dispersion.

These ideas have been tested on several systems of Pt adsorbates on carbonated substrates. From local structure optimizations, comparisons with existing dispersion corrected DFT calculations could be made, confirming the ability of the implicit dispersion correction model to reproduce reasonably well the structural and energetic properties of epitaxial graphene. Always comparing the different dispersion descriptions, MD simulations have been carried out, which showed clear differences in the thermal behavior between adsorbates on graphite and adsorbates deposited onto epitaxial graphene. On epitaxial graphene, adsorbate diffusion is very much suppressed, while on graphite particularly high diffusion rates could be identified. This could be explained by the strong dispersion interaction between the metal adsorbate and the metal part of the substrate that may pin the graphene layer firmly between the two Pt subsystems. Due to the reduced dispersion interaction of the adsorbate with graphite a such

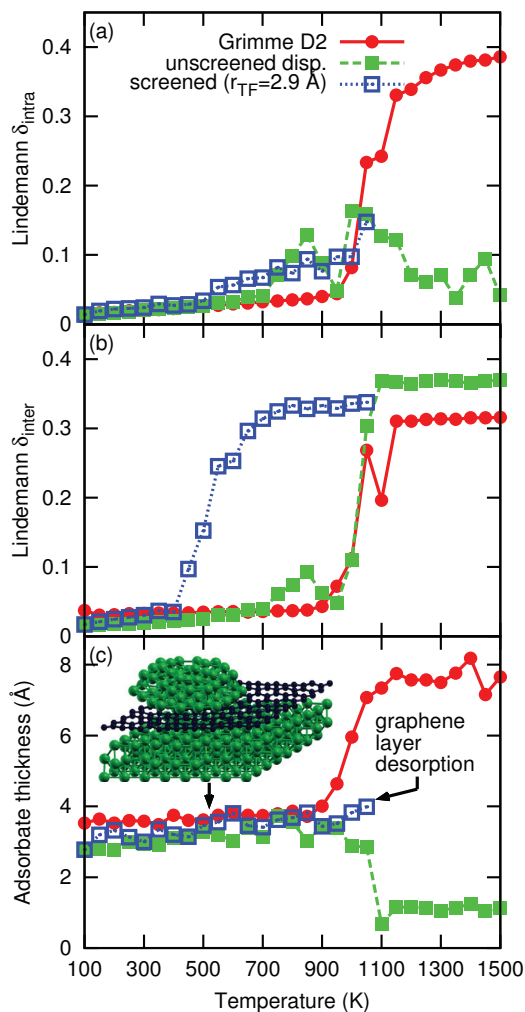


Figure 3.18: Lindemann indices of intra-adsorbate mobility and adsorbate-support and thickness of  $\text{Pt}_{64}$  on graphene/Pt(111) in the  $\xi$  moiré structure as a function of temperature for different dispersion correction models.

effect is not observed in this system.

Epitaxial graphene interacts rather weakly and mostly only by dispersion interactions with the Pt(111) surface. In contrast, the graphene/Ru(0001) system treated in the following chapter interacts strongly. Nonetheless dispersion interactions play also an important role in this system.

# Chapter 4

## The ruthenium-carbon system

In contrast with the Pt-C system, where different dispersion models could be evaluated on various static and dynamical properties, we focus here on the Ru-C system for which no BOP was available at the beginning of this thesis. Our model for the Ru-C system aims to describe epitaxial graphene on Ru(0001) and ruthenium NPs on such substrates or on graphite. The model has been parametrized on electronic structure calculations and improved to account for long-range London dispersion forces following an approach similar to the Grimme D2 correction scheme, as well as possible non-additive screening effects that are relevant for GOM. As will be shown below, the model correctly reproduces a variety of structural properties for different commensurate moiré structures as observed in experiments or predicted by DFT calculations. As achieved previously for Pt-C systems, the energetic and thermal stabilities of Ru NPs on graphite and epitaxial graphene have been addressed using local optimizations and MD simulations. While NPs exhibit relatively fast diffusion on the graphite substrate, the corrugation of epitaxial graphene is found to strongly stabilize them against internal rearrangement and global diffusion. The simulated vibrational spectra of epitaxial graphene show variations with moiré structure and temperature that provide insight into anharmonicities and emphasize the role of strain.

### 4.1 Introduction

Ruthenium is a transition metal to which epitaxial graphene binds rather strongly [179]. Experimentally, epitaxial graphene on Ru(0001) can be prepared by methane [180] or ethylene [181–190] decomposition, surface segregation [44, 184, 191–197], carbon vapor deposition [198] or by temperature programmed growth where hydrocarbon molecules are adsorbed at low temperature and subsequently annealed to higher temperatures [184]. Experimental characterization has been achieved most commonly using STM [180–182, 184, 186, 187, 189–192, 194, 195, 197], LEED [44, 181, 187, 188, 190, 191, 193, 194] and AES [44, 187, 191, 192, 194]. On the theoretical side, epitaxial graphene on Ru(0001) has been studied extensively by electronic structure calculations [199–203] but usually at zero temperature.

From the quoted studies, several periodicities of moiré structures appear to have been considered. The cases of 10 on 9 [44], 11 on 10 [67, 203–205], 12 on 11 [180, 188, 191, 194, 199, 203, 205, 206] and 13 on 12 moirés [188, 203, 206] are among the most documented. While these relatively small values of both  $x$  and  $y$  make them convenient for theoretical modeling, surface X-ray diffraction studies have confidently shown that experimental moirés of graphene on Ru(0001) are more likely of the 25 on 23 type [181, 185]. The 25 on 23 system is approximately four times as large as the aforementioned structures, and has also recently been

addressed by DFT calculations using the Gaussian and plane wave method (GPW) [203]. It contains four subsystems called moirons, each containing a topographic buckling or hill in the graphene layer. Detailed analysis shows that three of them are equivalent [203].

Graphene usually grows in alignment with the underlying Ru(0001) surface, however on polycrystalline Ru moiré finite inplane angles and a plethora of periodicities have been reported [46, 201, 207]. Further bilayer graphene may be grown on Ru(0001) [200, 208–211], also with different orientations or stacking order of the two layers [212].

Because of the rather large moiré structures, this system is challenging for *ab initio* calculations, especially at finite temperature where no predictions have been reported so far. In this chapter, we have constructed and parametrized a many-body potential to model epitaxial graphene on Ru(0001), allowing in turn large scale statistical simulations at finite temperature for this complex substrate, but also for deposited ruthenium NPs. Our potential combines the BOP for carbon developed by Brenner [101] with an EAM for ruthenium. Among the various existing EAMs for this metal [213–218] we have chosen the form and parameters by Li and coworkers [215–217] that can be rewritten under the BOP format [97], providing a uniform and simple expression for the general Ru-C potential, similar to previous efforts carried by Albe and coworkers for the Pt-C system [96]. In order not to degrade these original potentials for the pure elements, only the parameters corresponding to mixed Ru-C interactions were adjusted in order to reproduce available electronic structure data [201, 206] as best as possible.

Recent DFT calculations have additionally shown that London dispersion interactions could be a significant contribution to the binding of monolayer graphene on Ru(0001), owing to their long-range nature and to the semi-infinite extension of the two materials [67, 200, 202, 203]. We have thus completed our model for the Ru-C system by including dispersion corrections as well, following the simple pairwise model of Grimme and coworkers (D2 version) [76]. Non-additive screening effects due to delocalized electrons in the metal substrate [66] were included phenomenologically by considering the contribution from the first metal layer only [61, 168]. Besides the substrate itself, our model can be used straightforwardly to treat ruthenium NPs on carbonaceous substrates such as graphene, graphite, or epitaxial graphene. Ru NPs are interesting in their own and have been shown to have applications in catalysis for ammonia synthesis [219], hydrogen storage [136], and the oxidation of carbon monoxide [220] and a wide range of alcohols [221]. Their practical use requires formation (or deposition) on a substrate in a stable fashion, carbon providing a low-cost and versatile element for such supports [52, 221, 222].

In the following section we present the parametrization for the Ru-C system aimed toward epitaxial graphene. Section 4.4 discusses applications for Ru clusters deposited on graphite, for epitaxial graphene on Ru(0001) in bare form and acting as a substrate for Ru clusters as well. In addition to structural and energetic properties, the dynamical behavior at finite temperature has been investigated from MD simulations. In particular we report activation temperatures for Ru NPs diffusing on graphite as well as a vibrational analysis of anharmonic properties through the graphene Raman G band. Both properties, of experimental relevance, were obtained from long time scales trajectories that would not have been practical had the electronic structure of the system been described explicitly. Finally we conclude in section 4.5 by giving a brief summary of the main results from this chapter.

## 4.2 Bond-order potential for Ru-C

The original Brenner BOP naturally includes many-body contributions for metals in TB-SMA scheme [223], which have notably been parametrized for ruthenium [215–217]. The BOP framework was thus naturally chosen to model the system of interest here, namely epitaxial graphene

	Ru-Ru	Ru-C	C-C
$S$	19.039	40.089	1.22
$\beta$ ( $\text{\AA}^{-1}$ )	1.5444	1.2139	2.1
$D_0$ (eV)	3.8503	0.71573	6
$r_0$ ( $\text{\AA}$ )	2.5584	2.0833	1.39
$R^{(1)}$ ( $\text{\AA}$ )	4.0	2.71	1.7
$R^{(2)}$ ( $\text{\AA}$ )	4.3	3.01	2
	Ru-Ru-Ru	permutations of Ru-Ru-C and Ru-C-C	C-C-C
$\gamma$	1	0.0038154	0.00020813
$c$	0	244.84	330
$d$	1	9.3054	3.5
$2\mu$ ( $\text{\AA}^{-1}$ )	1.0011	0.35614	0

Table 4.1: Pair-type dependent parameter set for the Brenner potential for Ru-C systems.

on Ru(0001) and Ru NPs deposited on carbon substrates.

Similarly to the previous chapter, the carbon parameters were taken from the original source [101], and more specifically its Table III, without the overbinding corrections that are mostly relevant for radicals. These parameters are summed up in Table 4.1. For pure ruthenium, the parameters were borrowed from the work by Li and coworkers [215] who managed to successfully reproduce various properties of hcp Ru, including the experimental cohesive energy, the lattice and elastic constants. In contrast with the original work of Li *et al.*, who used a sharp cut-off at 4  $\text{\AA}$  [215], the same smooth function  $f^{ij}(r)$  already used in the BOP was employed here with inner and outer cut-off radii at 4  $\text{\AA}$  and 4.3  $\text{\AA}$ , respectively. The other parameters of the Ru-Ru potential are detailed in Table 4.1 as well.

### 4.2.1 Parametrization

No set of parameters corresponding to unlike Ru-C pairs is available in the literature. Therefore the PTMC procedure presented in chapter 2 has been used for the search of an appropriate Brenner BOP parameter set for Ru-C. Locally optimized geometries of epitaxial graphene on Ru(0001) and small adsorbates thereon, obtained by dispersion-free DFT calculations by Bocquet and coworkers [201, 206] served as reference data. The training set comprised configurations with three relaxed structures of graphene on Ru(0001): A 12 on 11 and a 13 on 12 moiré structure containing three Ru(0001) layers and a 13 on 12 geometry containing four of such layers, all obtained from DFT calculations [206]. In addition, two configurations with a Ru adatom (Ru trimer) on a 12 on 11 moiré at the low fcc moiré registry and at the hollow (bridge) adsorption site were included as well, again originating from electronic structure calculations at the same level of theory [201]. The exact definitions and more details about these structures can be found in Ref. [201] and [206]. The data to be reproduced included adsorption energies of graphene on the Ru(0001) metal, and of the Ru adsorbates on epitaxial graphene on ruthenium. The adsorption energy of a system composed of two subsystems is defined as  $E_{\text{ads}} = E_{\text{total}} - E_{\text{sub}}^{(1)} - E_{\text{sub}}^{(2)}$ , where  $E_{\text{total}}$  is the potential energy of the entire system after local relaxation,  $E_{\text{sub}}^{(1)}$  and  $E_{\text{sub}}^{(2)}$  the energies of the two subsystems optimized at infinite separations. The members of this training set and the target values are listed in Table 4.2.

In the error function of Eq. (2.27), the weighting parameters  $\rho_i$  were taken as 20  $\text{\AA}^{-2}$  and 100  $\text{\AA}^{-2}$  for configurations without and with adsorbates. The Brenner BOP parameters were

Property	DFT	DFT reference	BOP
Graphene corrugation	1.51	[206]	1.50
Uppermost Ru layer corrugation	0.05	[206]	0.06
Smallest graphene-metal separation	2.22	[206]	2.43
Average graphene-metal separation	2.57	[206]	2.81
Graphene-Ru <sub>3</sub> distance	2.06	[201]	2.63
Graphene adsorption energy	-3.9	[206]	-3.57
Graphene interaction energy	-10.0	[206]	-6.96
Graphene deformation energy	5.7	[206]	3.28
Ru(0001) deformation energy	0.4	[206]	0.12
Ru <sub>3</sub> adsorption energy (eV/atom)	-0.77	[201]	-0.10

Table 4.2: DFT reference data [201, 206] for graphene on Ru(0001) structures employed for the parametrization procedure, and predictions of the present BOP Unless otherwise mentioned, all distances and energies are in Å and eV, respectively. All data are without dispersion correction.

first optimized globally using a PTMC procedure with 24 replicas geometrically distributed in the pseudo temperature range between  $T_1 = 2 \cdot 10^{-2} \text{ eV}^2/\text{Å}^2$  and  $T_{24} = 2 \cdot 10^9 \text{ eV}^2/\text{Å}^2$ . For each replica,  $2.5 \cdot 10^5$  MC cycles were performed. A subsequent PTMC simulation with the same number of steps was carried out starting from the parameter set minimizing  $\chi^2$ , using pseudo temperatures lowered by a factor 20. Finally, low- $\chi^2$  configurations from all replicas were further refined locally using the Levenberg-Marquardt algorithm and structural relaxations at each optimization step.

The Ru-C parameters optimized using this procedure are shown in Table 4.1, and the quality of the potential for reproducing the target values can be appreciated from the last column of Table 4.2. Overall the agreement between target and obtained values is very satisfactory, which confirms the ability of the original BOP to describe such complex substrates and the possible presence of adsorbates. The main residual discrepancy is the adsorption energy of the deposited trimer, which is too low with the BOP. However, reoptimizing the trimer in presence of dispersion corrections (see general discussion below) significantly stabilizes it, the adsorption energy increasing from 0.097 eV/atom to 0.645 eV/atom, in much better agreement with the (dispersion-free) DFT results of Sutter and coworkers [201]. It would be useful to quantify the effects of dispersion forces at the DFT level also for this system.

### 4.2.2 Pauling relation

One possible way to assess the transferability of the potential to situations away from the training set consists of correlating the bond energy to the equilibrium distance under various configurations. This so-called Pauling relation [98] has been shown by Albe and coworkers [96] to be a suitable testing ground for measuring the quality of BOPs away from their training set. The Pauling relation imposes constraints on various parameters of the BOP. If only nearest-neighbor properties are included in the training set, it is possible to fit a potential in such a way that the Pauling relation is automatically satisfied. The collective properties of interest here such as the amplitude of graphene corrugation or the size of moiré domains extend beyond the first neighbors and are not directly impacted by the Pauling relation. However, it remains interesting to see how the BOP performs toward this relation especially when compared to more realistic calculations based on explicit electronic structure.

In principle, the non angular-dependent part of a BOP can be determined straightforwardly by considering the properties of a dimer and one other compound  $B$  of the desired chemical

species. The dimer bond length directly gives  $r_0$ , the binding energy  $D_0$  and the vibrational frequency  $\omega$  that are related to  $\beta$ :

$$\beta = 2\pi\omega\sqrt{\frac{\mu^*}{2D_0}}, \quad (4.1)$$

where  $\mu^*$  designates the reduced mass of the dimer. Taking into account first neighbor interactions only, a relation can be found between  $S$ , the energy per bond  $E_B$  and the nearest neighbor distance  $r_B$  of compound  $B$  as [96]

$$S = \frac{1}{2} \left[ \frac{\ln(-E_B/D_0)}{\beta(r_0 - r_B)} \right]^2. \quad (4.2)$$

The energy per bond as a function of the equilibrium nearest neighbor distance for several Ru-C compounds [diatomic, NaCl structure (B1), CsCl structure (B2) and zinc-blende structure (B3)] have been determined with the present Ru-C parametrization and compared to existing data for the Ru-C diatomic [224, 225] and the B1 and B3 mixed structures [226]. These data together with the above Pauling relation are represented in Fig. 4.1. Energies per bond of

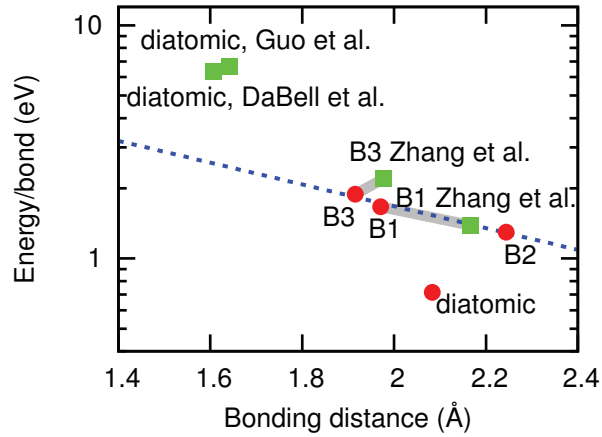


Figure 4.1: Satisfaction of Pauling relation (dotted line) for assessing the Ru-C BOP in different compounds: NaCl (B1), CsCl structure (B2), zinc-blende (B3) and diatomic computed with the BOP (red dots) and literature data (green squares) from Guo and coworkers [225], and DaBell and coworkers [224], and Zhao and coworkers [226].

$-1.67$  eV,  $-1.30$  eV and  $-1.89$  eV have been obtained at nearest neighbor distances of  $1.97$  Å,  $2.24$  Å and  $1.92$  Å for the B1, B2 and B3 compounds, respectively. The exponential decrease of the bond strength with increasing bond distance indicates a very satisfactory behavior of the present model toward the Pauling relation. The agreement with existing DFT calculations for the structures B1 and B3, where bond energies of  $-1.39$  eV and  $-2.20$  eV at bond distances of  $2.17$  Å and  $1.98$  Å have been found [226], is also noteworthy both for the bond energy and equilibrium distance, especially considering how far these compounds are from the training set. However, for the bare RuC diatomic the Pauling relation is not satisfied, with a markedly long bond length of  $2.08$  Å and too low binding energy of  $-0.72$  eV. Electronic structure calculations for this molecule [225] indicate a strong chemical bond with a significant charge transfer, the Pauling relation being not fulfilled. Though lesser in magnitude, deviations from the expected behavior are also noted for the zinc-blende compounds at the DFT level. These deviations mitigate the apparent limitations of the present model, the ionic character could also explain why the adsorption energy of the trimer on epitaxial graphene is predicted to be too low.

### 4.2.3 Dispersion corrections

In order to account for dispersion interactions, the empirical Grimme D2 [76] correction was added to the BOP which only accounts for metallic and covalent interactions due to its short cut-off distance. Following our previous calculations on Pt-C systems, we have also considered the possible screening of dispersion interactions involving delocalized electrons over extended media, as relevant here for the bulk ruthenium metal [84]. Following earlier authors [61, 168], such screening effects were accounted for empirically by including dispersion interactions in the D2 model limited to the uppermost layer of Ru atoms only.

Finally, the BOP was also used to model Ru adsorbates on pure carbon substrates such as graphene or graphite. Again, the LJ pairwise potential of Che and coworkers [118] was employed between any pair of atoms belonging to different graphene layers, no additional dispersion correction being included for these intra-substrate contributions in order to avoid double counting. In order to focus this chapter on the covalent interactions, the coarse graining approach for dispersion forces presented in the previous chapter has not been employed. Instead, only the explicit, atomistic dispersion correction à la Grimme D2 was used.

## 4.3 Simulation details

In the static limit, several geometric and energetic properties were calculated for a number of adsorbates on graphite and on epitaxial graphene on Ru(0001). At finite temperature, locally relaxed structures produced during the parametrization stage further served as initial configurations for MD simulations. Several geometric properties were calculated to monitor the thermal response of the graphene layer on the Ru(0001) metal for different moiré configurations, including the corrugation amplitude and average graphene-metal distance.

Adsorbates on graphene, graphite, and epitaxial graphene on Ru(0001) were also simulated at finite temperature. From the MD trajectories, the global diffusion properties were addressed by calculating the MSD of the center of mass, from which the diffusion constant could in turn be evaluated. The velocity time autocorrelation function was also calculated over windows of 40 ps at intervals of 8 fs and Fourier transformed to get the vibrational spectrum for various systems. This sets the spectral resolution to  $1 \text{ cm}^{-1}$  and a maximum detectable frequency of  $2085 \text{ cm}^{-1}$ .

Unless otherwise mentioned, the MD trajectories employed a time step of 1 fs and were propagated over 5.5 ns, with the first 0.5 ns disregarded as equilibration period. The simulations were performed in the canonical ensemble using a Nosé-Hoover thermostat. In order to avoid any perturbation from the thermostat on the physical properties under evaluation, the thermostat was not directly coupled to the system of interest (adsorbate or epitaxial graphene layer), but only to the remaining substrate (graphene, graphite or hcp ruthenium). The bottom layer was also kept fixed so as to prevent undesired drifting of the entire simulation cell.

The graphite substrate was modeled explicitly using three layers (ABA fashion) and  $10 \times 10$  graphene unit cells per layer, at a surface density matching the equilibrium lattice constant of graphene in the Brenner model of  $2.51 \text{ \AA}$  at 0 K. In the case of GOM, the graphene layer plus three Ru(0001) layers were taken into account, with lateral system sizes imposed by the commensurability of the moiré. The structures considered here comprised the 12 on 11, the 13 on 12 and the 25 on 23 moirés. In all calculations, lateral periodic boundary conditions of fixed size were applied. In the calculations of epitaxial graphene on Ru(0001), the simulation box was fixed with respect to hcp ruthenium, for which a lattice constant of  $a = 2.724 \text{ \AA}$  was imposed, the lattice constant of graphene being left to fluctuate as no boundary condition except at the

bottom layer was applied in the corresponding direction. This choice imposes a strain on the epitaxial graphene layer depending on the moiré commensurability and temperature.

## 4.4 Results

The interatomic potential was applied to epitaxial graphene on Ru(0001) and Ru adsorbates on carbonaceous substrates. In order to evaluate the performance of the BOP in a variety of situations, we have considered structural and energetic properties in the static limit, as well as dynamical properties at finite temperature.

### 4.4.1 Static properties

#### Single Ru atom on graphene and graphite

A single ruthenium adatom on graphene and graphite was chosen as the most straightforward testing case for the present model, especially for discussing the possible role of dispersion forces on such extended substrates. Energy profiles of a Ru adatom approaching the flat graphene and graphite surfaces were calculated along high symmetry sites. The alpha and beta sites are found directly over a substrate C atom and differ only from the presence of another C atom at the alpha position in the subsequent graphitic layer, whereas the beta site lies above the center of a six-membered carbon ring (in graphene, the alpha and beta sites are thus equivalent to each other). The bridge and hollow sites lie over a C-C bond and the center of a six-membered carbon ring, respectively. See also Fig. 3.1.

The corresponding energy profiles along these four adsorption sites were calculated using the regular BOP and its dispersion-corrected version. Without any dispersion contribution, the results for planar graphene and graphite are identical to each other, hence only three curves are shown in Fig. 4.2. For this simple system the results indicate that dispersion forces have

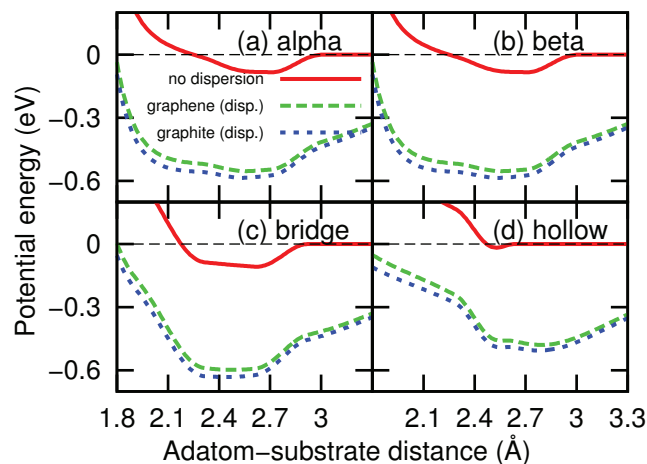


Figure 4.2: Interaction energy of a Ru adatom approaching planar graphene and graphite substrates along various high symmetry sites, as a function of the distance from the surface. The profiles have been computed with the BOP for Ru-C with and without dispersion correction.

a significant effect on the binding energy and, to a lesser extent, on the equilibrium distance between the adatom and the surface.

In presence of dispersion forces, the bridge site appears as the most stable for both substrates ( $-0.60$  eV binding energy for graphene,  $-0.63$  for graphite), followed by the alpha and beta

sites ( $-0.55/-0.59$ ) and finally the hollow site ( $-0.48/-0.51$ ), the difference between the alpha and beta sites being negligible also for graphite. Without dispersion corrections, these values are reduced by about half an eV. The role of dispersion forces is also manifested on the slightly higher binding energies obtained on graphite relative to graphene, by about 0.03 eV for all adsorption sites.

Dispersion interactions also affect the equilibrium position of the adatom, but in a rather nontrivial way that depends on the site. At the hollow position, dispersion forces push the minimum away from the surface by 0.2–0.3 Å, whereas they pull the system 0.1–0.2 Å closer to the surface for the three other sites. This behavior results from the very shallow nature of the hollow minimum, which in the present model is barely bound at all in absence of dispersion forces. Relative to graphene, dispersion forces further shift the minima of Ru adatoms closer to the graphite surface by 0.02–0.04 Å depending on the adsorption site.

It is instructive to consider the lateral energy maps obtained by scanning the unit cell and minimizing the energy along the perpendicular distance. These maps, as calculated for graphite with and without dispersion corrections, are shown in Fig. 4.3.

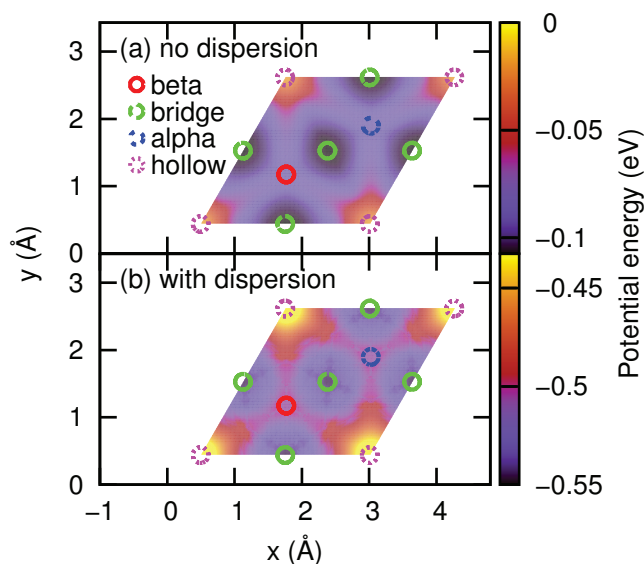


Figure 4.3: Potential energy map of Ru adatom throughout the graphite unit cell, as obtained from the BOP without (a) and with (b) dispersion corrections.

Besides energy profiles on selected sites, energy maps have been calculated by minimizing the energy of a Ru adatom along the perpendicular distance throughout the entire unit cell of graphite. These maps confirm the bridge position as the most stable within the present models. Furthermore they demonstrate the absence of other metastable adsorption sites, which suggests that surface diffusion can proceed from one bridge site to the next via low barriers of less than 0.05 eV.

### Larger Ru adsorbates on graphite

The BOP model was subsequently applied to increasingly large Ru NPs deposited on graphite, for which DFT calculations would be less practical. Ruthenium nanoclusters of icosahedral and truncated octahedral structure (Wulff shapes) and up to 3871 atoms were deposited on graphite and subjected to local relaxations. Initially a (111) facet was put into epitaxial contact with the substrate.

In the case of a Ru adatom, which has already been discussed above, local geometry optimizations have been carried out at all high symmetry sites. The bridge site remains the most stable one in calculations without and with dispersion, with adsorption energies of  $-0.67$  eV and  $-0.15$  eV at closest Ru-C distances of  $2.43$  Å and  $2.71$  Å, respectively. Upon relaxation, also the alpha and beta site become metastable with adsorption energies of  $-0.61$  eV (including dispersion) and  $-0.11$  eV (without dispersion) at a Ru-C separation close to  $2.5$  Å weakly dependent on dispersion corrections.

The deposition of the icosahedral  $\text{Ru}_{13}$  cluster on graphite is still most stable when the three atoms in contact with the substrate surface occupy the bridge position. The distance of the trimer to the uppermost graphene layer is about  $2.7$  Å (without dispersion) and  $2.3$  Å (including dispersion) and the adsorption energy with the substrate is  $-0.99$  eV/atom, or about  $-0.11$  eV/atom in relaxations with and without dispersion, respectively. However, the closest separation to the substrate does not change significantly compared to the single adatom.

The larger highly symmetric clusters were all initially placed with one facet in epitaxial contact with the substrate. The center of the contact facet was put into the epitaxial bridge positions. However, due to unequal lattice constants of the two materials, the adsorption sites of the contact facet atoms of the adsorbate away from the center may face other sites. In return, such strain effects lead to a noticeable buckling of the graphite surface that can be as high as  $1.2$  Å in calculations including dispersion and still reach  $0.5$  Å when dispersion is disregarded. The distortions of the adsorbates remain very limited, though, especially in absence of dispersion corrections. Their closest distance to an atom of the substrate ranges from  $2.5$  Å to  $2.7$  Å when dispersion is neglected and from  $2.0$  to  $2.4$  Å including dispersion. These closest distances do not differ markedly between icosahedral and truncated octahedral adsorbates.

As shown in Fig. 4.4, the adsorption energy is almost proportional to the number of atoms at the contact facet in the case of the largest clusters, which is the expected behavior in the bulk limit. The difference in interaction energy per facet atom between the two types of adsorbed NPs is explained by the larger fraction of atoms in contact for the Wulff particles. The slightly decreasing strength of the substrate interaction with adsorbate size can be attributed to the diminishing portion that cluster edges contribute to the overall binding. The adsorption of small

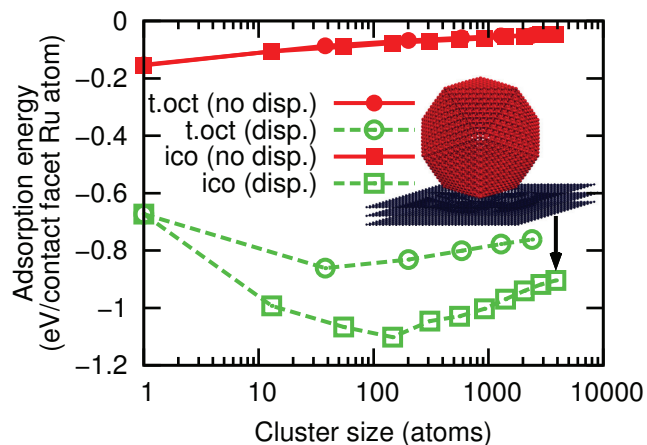


Figure 4.4: Adsorption energy of icosahedral (ico) and truncated octahedral (t.oct) adsorbates on graphite obtained in local relaxations with and without Grimme D2 dispersion correction.

ruthenium adsorbates on graphene and graphite has been theoretically addressed in the past from DFT, usually focused on the adatom case. The most stable adsorption site on graphene

was found by various authors to be the hollow site, with an adsorption energy ranging from -3.2 eV [227] to -4.03 eV [228] and -4.43 eV [229], with a closest separation Ru and C atoms between 1.62 Å [229] and 2.23 Å [227]. The migration barrier has also been estimated to range between 0.72 eV [228] and 0.96 eV [229]. Clearly these energetic and structural properties do not fully agree with the predictions of the present model, which we attribute essentially to its poor description of charge transfer (almost one electron) in the case of the single adatom [227]. This is also related to the aforementioned weak performance of the BOP to reproduce the properties of the bare RuC diatomic.

Electronic structure calculations for Ru adsorbates larger than the trimer are scarce, but a noteworthy effort from Gao and Zhao on the Ru<sub>13</sub> cluster adsorbed on the outer face of (12,12) carbon nanotubes deserves mentioning [227]. These authors reported a Ru-Ru bond distance of 2.62 Å in the free Ru<sub>13</sub>, which increases by 9% upon deposition on the nanotube. For this adsorbate the most stable adsorption sites were found to be the top and bridge positions. These results on Ru<sub>13</sub> compare well with our data obtained for the flat graphite substrate, with similar most stable adsorption sites. This provides strong support for the model in its ability to treat larger adsorbates.

### Epitaxial graphene on Ru(0001)

The bond-order model was also employed in situations closer to its training set, to treat epitaxial graphene on Ru(0001) but under different commensurability ratios. In simulations performed with a common periodic box, the moiré dimensions have to be imposed in advance, which entails some tensile or compressive strain depending on commensurability, leading in turn to possible variations in the calculated properties at zero or finite temperatures. Here we have focused on the 12 on 11, 13 on 12 and 25 on 23 moirés, the latter being closest to experimental observations but also harder to address with explicit descriptions of electronic structure. The two smaller moirés provide upper and lower limits on the strain imposed by the common box size on the graphene layer, while offering a computationally more convenient size about four times smaller than the 25 on 23 structure. The scaling ratios imposed to graphene relative to the Ru(0001) surface amount to 0.9938, 0.9974 and 1.0007 for the 12 on 11, the 25 on 23, and the 13 on 12 moiré structures, respectively.

Upon structural optimization, the interaction between the graphene layer and the Ru(0001) surface induces corrugation in both materials by amplitudes that we denote  $\Delta_{\text{gr}}$  and  $\Delta_{\text{Ru}}$ , respectively. We further denote by  $\Delta_{\text{Ru,gr}}$  the shortest distance of the graphene layer from the laterally averaged position of the topmost Ru layer. These observables, together with the average adsorption energy  $E_{\text{ads}}$  per carbon atom, are listed in Table 4.3 as obtained from calculations without and with dispersion corrections using the screened version of the Grimme D2 model.

Including dispersion corrections generally reduces the corrugation of the graphene layer and pulls it about 0.1–0.2 Å closer to the metal surface. Energetic stability is strongly increased by these long-ranged forces. These static properties appear relatively independent on the particular moiré commensurability, and only the corrugation of the graphene layer depends rather strongly on lateral strain imposed by the simulation box. Comparison with existing DFT results also listed in Table 4.3 indicates very satisfactory agreement for all observables. In particular, we note that adding the dispersion correction has very similar consequences in the model and in the DFT calculations, which was achieved without additional fitting parameter. The screening effect of dispersion forces due to delocalized electrons in the metal seems to be of limited importance, calculations with the unscreened original Grimme D2 model leading to adsorption energies only 21% larger than those computed with the screened version. In contrast, fully

Method	System/size	$\Delta_{\text{gr}}$ (Å)	$\Delta_{\text{Ru}}$ (Å)	$\Delta_{\text{Ru,gr}}$ (Å)	$E_{\text{ads}}$ (meV)
BOP	12 on 11	1.50	0.06	2.43	-12.4
BOP	13 on 12	0.99	0.05	2.43	-16.8
BOP	25 on 23	1.33	0.06	2.42	-14.3
BOP + screened dispersion	12 on 11	0.66	0.11	2.19	-213.5
BOP + screened dispersion	13 on 12	0.57	0.04	2.24	-220.0
BOP + screened dispersion	25 on 23	0.51	0.05	2.34	-217.3
PBE [199]	12 on 11	1.5		2.2	-23.3
PBE [205]	12 on 11	1.67	0.2	2.2	-21
PBE [205]	11 on 10	1.75		2.3	-11
GGA [194]	12 on 11	0.4			
DFT [187]	12 on 11	1.65		2.13	
PBE [206]	12 on 11	1.51	0.05	2.22	-13.5
PBE [206]	13 on 12	1.44	0.04	2.24	-8.0
PBE [188]	12 on 11	1.50		2.1	
PBE [188]	13 on 12	1.59	0.1	2.2	
PBE [200]	$(\sqrt{91} \times \sqrt{91})R_{\text{gr}}5.21^\circ$	1.8		2.2	
PBE [67]	11 on 10				-27
PBE + D2 [67]	11 on 10	1.195	0.045	2.195	-206
PBE + scr. D2 [67]	11 on 10	1.239		2.242	-163
revPBE + D2 [202]	12 on 11	1.17		2.18	-224
PBE + vdW [200]	$(\sqrt{91} \times \sqrt{91})R_{\text{gr}}5.21^\circ$	1.3		2	-181.6
revPBE + dispersion [203]	11 on 10	1.27			-210
revPBE + dispersion [203]	12 on 11	1.17			-220
revPBE + dispersion [203]	13 on 12	1.11			-230
revPBE + dispersion [203]	25 on 23	1.16	0.17	2.09	-240
Surface segregation, STM [191]	30 Å, 12 on 11	1.1			
Surface segregation, STM [192]	30 Å	1			
CVD, SXRD, parametric model [181]	25 on 23	1.5	0.2	2.2	
CVD, SXRD, CTR [181]	25 on 23	$0.82 \pm 0.15$	$0.19 \pm 0.02$	2.0	
CVD, STM [182]	27 Å	0.2-1.2			
surface segregation, LEED [194]	30 Å				
CVD, STM [187]	12 on 11	1.7			
CVD, LEED [188]	13 on 12	$1.53 \pm 0.2$	0.26	2.1	

Table 4.3: Moiré structures of graphene on Ru(0001): Structural properties, including graphene corrugation  $\Delta_{\text{gr}}$ , Ru(0001) corrugation  $\Delta_{\text{Ru}}$  and the lowest spacing  $\Delta_{\text{Ru,gr}}$  between the graphene layer and the metal surface; adsorption energy  $E_{\text{ads}}$  of graphene on Ru(0001) per carbon atom as obtained upon structural optimizations without and with screened dispersion corrections, as well as electronic structure and experimental reference data.

neglecting dispersion forces leads to a 13–17-fold decrease in the adsorption interaction. Stradi and coworkers [67] carried out structural optimizations of the 11 on 10 moiré, evaluating the effects of dispersion forces and their screening on the resulting structure. These authors scaled down the dispersion coefficients to mimic screening and found adsorption energies of  $-27$ ,  $-206$  and  $-163$  meV per carbon atom in calculations without dispersion, with unscreened dispersion and with screened dispersion, respectively. They adjusted their scaling factor for the  $C_6$  coefficients so as to reproduce the experimental interlayer distance and exfoliation energy of graphite. Their values are fully consistent with the general trends obtained with the present model.

Several predictions can also be compared to experimental measurements obtained using different methods such as STM, surface x-ray diffraction (SXRD), x-ray crystal truncation rod scattering (CTR) or LEED, and carried on different moiré structures produced by CVD, as listed in the bottom part of Table 4.3. Here also, good overall agreement is reached for most structural properties, except perhaps for the buckling of the uppermost ruthenium layer which appears somewhat underestimated in the present calculations. One cause for such discrepancies could be the finite temperature employed in the experiments, and such effects are discussed in the following section.

Nevertheless, the adsorption energy of the graphene layer on Ru(0001) as obtained with the screened dispersion model slightly exceeds the reference values from Stradi and coworkers [67]. In order to better reproduce this reference value, and in addition to taking only the topmost Ru(0001) layer into account, we attempted to scale the  $C_6$  coefficients. Fig. 4.5 shows the adsorption energy of epitaxial graphene, its corrugation and its smallest distance to the Ru(0001) surface as a function of the fraction of the Grimme D2 dispersion coefficients obtained for locally optimized structures of the 12 on 11 and 13 on 12 moirés. The figure indicates also the values from Ref. [67] for these three properties. Unfortunately, it was not possible to reproduce them all simultaneously and therefore the original (100%) Grimme D2 coefficients were kept for the subsequent simulations. Both the adsorption energy of the graphene sheet and its distance from the substrate surface vary linearly with dispersion strength. However, the corrugation of the graphene sheet does not follow such a simple trend when dispersion is weak ( $C_6/C_6^{(D2)} < 20\%$ ), and larger discrepancies appear for the two moiré structures. The strain imposed by the simulation box on the graphene layer is compressive for the 12 on 11 structure but tensile for the 13 on 12 structure, which naturally reduces the corrugation for the latter. Until dispersion is strong enough to flatten the graphene layer, the strain difference induces the discrepancies in the corrugation. In the strong dispersion regime, the differences between the two moiré commensurabilities become less pronounced and the corrugation may slightly increase due to the geometric effect of the moiré caused by the stronger contact with the Ru(0001) surface.

The deformation of the graphene layer in the 25 on 23 moiré has been closely examined for a more detailed comparison with literature data [185]. Fig. 4.6(a) defines relevant registries for this moiré structure. The geometry of the graphene layer on top of two hcp (0001) layers is very similar to the one of graphene on top of two fcc (111) layers. The differences are the spacing between the metal layers and the stacking if more than two metal layers are taken into account. Therefore the moiré registries take different names for graphene/Ru(0001) as compared to graphene/Pt(111) (see Fig. 3.11). In the (top, hcp) region, the carbon atoms are on top of Ru atoms of either the first or second Ru layer. In the (hcp-fcc) region, the center of the 6-membered carbon rings are on top of the Ru atoms of the uppermost layer. Finally, the (fcc, top) region has these rings aligned with the atoms of the second Ru layer. Panel (b) shows the height of the carbon atoms or the corrugation of the graphene layer as a color coded graph. The hills are located in the (hcp, fcc) region, whereas the closest approach to the metal surface is found in the (fcc, top) region, but similar closest distances to the

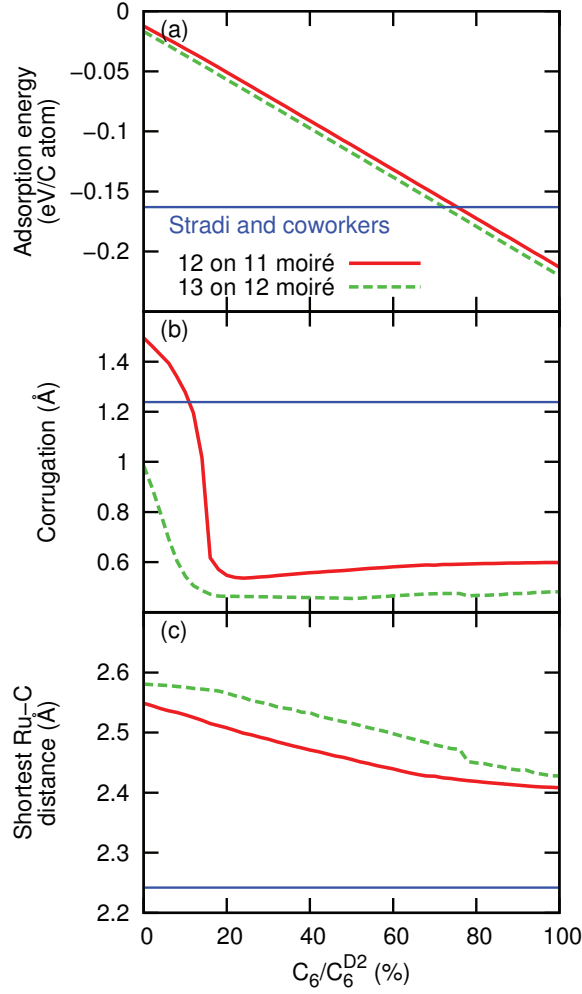


Figure 4.5: Properties of graphene on Ru(0001) moirés as a function of dispersion strength as obtained upon local relaxations. Only the first layer is included in order to account for screening effects. Additionally the Grimme D2  $C_6$  coefficients have been scaled. Literature DFT values (from calculations including screened dispersion correction) from Stradi and coworkers [67] are also indicated; (a) Adsorption energy of graphene; (b) Graphene corrugation; (c) Closest distance between the graphene and the Ru(0001) surface.

metal surface are also found in the (hcp, fcc) region. These overall trends are the same when dispersion is neglected, only the shape of the hills and valleys may vary. In both experiments and electronic structure calculations, there is a wide consensus on this overall geometry of the graphene corrugation [185, 188, 194, 201, 202, 206, 222], which suggests that the present Ru-C Brenner parametrization is a good description for the graphene/Ru(0001) system for which it was developed.

Some evidence for chirality in the epitaxial graphene layer (corresponding to slight inplane twists) was found by Martoccia and coworkers [185]. This could have interesting applications for chiral recognition of adsorbates or for spin polarization. However, the existence of such a chiral domain in graphene/Ru(0001) could not be confirmed in some later studies [203, 230]. Fig. 4.6(c) shows the displacements of carbon atoms in the graphene/Ru(0001) with respect to freestanding graphene. The highest displacements occur on the flanks of the hills, but no chirality, which would correspond to a breaking of the symmetry along the long diagonal axis, is distinguishable.

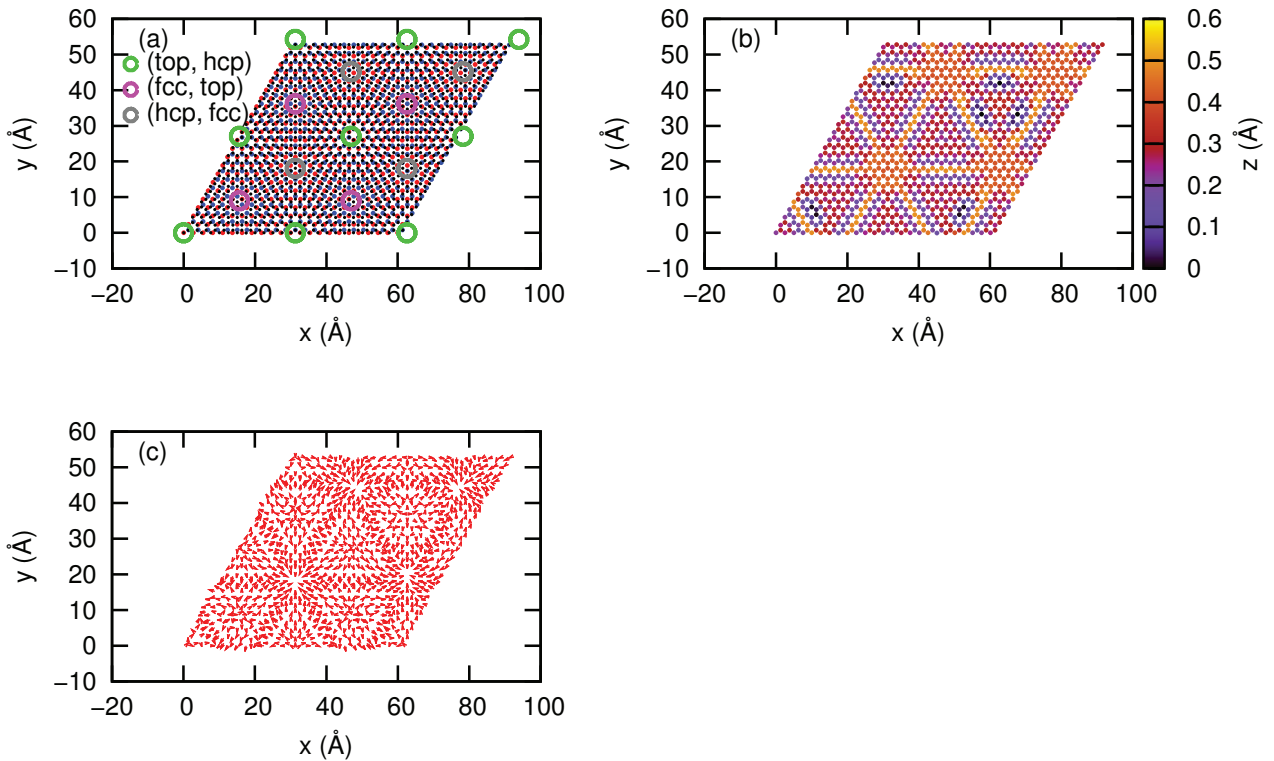


Figure 4.6: Local relaxation of the graphene layer in the 25 on 23 moiré, as described using the screened dispersion model. (a) Top view: graphene: black, first Ru(0001) layer: red, and second Ru(0001) layer: blue. The different moiré registries are highlighted and explained in the text; (b) Graphene corrugation: The hills are located in the (hcp, fcc) registry; (c) Lateral displacement (magnified by 50) of C atoms in the epitaxial graphene with respect to free graphene. A possible chirality is not discernible.

## 4.4.2 Finite temperature dynamics

The production of NPs with a narrow size distribution is essential in catalysis and information storage. One experimental way of optimizing size selection consists of preforming the NPs and soft-landing them on the substrate of interest [231]. It is important that the NPs thus designed be thermally stable over reasonably long time scales. The present BOP model is convenient for addressing this issue with MD directly at the atomistic level. We use the two Lindemann indices as defined in Eq. (2.61) and Eq. (2.62) to measure the amount of fluctuations within the NP or between the particle and the substrate (graphite or epitaxial graphene), respectively. The Lindemann indices should be considered as qualitative, in the sense that they provide information only about the nature of the dynamics, but not about the isomerization or diffusion rates. In addition to these dynamical indicators, the shape of the adsorbate was quantified from the asphericity index as defined in Eq. (2.63).

### 4.4.2.1 Ru adsorbates on graphite

**Thermal stability** MD simulations have been performed for  $\text{Ru}_{38}$  and  $\text{Ru}_{201}$  initially deposited with (111) facets in epitaxy on the honeycomb lattice of the graphite surface, at temperatures ranging between 100 and 1500 K, and using the explicit Grimme D2 approach to account for dispersion forces, or neglecting them altogether. Fig. 4.7 shows the evolution of

the three dynamical and geometrical parameters  $\delta_{\text{intra}}$ ,  $\delta_{\text{inter}}$  and  $\chi$  as a function of increasing temperature. In absence of dispersion forces, the two NPs keep vibrating around their initial configurations but eventually desorb at 500 K (Ru<sub>38</sub>) or 1100 K (Ru<sub>201</sub>) under the time scales of nanoseconds covered by the MD trajectories.

Once dispersion interactions are included, the NPs appear much more thermally stable and do not desorb from graphite even at 1500 K. As commonly shown by the sharp increase in  $\delta_{\text{intra}}$  and  $\chi$ , the smaller 38-atom system rearranges near 700 K into a much less spherical and flatter structure, but remaining three-dimensional. Internal rearrangements also occur in the larger adsorbate, but require a much higher temperature  $T > 1300$  K to become discernible. As shown by the substrate-adsorbate fluctuation index  $\delta_{\text{inter}}$ , all adsorbates but Ru<sub>201</sub> bound by dispersion-corrected forces exhibit significant mobility over the substrate already below room temperature. This mobility can be quantified further by calculating the surface diffusion coefficient  $D$  from the long time variations of the MSD of the adsorbate center of mass.

**Surface diffusion** Figure 4.8 shows the resulting diffusion coefficients obtained for both adsorbates bound to the substrate with additional dispersion forces, and for Ru<sub>201</sub> in absence of dispersion corrections but limited to  $T < 1100$  K since above this limit thermal desorption occurs. The logarithmic plot of  $D$  versus  $1/T$  clearly shows that the diffusion constants follow the Arrhenius behavior of Eq. (2.65). Values for the activation energy of  $E_{\text{act}} = 0.31$  eV and 0.14 eV are obtained for Ru<sub>201</sub> in simulations with and without dispersion correction, respectively. The higher values obtained for the activation energy for dispersion-corrected interactions are of course consistent with the lower mobility inferred from Fig. 4.7(b) and from the greater binding of the NPs on the substrate with dispersion contributions (see Fig. 4.4). This result confirms the importance of the dispersion correction for the stability of the clusters and emphasizes their role at finite temperature. For the Ru<sub>38</sub> in calculations including the dispersion correction, activation energies of 0.35 eV and 0.11 eV are obtained at high and low temperatures, respectively. The higher value of the activation energy high temperature is consistent with the large contact area of this system after it has annealed and left the truncated octahedral shape.

Such high adsorbate mobilities are also consistent with experimental results [41], where fast diffusion of metal clusters on graphite has been attributed to the very flat potential energy surface felt by the adsorbates owing to the longer equilibrium distance between metal and carbon atoms relative to carbon-carbon interactions.

#### 4.4.2.2 Epitaxial graphene on Ru(0001)

**Geometrical properties** The thermal stability of epitaxial graphene on Ru(0001) has also been evaluated using the same computational methodology for the moiré structures described in Table 4.3. From 1 ns long MD simulations, the corrugation of the graphene layer was evaluated from the standard fluctuations of the Cartesian coordinate  $z_{\text{C},i}$  of the carbon atoms in the normal direction to the surface:

$$\Delta'_{\text{gr}} = [\langle z_{\text{C},i}^2 \rangle - \langle z_{\text{C},i} \rangle^2]^{1/2}. \quad (4.3)$$

The distance between the Ru(0001) surface and the graphene layer is here redefined as the difference between  $\langle z_{\text{C},i} \rangle$  and the corresponding averaged coordinate  $\langle z_{\text{Ru},i} \rangle$  of the topmost Ru layer. The advantage of these new observables over earlier definitions chosen for comparison with DFT data and based on upper and lower distances is their lesser dependencies on extreme values, hence on system size. However, in comparing the two definitions of corrugation it is

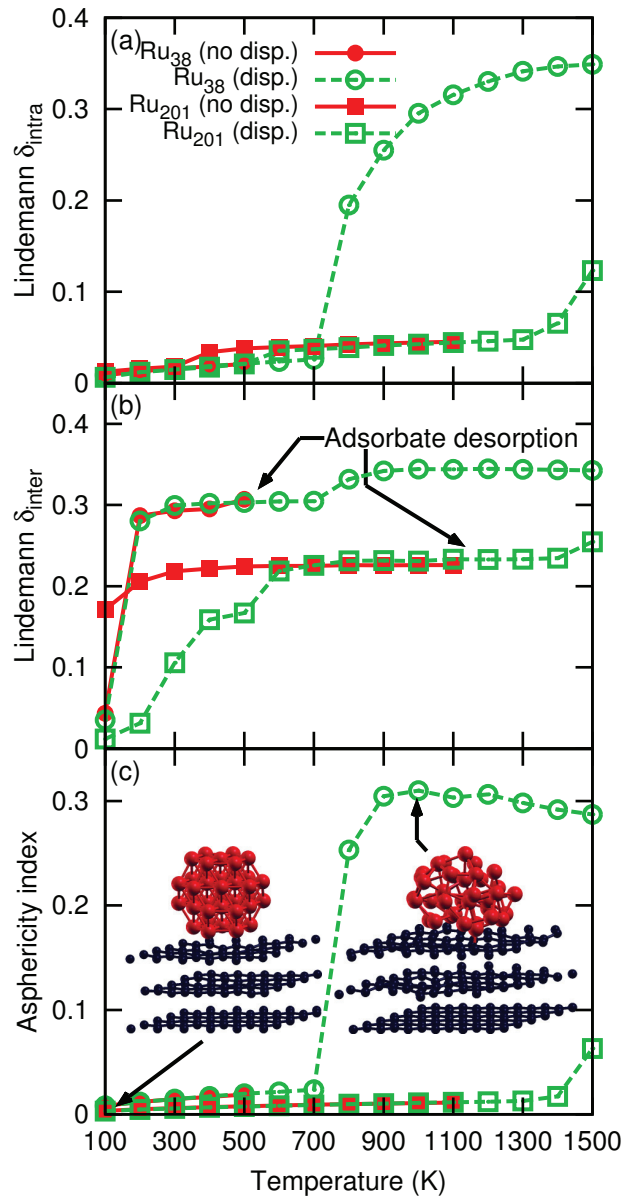


Figure 4.7: Shape and thermal stability of  $\text{Ru}_{38}$  and  $\text{Ru}_{201}$  on multilayer graphite, quantified by (a)  $\delta_{\text{intra}}$ , (b)  $\delta_{\text{inter}}$  and (c) the asphericity index  $\chi$  as defined in Eqn. (2.61)–(2.63), and as obtained from MD simulations based on the BOP model corrected for dispersion forces (disp.) or uncorrected (no disp.).

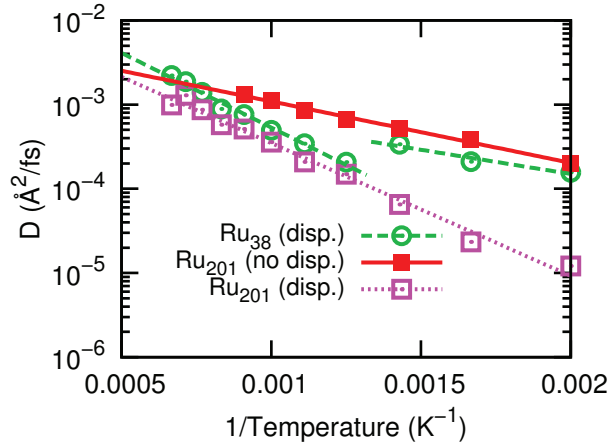


Figure 4.8: Surface diffusion coefficients of  $\text{Ru}_{38}$  and  $\text{Ru}_{201}$  on graphite shown as an Arrhenius plot. The simulation data were obtained from MD trajectories at temperatures covering the range 500–1500 K, and linear interpolations are also shown.

important to notice that the value obtained from the statistical fluctuations (in time and space) is only a fraction of the one based on extreme values.

Fig. 4.9 shows the variation of  $\Delta'_{\text{gr}}$  with temperature for the three moiré structures 12 on 11, 13 on 12 and 25 on 23, as obtained from simulations using the BOP model with and without dispersion corrections. Here, all dispersion corrections were screened by considering only the contribution of the uppermost metal layer. As expected, temperature generally leads to an increase in the corrugation of the graphene layer. As already found in the static case, disper-

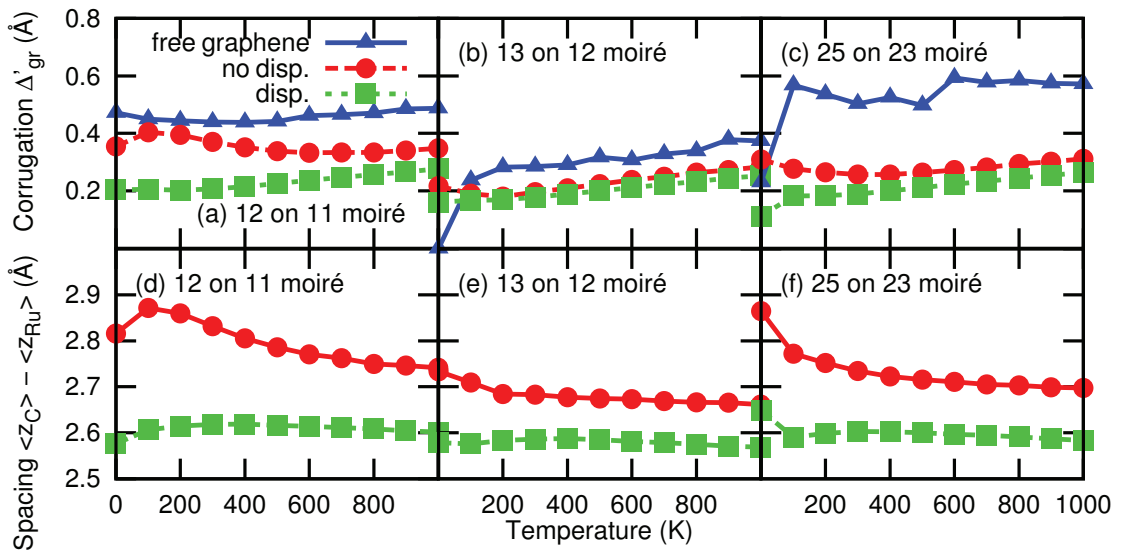


Figure 4.9: Graphene corrugation  $\Delta'_{\text{gr}}$  and graphene-Ru(0001) distance  $\langle z_{C,i} \rangle - \langle z_{\text{Ru},i} \rangle$  versus temperature for the three moiré structures computed with and without dispersion corrections. For comparison, the corrugation of free graphene having the same surface density as its epitaxial counterpart is also shown.

sion forces tend to flatten the graphene layer, and these effects remain at finite temperature. Interestingly we find that the lateral constraints imposed by the different moiré structures have little influence on the globally averaged graphene corrugation once thermal effects set in. These

constraints are better appreciated by looking at the corrugation amplitude for the free graphene layer kept under the same surface density as in the corresponding moiré. Except sometimes at 0 K, these monolayers are always more corrugated than epitaxial graphene, which is consistent with the larger corrugation experienced by graphene lesser bound to the metal in absence of dispersion forces.

Comparing the different moiré structures also gives insight into the respective effects of size and strain: the 12 on 11 and 13 on 12 moirés have primitive cells with similar sizes, but the graphene layer experiences strain ratios of 0.9938 and 1.0007, respectively. The 25 on 23 moiré is about four times larger, but also undergoes some strain (by a factor of 0.9974). Due to the high inplane stiffness of graphene [169], the resulting differences in strain are large enough to influence the corrugation significantly. The tensile strain on graphene in the 13 on 12 simulation cell reduces its corrugation in all three cases. In the 12 on 11 moiré, compressive strain has an opposite effect on this observable and in the case of epitaxial graphene in the 25 on 23 structure, the intermediate strain leads to intermediate corrugations. Only for free graphene in the largest simulation cell does the size effect dominate, with a slightly larger corrugation as the one found for the two smaller free graphene sheets.

For a more thorough distinction between the effect of size and strain on the corrugation of graphene, simulations on freestanding graphene with  $12 \times 12$  unit cells and  $13 \times 13$  unit cells have been carried out at surface densities matching those of epitaxial graphene in the 12 on 11 and 13 on 12 moirés. From Fig. 4.10, increasing the size of the graphene sheet is seen to also increase the corrugation, as expected. However, this effect is rather limited in comparison to the effect of the density difference between the 12 on 11 and 13 on 12 simulation boxes. The slightly compressive strain (or higher density) in the 12 on 11 box induces a higher corrugation as the tensile strain in the 13 on 12 box, especially at low temperatures. This confirms the interpretation of Fig. 4.9(a-c) above.

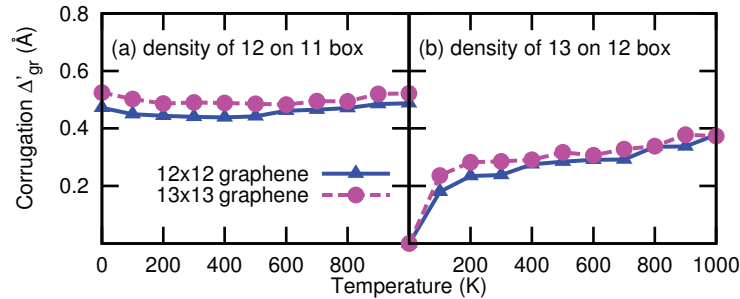


Figure 4.10: Corrugation of freestanding graphene as a function of temperature for the two system sizes of  $12 \times 12$  and  $13 \times 13$  unit cells. The calculations have been carried out in simulation cells that impose the same surface density as in epitaxial graphene in the 12 on 11 and 13 on 12 moiré structures. This allows to discriminate between the effect of size and strain on the corrugation of graphene.

In addition to the corrugation of the graphene layer, its distance to the metal can be evaluated from the MD trajectories. The thermally and spatially averaged separation between the graphene and uppermost metal layers are shown in panels (d-f) of Fig. 4.9. As expected, the additional dispersion corrections pull the graphene layer closer to the metal surface by a fraction of an Angström. As was the case for the intrinsic graphene corrugation, no significant dependence on the moiré structure is found in presence of dispersion corrections, the distance between the graphene and uppermost metal layers remaining close to 2.6 Å. However, when the graphene layer is weakly bound without dispersion forces, its average distance to the metal

surface mainly decreases with increasing temperature, which suggests that graphene better accommodates with the metal surface under thermal excitations.

This assumption is supported by looking at the corrugation of the uppermost layer of the Ru(0001) substrate. Using the definition used in the DFT calculations quoted in Table 4.3, significant values in excess of 0.3 Å and 0.6 Å are obtained at 300 K and 1000 K, respectively, independently of the moiré size and possible account of dispersion forces. These larger values with respect to the static calculations mentioned in Table 4.3 are better compatible with experimental measurements, which again emphasizes the importance of thermal effects on such structural observables.

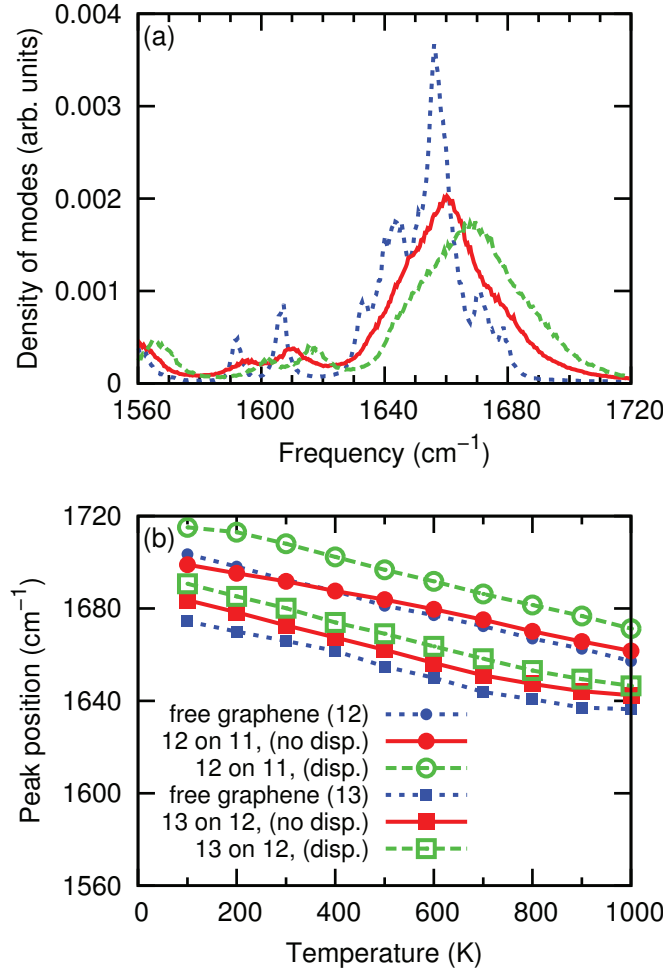


Figure 4.11: (a) Vibrational spectra of freestanding graphene and epitaxial graphene on Ru(0001) in the 13 on 12 moiré at 500 K, as obtained from simulations with and without screened dispersion corrections; (b) Frequency of the graphene G peak as a function of temperature for the 13 on 12 and the 12 on 11 moirés, calculated with and without screened dispersion corrections. For comparison, the G peak frequencies of free graphene layers having the same surface densities as their epitaxial counterparts are also shown.

**Vibrational properties** MD also provides a suitable framework for accessing vibrational properties in anharmonic regimes. Raman spectroscopy has notably been widely employed to study graphene and even to count the number of graphene layers on a substrate and to gauge their quality or the amount of strain [169, 171, 232]. In addition, Raman spectra can be further processed to give insight into thermomechanical properties such as the TEC [178]. Unfortu-

nately, the present BOP model lacks electrostatic components and cannot be used to simulate infrared or Raman intensities directly. Despite these limitations, the entire vibrational spectrum can be determined by Fourier transformation of the velocity time autocorrelation function, enabling a possible correspondence with experimental measurements for specific bands.

Vibrational spectra have been evaluated in the 100–1000 K temperature range for epitaxial graphene in the 13 on 12 and 12 on 11 moirés, with and without screened dispersion interactions and for the free graphene layers experiencing the compressive and tensile strains at the same surface densities. Typical spectra obtained for graphene in the 13 on 12 moiré at 500 K have been depicted in Fig. 4.11(a) in the specific spectral range covering 1560–1720  $\text{cm}^{-1}$  that corresponds to the Raman G band of graphite [170]. Compared with the results obtained for the free graphene layer, the interaction with the metal broadens the peak and shifts it to higher frequencies, especially when dispersion is taken into account. This compares well to experiments, where a blueshift of the G peak has been observed for GOM with respect to freestanding graphene [160]. The temperature dependence of the peak position in this range is shown in Fig. 4.11(b) for the six situations considered. In all cases, anharmonicities are manifested by a linearly increasing redshift with a slope in the range of  $-0.041$ – $-0.053 \text{ cm}^{-1}\text{K}^{-1}$ . Comparable slopes have been observed in experiments on pure graphene [176].

Strain effects are better seen on the overall peak position, rather than its dependence on temperature. Graphene layers experiencing compressive strain as in the 12 on 11 moiré exhibit a blueshift, while tensile strain leads to redshift. Size effects have also been quantified by repeating these simulations for the 25 on 23 moiré, but no difference was noted (data not shown). Changes in the peak positions in Fig. 4.11 are thus the result of strain effects rather than minor variations in system size. The difference in compressive strain between the 13 on 12 and the 12 on 11 moiré structures amounts to 0.69% in favor of the latter, which is fully consistent with recent Raman spectroscopy measurements on graphene where redshifts of the G peak of  $70 \pm 3 \text{ cm}^{-1}$  per percent of strain were reported [172]. It is also noteworthy that in both cases, binding to the substrate leads to an additional blueshift of the G peak, especially prominent when dispersion interactions are included. This intuitive effect further confirms that Raman spectroscopy could also be used to unravel the nature of the graphene-metal interaction in some of its intimate details.

#### 4.4.2.3 Ru NPs on graphene/Ru(0001)

Finally we have considered the thermal stability of Ru NPs on epitaxial graphene on Ru(0001) under the 12 on 11 configuration. In contrast with the graphite substrate, which is able to accommodate NPs of arbitrary size, the relatively restricted spatial extension of the moiré structures makes it more relevant to focus on small NPs of dimensions not larger than the moiré lattice. Here we have chosen to focus on  $\text{Ru}_{38}$  as a realistic example. In a first series of MD simulations of the soft-landing type, the adsorbate was initially placed at the low fcc moiré registry [201] and locally optimized, as depicted in Fig. 4.13(a). The system was subsequently simulated at increasing substrate temperatures, and the same two Lindemann indices  $\delta_{\text{intra}}$  and  $\delta_{\text{inter}}$  already introduced for adsorbates on graphite were calculated to characterize the internal state of the cluster and its overall motion on the corrugated substrate. Likewise the asphericity index was evaluated to determine possible shape transformations during the heating process.

Fig. 4.12 shows the variations of these observables as a function of temperature, as obtained from simulations carried without and with screened dispersion interactions. Without dispersion and at low temperatures, the diffusion of  $\text{Ru}_{38}$  on graphene/Ru(0001) is very similar to its diffusion on graphite, with the adsorbate moving freely without deforming over the substrate. A peak in  $\delta_{\text{inter}}$  near 300 K and the stabilization of this index to low values above 500 K

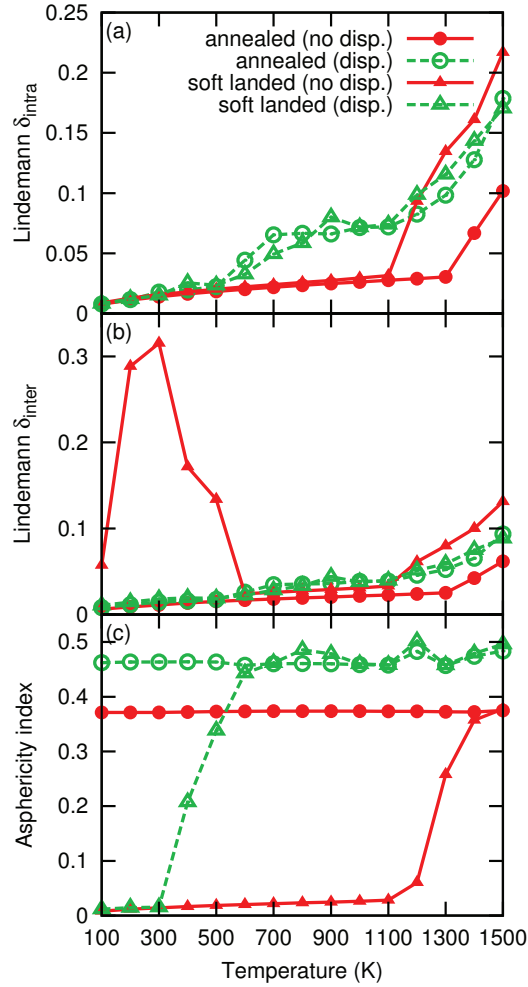


Figure 4.12: Thermal stability and shape of  $\text{Ru}_{38}$  on epitaxial graphene on  $\text{Ru}(0001)$ , as quantified by the Lindemann indices (a)  $\delta_{\text{intra}}$ ; (b)  $\delta_{\text{inter}}$ ; and (c) the asphericity index. Triangles correspond to data for soft-landed configurations, circles correspond to simulations restarted from previously annealed structures. The results are shown for the BOP model with (dashed lines) and without (solid lines) screened dispersion corrections.

shows that the adsorbate finds a more stable position closer to the substrate than in its initial deposition site. However, the truncated octahedral structure remains stable up to about 1300 K, above which the cluster reorganizes and flattens.

In the simulations including dispersion, the trajectories spontaneously converge to a more stable minimum already at low temperature and above 300 K the cluster isomerizes into a lower-energy, flatter structure with only three layers instead of four as in the initially deposited truncated octahedron. Having found lower energy minima, the configurations from the MD trajectories were systematically minimized for both models and the simulations were restarted from these annealed structures depicted in Fig. 4.13(b). These additional MD simulations closely resemble the experimental situations in which the clusters are grown *in situ* from the atomic vapor [19]. As expected, the annealed structures appear much more stable over the entire temperature range, and even rather robust against global diffusion on the substrate. The NPs also remain rigid and only exhibit some minor fluxionality in presence of dispersion forces above 700 K, before melting takes place above 1300 K. With dispersion interactions, the NP

displays lesser mobility and becomes fluxional only at the highest temperatures considered here, suggesting less rugged energy landscapes and higher isomerization barriers.

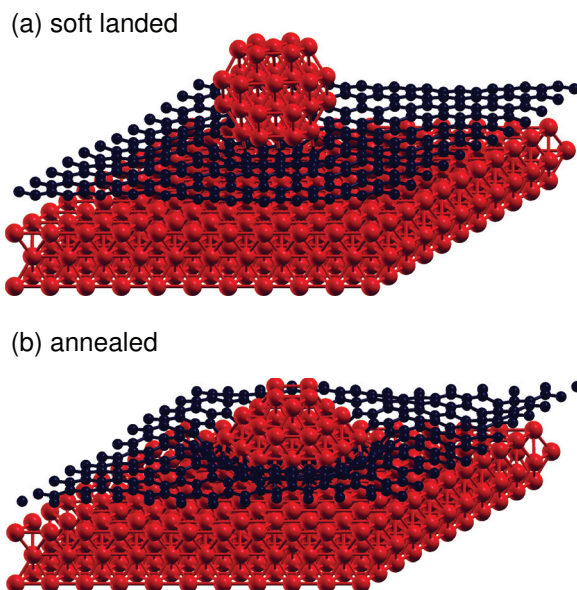


Figure 4.13: Low-energy structures of the Ru<sub>38</sub> NP on epitaxial graphene on Ru(0001) in the 12 on 11 moiré template. (a) Truncated octahedral minimum obtained assuming soft-landing and global migration to the most stable (fcc) registry; (b) Flatter minimum obtained by annealing the high-temperature MD trajectories.

Compared to the flat graphite substrate, Ru NPs deposited on epitaxial graphene are thermally much more stable. When dispersion forces are included, this greater stability can be traced back to the greater dispersion coefficients between metal atoms. However, even in absence of dispersion the particles show much less mobility, which we attribute to the moiré effect and the corrugation of the graphene layer that increases its contact surface with the particle and binds it more efficiently. Another contribution to the higher stability of the NPs on epitaxial graphene relative to graphite that was proposed based on electronic structure calculations [56] is the local change of hybridization of the carbon atoms sandwiched between the bulk metal substrate and the deposited NP. Although the present model does not explicitly quantify hybridization levels, a similar behavior is obtained here, as supported by the three-dimensional structure of the locally optimized configuration represented in Fig. 4.13. Moiré structures of graphene on metal have also already been used experimentally as substrates for metallic nanoclusters [19, 37, 233, 234]. Detailed electronic structure calculations gave insight into geometries of the adsorbates and their binding energy at several sites [19, 233, 234].

## 4.5 Conclusions

We have parametrized the Brenner BOP for the Ru-C system on several geometries obtained at DFT level for epitaxial graphene and small adsorbates thereon. Similarly to the previous chapter a dispersion correction has been added to the force field. However, here we kept the focus on the Brenner BOP that models the metallic and covalent interactions in the Ru-C system in order to assess in detail the qualities of the parametrization. Because graphene

interacts via chemisorption with the Ru(0001) surface, the dispersion description is only a correction though a significant one.

The Ru-C BOP has been employed successfully in local structure optimizations of epitaxial graphene, which allowed for comparison with a number of DFT data. The potential is also able to describe this system well at finite temperature, as shown e.g. from the analysis of the vibrational spectra of epitaxial graphene. In particular, the G peak in the spectrum reacted to temperature and strain in the way it was expected from experimental data, which shows that the BOP parametrization is able to correctly capture some of the anharmonicities of the potential energy surface. Limitations of the Ru-C BOP could be identified in the description of small clusters in contact with graphene as in these situations charge transfer may occur, which could not be modeled explicitly by the BOP. In these situations, the adsorption energies are underestimated with the BOP. However, for larger adsorbates on graphite and epitaxial graphene, the expected thermal behavior is recovered.



# Chapter 5

## Other transition metal–carbon systems

Epitaxial graphene on Ir(111) and Ni(111) are other examples of weakly and strongly interacting systems, respectively, that we discuss in this chapter. In the case of Ni, we consider also metallic nanoclusters deposited onto graphene and epitaxial graphene on the same metal. However, the investigation on these two systems was carried out in less detail. In the case of Ir–C, we present a Brenner BOP that has been parametrized on vdW-DF data of epitaxial graphene on Ir(111) [235, 236]. Discussing the qualities of this parametrization in the following section, it becomes clear that it is less reliable compared to the Ru–C Brenner BOP parametrization presented in chapter 4.

For the Ni–C system, we employed a TB model built on a minimal basis, including the  $s$  and  $p$  electrons of carbon and the  $d$  electrons of nickel [237]. This model has already been successfully employed for studying the growth of epitaxial graphene on Ni(111) [237–240] or for simulating the nucleation of carbon nanotubes on Ni NPs [241]. A dispersion correction was not applied in combination with the Ni–C covalent potential, because the interaction of graphene with Ni(111) is very strong and chemical bonding clearly dominates [242]. In addition, dispersion forces are expected to be smaller as for the other transition metals discussed in this work since Ni has with 28 the lowest number of electrons and is the only transition metal from the fourth period we considered.

### 5.1 Iridium–Carbon systems

Similarly to platinum, graphene binds only weakly to iridium surfaces [243], which explains the observation of several rotational domains [127, 183, 244]. The lattice parameter mismatch between graphene and Ir depends on temperature as the two materials have different TECs: The TEC of Ir is positive and the one of graphene possibly negative, but at least considerably smaller than the one of Ir. Instead of building up strain, graphene on Ir(111) slides, changing the moiré structure from a 21 on 19 commensurability at low temperature to a commensurability of 10 on 9 at high temperature [245]. We attempt to model this system with the help of a Brenner BOP in MD simulations at finite temperature. To our best knowledge, a parameter set for Ir–C of the Brenner BOP is not available in the literature, which makes a custom parametrization necessary. How it was obtained is described in the following section.

#### 5.1.1 Brenner BOP Ir–C parametrization

The carbon-carbon interactions were again described by the Brenner potential with the parameters taken from Table III of the original publication [101], neglecting the overbinding terms for radicals. The corresponding parameters are reproduced in Table 5.1. The iridium-iridium

interactions are described by the TB-SMA potential, which has been parametrized for a number of transition metals by Cleri and Rosato [94]. They adjusted the parameters in order to reproduce experimental data on lattice constants, cohesive energies and elastic constants. In the derivation of the binding energy, only first neighbor interactions are taken into account [see Eq. (2.1)–(2.2)]. Nonetheless, Cleri and Rosato report improvements on the finite temperature behavior when interactions up to fifth neighbors are included into the total cohesive energy. Especially in the case of a too short cut-off, the melting temperature might be decreased due to the atoms being able to escape the interaction sphere too easily. The distance to the fifth neighbor shell in fcc iridium is  $a_{\text{Ir}}/\sqrt{2} \cdot \sqrt{5} \approx 6.1 \text{ \AA}$ , with  $a_{\text{Ir}} = 3.839 \text{ \AA}$  its lattice constant [94]. For computational efficiency, we have opted for a cut-off at 5.0–5.3  $\text{\AA}$  which falls between the third and fourth neighbor shell. Using Eqn. (2.19)–(2.26), we have obtained the values for the Brenner parameter set for pure iridium, as shown in the first column of Table 5.1.

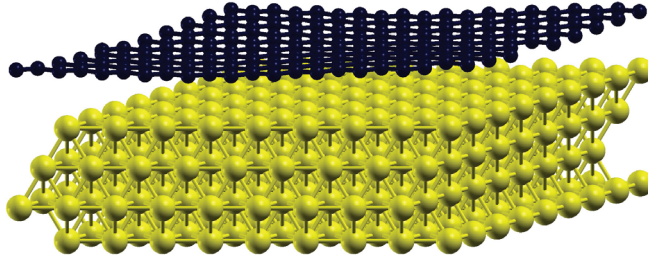


Figure 5.1: Locally optimized 10 on 9 moiré geometry of epitaxial graphene on Ir(111) as calculated with the vdW-DF by Atodiresei [235, 236].

To our best knowledge, no Brenner BOP parametrization for the interaction of carbon and iridium is available in the literature. Using the PTMC procedure presented in chapter 2, we adjusted a set of Brenner parameters for Ir-C by optimizing an error function that contained data of a relaxed geometry of epitaxial graphene on Ir(111) obtained at vdW-DF level [235]. This geometry, as depicted in Fig. 5.1, corresponds to a 10 on 9 moiré and contains four Ir(111) layers with 81 atoms each and an epitaxial graphene layer of  $10 \times 10$  unit cell with a total of 200 carbon atoms. In a first attempt, the Grimme D2 dispersion correction was added to the Brenner BOP trial potentials during the parameter optimization. However, it turns out that the non-bonding adsorption energy of the graphene layer as calculated with the Grimme D2 correction exceeds the total adsorption energy as calculated in the reference vdW-DF calculation. This shows that dispersion interactions calculated by Grimme D2 are stronger as compared to interactions obtained by the vdW-DF at least in the context of epitaxial graphene.

Due to these difficulties, the parameter adjustment was carried out in a second attempt without the dispersion correction coupled to the trial Ir-C Brenner BOP potentials. In order to capture at least some of the dispersion interaction, the range of the Brenner BOP potential was increased to at least up to 4.0–4.3  $\text{\AA}$  during the parameter adjustment. The error function Eq. (2.27) was computed on the basis of the sum of the square gradient components of the relaxed vdW-DF geometry as calculated with the trial parameter sets and the interaction energy of the graphene layer. The weighting factor  $\rho$  in Eq. (2.27) was used to assign a relative weight of 20 to the reproduction of the graphene interaction energy. Two subsequent PTMC optimizations with 24 replicas were performed with  $10^6$  cycles each.

In a second step of the parameter optimization, the Levenberg-Marquardt algorithm was employed to search for a precise minimum of the error function close to the best performing trial parameter set obtained by the PTMC procedure. For this last step the error function was refined: local geometry relaxations were carried out at each optimization step and the target

	Ir-Ir	Ir-C	C-C
$S$	6.3099	330.9142	1.22
$\beta$ ( $\text{\AA}^{-1}$ )	1.7608	1.2956	2.1
$D_0$ (eV)	4.7783	0.1958	6
$r_0$ ( $\text{\AA}$ )	2.4973	0.6574	1.39
$R^{(1)}$ ( $\text{\AA}$ )	5.0	4.047	1.7
$R^{(2)}$ ( $\text{\AA}$ )	5.3	4.463	2
	Ir-Ir-Ir and Ir-C-Ir	Ir-Ir-C and C-Ir-Ir	C-C-C and C-Ir-C
$\gamma$	1	0.1997	0.00020813
$c$	0	1376.4174	330
$d$	1	28.5070	3.5
$2\mu$ ( $\text{\AA}^{-1}$ )	1.9826	2.5605	0

Table 5.1: Pair-type dependent parameter set for the Brenner potential for iridium and carbon containing systems.

observables were changed to the properties listed in the first part of Table 5.2. The table gives these observables as obtained in the reference vdW-DF calculation by Atodiresei [235, 236] together with the data obtained with the Brenner BOP with the final Ir-C parameter set which is shown in Table 5.1. Dispersion interactions are implicitly included into the Brenner BOP with its large cut-off distance for Ir-C, because these interactions were also included in the reference data during the parameter optimization. Adding dispersion corrections would represent some sort of double counting of dispersion and degrades the rather satisfactory agreement with the vdW-DF reference data. However, it should be noted that the long-range character of dispersion is lost, which represents a major drawback of this approach.

The overall agreement with the reference data is satisfactory for these zero temperature properties. Only the deformation of the graphene layer is too large, which also translates to an excessive deformation energy. The graphene corrugation depends very sensibly on temperature and even more importantly on the strain imposed on the graphene layer not only by the contact with the substrate, but also by the common simulation box that is used for both subsystems. Unfortunately, these influences are not very well controlled in these calculations and subject the deformation of graphene to a rather high degree of uncertainty and systematic error. Despite the difficulties of administering the interdependent influences of strain and temperature on this observable, at least the analysis of their effect is attempted below. More important for the appreciation of the quality of the present Brenner BOP parametrization is probably the distance of the graphene layer from the metal surface and its adsorption energy. A graphene-metal spacing similar to the interlayer distance of graphite (3.36  $\text{\AA}$ ) points to a weak interaction dominated by dispersion forces, which is the case of the graphene/Ir(111) system as opposed to the graphene-metal spacing of strongly interacting systems such as graphene/Ru(0001) and graphene/Ni(111), which is of the order of 2.1  $\text{\AA}$  [188, 250] and therefore similar to the spacing of the (0001) or (111) metal layers.

The second part of Table 5.2 shows data from other DFT calculations. Busse and coworkers [246] locally relaxed the 10 on 9 graphene/Ir(111) moiré structure using GGA DFT-D where the Ir  $C_6$  dispersion coefficient was determined by comparing DFT-D and nonlocal vdW-DF calculations for adsorption geometries of benzene on Ir(111). The adsorption energy of graphene was then obtained via a full vdW-DF calculation of the structure obtained from DFT-D [246]. Using the PW91 GGA functional, N'Diaye and coworkers [19] found a comparatively very small

Method	$\Delta_{\text{gr}}$	$\Delta_{\text{Ir}}$	$\Delta_{\text{Ir,gr}}$	$\tilde{\Delta}_{\text{Ir,gr}}$	$E_{\text{int}}$	$E_{\text{ads}}$	$E_{\text{def}}$
Brenner BOP	0.72	0.03	3.07	3.41	-76.3	-64.6	11.59
vdW-DF [235, 236]	0.46	0.02	3.25	3.44	-72.3	-69.9	2.4
GGA DFT-D/vdW-DF [246]	0.35		3.27	3.41		-50	
PW91-GGA [19]	0.27	0.05	3.77			-2	
LDA [247]	0.6		3.25				
AFM at 4.7 K [248]	0.35±0.1						
SXRD at 300 K [236]	0.379±0.044	0.017±0.002		3.39±0.28			
EXRR at 300 K [236]				3.38±0.04			
LEED $I(V)$ model at 300 K [249]	0.47 ± 0.05		3.27				
STM at 300 K [183]	0.3						

Table 5.2: Properties of the epitaxial graphene on Ir(111) moiré structure (10 on 9 moiré, zero inplane angle). Data obtained in local structural relaxations with the present Brenner BOP parametrization and vdW-DF reference data [235, 236] that have been used for its parametrization. The middle and lower parts of the table indicate DFT and experimental data of the system taken from the literature. The data include the corrugation of the graphene layer  $\Delta_{\text{gr}}$ , the corrugation of the uppermost iridium layer  $\Delta_{\text{Ir}}$ , the smallest separation between the graphene layer and the Ir(111) surface  $\Delta_{\text{Ir,gr}}$ , the average separation between the graphene layer and the Ir(111) surface  $\tilde{\Delta}_{\text{Ir,gr}}$ , the interaction energy of the graphene layer  $E_{\text{int}}$ , its adsorption energy  $E_{\text{ads}}$  and its deformation energy  $E_{\text{def}}$  which is defined as the energy necessary to deform a planar graphene sheet into the corrugated shape as in epitaxy with Ir(111). All distances and energies are given in Å and meV per carbon atom, respectively.

adsorption energy of the graphene of only 2 meV per carbon atom. The adsorption energy of graphene on Ir(111) (-69.9 meV per carbon atom [235]) can otherwise be compared to the one of graphene on Pt(111) (-43 meV per C atom [167]) or to the interlayer adhesion of graphite (-48 meV per C atom [119]) and is significantly below the value for graphene on Ru(0001) (-163 meV per C atom [67]). The indicated literature values are from the most detailed DFT calculations that we are aware of for the respective systems. Following the suggestion of Feibelman [56] that LDA calculations may lead to better results in the specific case of the Ir-graphene interaction, Knudsen and coworkers found with 0.6 Å a similar corrugation of the graphene layer as obtained with the present semi-empirical BOP.

Finally, in the lower part of Table 5.2, we have reproduced experimental data on this system. Using a variety of experimental techniques, such as AFM [248], SXRD [236], extended x-ray reflectivity (EXRR) [236], LEED [249] and STM [183], some of the geometric properties of this moiré structure could be quantified. Apart from the AFM measurement all the data were obtained at room temperature and one could therefore expect that the corrugation of the graphene and topmost Ir(111) layer as well as the spacing of the graphene layer from the metal surface exceed the zero temperature values of the cited calculations. This temperature effect seems to be small yet the experimental data are comparable to those from DFT or the present Brenner BOP. With the BOP we have carried out MD simulations at finite temperature as presented below, which allows for some additional comparison with experiment.

In order to assess the transferability of the Brenner BOP, the energies per bond and nearest neighbor distances of the Ir-C diatomic and the Ir-C crystal in NaCl structure have been calculated. With the B3LYP functional a diatomic distance of 1.649 Å with a binding energy of 6.43 eV and a ground state vibrational frequency of 1166 cm<sup>-1</sup> have been reported [251], which contrasts with the values of only 0.2 eV at a separation of 0.657 Å and a vibrational frequency of 230 cm<sup>-1</sup> as predicted by the current BOP. Clearly, the performance of the BOP is poor in this situation which is rather different from the training set. We speculate that this is

due to the ionic character of the molecule ( $\text{Ir}^+\text{C}^-$ ), which can not be modeled explicitly by the BOP. Slightly better results are obtained for the stoichiometric IrC compound in NaCl crystal structure where the BOP predicts an energy per bond of 1.12 eV at a nearest neighbor distance of 1.93 Å which we compare to 2.28 eV/per bond at a nearest neighbor distance of 2.06 Å in the same structure, as obtained by *ab initio* linear-muffin-tin-orbitals total energy calculations [252]. These transferability problems are not unusual for semiempirical potentials [253], but are particularly pronounced for the present parametrization despite its capability of reasonably reproducing the training set. Particular caution should therefore be used when using the present Ir-C Brenner BOP in situations that are very different from graphene/Ir(111). A possible solution to these problems would be to attempt a new parameter adjustment of the BOP for Ir-C, but including a dispersion correction that could be adjusted jointly with the BOP. If the screened dispersion model of Eq. 2.47 was used, this would mean to add the screening length  $r_{\text{TF}}$  to the adjustable parameters of the force field.

### 5.1.2 Geometry of epitaxial graphene on Ir(111)

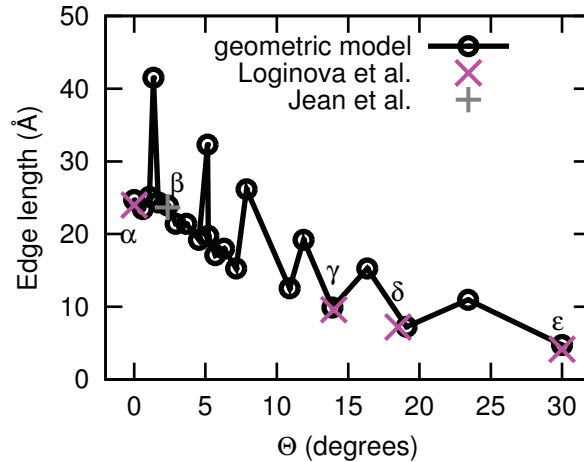


Figure 5.2: Edge length of the graphene/Ir(111) moiré as a function of the inplane angle  $\Theta$  between the graphene and metal lattices obtained by a purely geometric model. Experimental data from Loginova and coworkers [183] and Jean and coworkers [254] are superimposed. We have designated the experimental structures by  $\alpha$ ,  $\beta$ ,  $\gamma$ ,  $\delta$  and  $\varepsilon$ .

Before applying the Ir-C BOP in MD simulations on epitaxial graphene on Ir(111) at finite temperature, we investigate on possible inplane angles that produce commensurate moiré structures of graphene/Ir(111). For this purpose, the algorithm introduced in chapter 2.6 is employed for the 10 on 9 commensurability of graphene/Ir(111). Fig. 5.2 shows the size of the moiré unit cell as a function of the inplane angle between the graphene lattice and the triangular lattice at the Ir(111) surface. The figure also shows moiré structures that have been observed experimentally [183, 254], designated by  $\alpha$ ,  $\beta$ ,  $\gamma$ ,  $\delta$  and  $\varepsilon$ , which can be identified with the  $(10 \times 10)\text{R}0.00^\circ$ , the  $(\sqrt{93} \times \sqrt{93})\text{R}38.95^\circ$ , the  $(4 \times 4)\text{R}0.00^\circ$ , the  $(3 \times 3)\text{R}0.00^\circ$  and the  $(2 \times 2)\text{R}0.00^\circ$  moiré structure in Wood’s notation with respect to graphene which have inplane angles  $\Theta$  of  $0.000^\circ$ ,  $2.362^\circ$ ,  $13.898^\circ$ ,  $19.107^\circ$  and  $30.000^\circ$ , respectively. The agreement between the experimentally identified commensurabilities with the geometries detected with our geometric procedure is striking. Some of the moiré structures ( $\alpha$ ,  $\beta$  and  $\gamma$ ) have been studied in more detail with the help of MD simulations at finite temperature.

In order to avoid finite size effects, several moiré unit cells have been simulated in the structures with non-zero inplane angle, so that the number of graphene unit cells was at least equal to the number of graphene unit cells in the structure without inplane angle, that is  $10 \times 10$ . In addition, lateral periodic boundaries were applied imposing a graphene lattice constant of  $2.467 \text{ \AA}$ , which has been adopted from the DFT calculations on which the Ir-C potential was parametrized [235]. The lattice constant of Ir is then determined by the particular moiré structure as the Ir lattice needs to fit into the same simulation box. Below the epitaxial graphene layer, three Ir(111) layers were included explicitly, while the downmost layer has been kept fixed during the simulations. In a first step, the geometries were optimized locally before using them as initial configuration for MD simulations that employed a 1 fs time step and were propagated over 1.5 ns, with the first 0.5 ns disregarded as equilibration period. Using a Nosé-Hoover thermostat, the simulations were performed in the canonical ensemble. The thermostat was applied to the metal part of the substrate.

### 5.1.3 Effect of temperature on graphene/Ir(111)

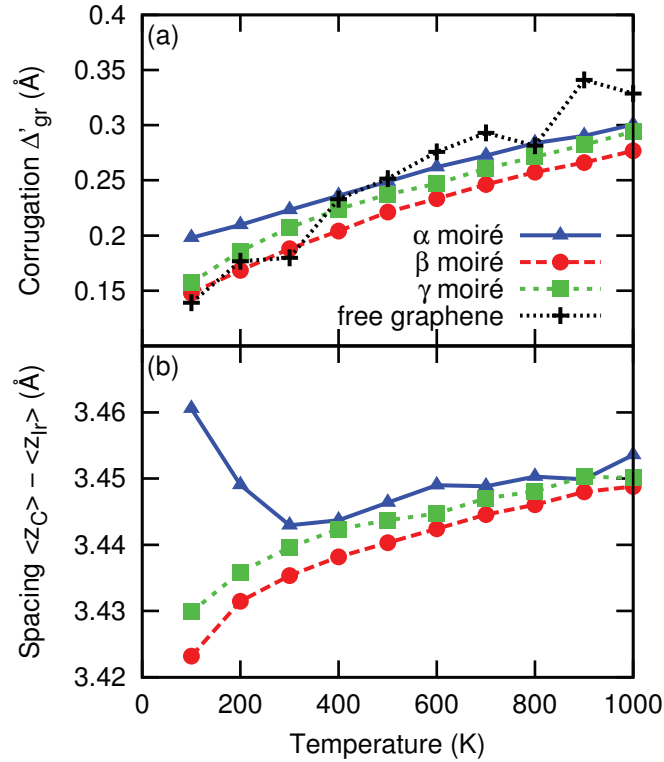


Figure 5.3: Graphene corrugation  $\Delta'_{gr}$  and graphene-Ir(111) distance  $\langle z_{C,i} \rangle - \langle z_{Ir,i} \rangle$  versus temperature for the case of aligned lattices and twisted graphene. For comparison, the corrugation of free graphene is also shown.

During the simulations, the corrugation of the graphene layer was quantified by its standard deviation of the out of plane distance of individual atoms ( $\Delta'_{gr}$ ). In addition, the average spacing between the graphene layer and the Ir(111) ( $\langle z_{C,i} \rangle - \langle z_{Ir,i} \rangle$ ) surface was also monitored. Fig. 5.3 shows these observables as a function of temperature for the three graphene/Ir(111) moiré structure as well as the corrugation of a free graphene layer with a density at which all strain vanishes at 0 K. Contrary to epitaxial graphene on Ru(0001), the epitaxial contact with the Ir(111) does not flatten the graphene layer, which can be attributed to the very

weak interaction for graphene on Ir(111). However, temperature affects the corrugation of free graphene more than when the graphene is in contact with the Ir(111) surface. Regarding the graphene corrugation, the differences between the three moiré structures are small and most likely to be attributed to different strains exerted by the common simulation box. Size effects are probably not the origin since larger system sizes tend to increase the corrugation. However, the smallest system in terms of simulated C atoms (the  $\alpha$  structure) has the largest corrugation. Except for some anomaly for the  $\alpha$  structure, the distance of the graphene layer from the Ir(111) surface tends to increase slightly, yet this effect is rather negligible as the increase is only about 0.03 Å over a temperature range of 1000 K. Over the entire temperature range and for all the three moiré structures, the spacing of over 3 Å is a clear indicator for the physisorbed state of graphene on Ir.

In conclusion, despite the difficulties to include a dispersion correction for epitaxial graphene on Ir(111) into the newly parametrized Ir–C BOP, the potential is able to describe reasonably well graphene/Ir(111). This is also exactly the system that was included into the fitting database during parameter optimization. For systems departing from this geometry, especially when small Ir clusters are involved, the Ir–C BOP exhibits some transferability problems.

## 5.2 Nickel–Carbon systems

The lattice constants of graphene and the Ni(111) surface lattice are very similar, which leads to commensurate structures. In contrast to epitaxial graphene on most other transition metal surfaces, usually no moiré effect is observed for nickel [32]. Even though the adsorption energy of graphene on Ni(111) of 67 meV per carbon atom is in the range of physisorption, the electronic structure shows clear signs of chemisorption [255]. In particular, the nickel 3d and the graphene  $\pi$  bands are hybridized and a partial charge transfer of spin-polarized electrons from nickel to carbon has been identified using x-ray magnetic circular dichroism and spin-resolved photoemission measurements [256]. This spin-filtering effect induces a magnetic moment into the graphene layer and may incidentally have interesting applications in spintronic devices. Metal contacts (Ohmic or Schottky) are essential for graphene-based devices and in this respect the metallic behavior of epitaxial graphene is promising [242].

There are three high symmetry geometries of commensurate graphene/Ni(111): The hcp-fcc geometry, where the centers of the carbon rings in graphene are aligned with the topmost Ni(111) layer; the top-hcp geometry, where the carbon atoms sit on top of nickel atoms either from the first or the second Ni(111) layer; and the top-fcc geometry, where the atoms in the graphene layer are aligned with the atoms of either the first or the third Ni(111) layer. LEED measurements suggest that the top-fcc configuration is the most stable [250]. Furthermore, the authors observed a distance of  $2.11 \pm 0.07$  Å from the graphene layer, but with a slight difference in spacing of 0.05 Å for the two sublattices of graphene. Models of these three structures have been considered by several authors [250, 255, 257], however intermediate structures where the center of the carbon-carbon bonds are aligned with the first Ni(111) layer have also been proposed based on experimental data [258].

Janthon and coworkers carried out local structural optimizations of the top-fcc, the bridge-top and the hcp-fcc geometry using a number of van der Waals or dispersion-corrected functionals [68]. The authors found significant differences in the results concerning adsorption energy and the spacing of the graphene layer. On the basis of comparisons with experimental data, they concluded that the optB86b-vdW functional and Grimme dispersive corrections resulted in the best predictions [68]. Additional precise data for the graphene/Ni(111) system were reported by Mittendorfer and coworkers at the DFT random phase approximation (RPA) level

of theory [255]. Their calculations predict two potential energy minima for the graphene layer, namely one at 2.17 Å from the Ni surface with 67 meV per carbon atom and another at 3.3 Å bound by 60 meV/C atom. The minima were found in the top-fcc and the top-hcp structure, however the closer minimum to the metal surface was slightly deeper in the case of the top-fcc structure compared to the top-hcp structure. Despite a low adsorption energy, the electronic structure of graphene is strongly affected by the epitaxial contact in the case of the closer minimum. Furthermore, these results clearly showed that simple LDA or GGA/PBE calculations are not reliable for this system [255].

The solubility of carbon atoms in bulk nickel is higher than for the other transition metals (Pt, Ru and Ir) discussed in this thesis [259]. This means that at high temperature considerable amounts of carbon may dissolve into the nickel surface. Upon cooling the carbon tends to segregate to the surface again and form several layers of graphene depending on the amount of carbon available. The interaction strength of epitaxial graphene also depends on the amount of carbon present in the underlying bulk metal. It has been shown that higher carbon concentrations reduce the adsorption energy of graphene [240]. This makes the formation of epitaxial graphene/Ni(111) with non-zero inplane angles more likely, as it is a general trend that weaker interactions of epitaxial graphene layer promote the formation of different rotational domains [32, 240, 259]. Such domains have been observed in epitaxial graphene on Ni(111) using room temperature STM: Murata and coworkers identified two moiré structures of graphene/Ni with inplane angles of 6.4° and 23° [242].

The calculations cited above showed that the results often depend on the details of the corresponding models, which makes computationally highly intensive methods such as RPA necessary [255]. Unfortunately, with these calculations only local relaxations representing the usual situation at zero temperature can be carried out. We attempt to address the effect of temperature on these systems with the help of MC simulations based on a TB approach that we present in the following section.

### 5.2.1 Tight-binding within the fourth moment approximation

The calculations on the Ni-C system are carried out using the TB model of Amara and coworkers [237]. The method takes the electronic density of states up to the first four moments into account and is therefore referred to as fourth-moment approximation to the tight-binding model (TB-FMA). In comparison to the BOP model that has been used throughout the rest of this work, this TB approach has the advantage of being less empirical and therefore of higher predictive power. In addition, Los and coworkers [260] developed a particularly efficient implementation of the potential in the form of a MC code, so that the computational cost of this TB model is only one order of magnitude higher than the one for the TB-SMA potential. In the following, we give a brief description of the TB-FMA potential, more details, especially on the efficient implementation and the potential parameters, can be found in Refs [237, 260].

The basis set of atomic orbitals contains the 2s and 2p states of carbon as well as the d states of nickel and is written as  $|k, \lambda\rangle$  with  $k$  the atomic site and  $\lambda$  the orbital index, ( $\lambda = s, p_x, p_y, p_z, d_{xy}, d_{yz}, d_{zx}, d_{x^2-y^2}, d_{3z^2-r^2}$ ). Direct overlap integrals ( $\langle i, \lambda | j, \mu \rangle = \delta_{ij} \delta_{\lambda\mu}$ ) and three-center integrals are neglected. The Hamiltonian  $H$  takes the form of a matrix containing the hopping integrals  $\beta_{k\lambda, j\mu}$ :

$$\beta_{k\lambda, j\mu} = H_{k\lambda, j\mu} = \langle k, \lambda | H | j, \mu \rangle \text{ for } k \neq j, \quad (5.1)$$

which can be expressed as function of the Slater-Koster parameters [261]. The on-site elements are assumed to be equal to the atomic levels  $\varepsilon_{k\lambda}$ :  $H_{k\lambda, k\mu} = \varepsilon_{k\lambda} \delta_{\lambda\mu}$ . For carbon (nickel),  $\varepsilon_s$  and

$\varepsilon_p$  ( $\varepsilon_d$ ) had to be determined.

These considerations on the electronic structure can be used in the following atomistic description. The total energy is written as a sum over all atoms  $k$ , containing each an attractive term corresponding to the band energy  $E_{\text{band}}^k$  in the TB model and an empirical repulsive term  $E_{\text{rep}}^k$ :

$$E = \sum_k E_{\text{band}}^k + E_{\text{rep}}^k. \quad (5.2)$$

The band energy in turn is expressed as an integral over the local electronic density of states  $n_k(E)$ :

$$E_{\text{band}}^k = \int_{-\infty}^{\varepsilon_F} (E - \varepsilon_k) n_k(E) dE, \quad (5.3)$$

where  $\varepsilon_F$  denotes the Fermi energy and  $\varepsilon_k$  the energy of atomic level  $k$ . The total density of states is defined as

$$n(E) = \frac{2}{N} \sum_N \delta(E - E_n), \quad (5.4)$$

where  $N$  is the total number of atoms and the factor two has been introduced in order to account for spin degeneracy. The eigenvalues of the Hamiltonian matrix  $H$  are designated by  $E_n$ . Equivalently, the sum over the eigenvalues of  $H$  can be replaced by its trace:

$$n(E) = \frac{2}{N} \text{Tr} \delta(E \cdot \text{Id} - H), \quad (5.5)$$

where  $\text{Id}$  denotes the identity operator. Using  $\delta(z) = \lim_{\varepsilon \rightarrow 0^+} (-1/\pi \text{Im} [z + i\varepsilon]^{-1})$  as an expression for the Dirac delta distribution, and introducing the Green's function operator  $G(z) = (z \cdot \text{Id} - H)^{-1}$ , one can write:

$$n(E) = -\frac{2}{N\pi} \text{Tr} \lim_{\varepsilon \rightarrow 0^+} \text{Im} G(E \cdot \text{Id} + i\varepsilon) \quad (5.6)$$

The local density of states for orbital  $\lambda$  can be obtained by projecting  $G$  on  $|k\lambda\rangle$ :

$$n_{k,\lambda}(E) = -\frac{2}{\pi} \lim_{\varepsilon \rightarrow 0^+} \text{Im} G_{k\lambda,k\lambda}(E \cdot \text{Id} + i\varepsilon), \quad (5.7)$$

where  $G_{k\lambda,k\lambda}$  designates a diagonal element of the Green's function. These elements can be obtained using the recursive Lanczos tridiagonalization transformation, which allows to rewrite  $G_{k\lambda,k\lambda}$  as the following continuous fraction:

$$G_{k\lambda,k\lambda}(z) = \frac{1}{z - a_1^{k\lambda} - \frac{(b_1^{k\lambda})^2}{\dots - z - a_M^{k\lambda} - (b_M^{k\lambda})^2 \Sigma_M(z)}}, \quad (5.8)$$

where the coefficients  $a_i^{k\lambda}$  and  $b_i^{k\lambda} = (\beta_i^{k\lambda})^2$  correspond to the diagonal and the squares of the off-diagonal elements of the tridiagonal Hamiltonian matrix, respectively. These coefficients are also related to the moments of the electronic density of states. In the TB-FMA model, the coefficients up to  $M = 2$  are considered as they depend on moments lower or equal to the fourth. Higher order coefficients are taken to be equal to the ones of  $M = 2$ . This allows to find a particularly simple expression for the local density of states.

The repulsive part of the potential  $E_{\text{rep}}^k$  is expressed as a functional  $F$  of a repulsive pair

potential  $\phi$ :

$$E_{\text{rep}}^k = F \left[ \sum_{j \neq k} \phi(r_{jk}) \right] \quad (5.9)$$

where  $r_{jk}$  stands for the distance between atom  $j$  and  $k$ . In the case of carbon-carbon interactions, the functional takes the form of a fifth order polynomial and  $\phi$  the following pair form:

$$\phi(r) = \phi_0(d_0/r)^m \exp\{m[-(r/d_c)^{m_c} + (d_0/d_c)^{m_c}]\} \quad (5.10)$$

In the case of pure nickel or nickel-carbon repulsion, the pair potential  $E_{\text{rep}}^k$  takes the Born-Mayer form, similarly to the repulsive part of the TB-SMA potential. The parameters were adjusted in order to reproduce certain reference data. In the case of carbon, these data are obtained from *ab initio* full potential linearized muffintin orbital calculations on a  $C_3$  linear molecule, an infinite linear chain, a graphene sheet, diamond, simple cubic, and facecentered-cubic structures [237]. In the case of pure Ni, the data correspond to the experimental values of the lattice parameter, of the cohesive energy, and of the elastic moduli [237]. Finally, the parameters for the repulsive term of the Ni-C interactions were adjusted to *ab initio* data (lattice constant, bulk modulus and enthalpy of formation) of the hypothetical NaCl structures [237].

## 5.2.2 Simulation details

The TB model described above has already been successfully employed in grand canonical MC simulations on the growth of epitaxial graphene on Ni(111) [237], the catalytic nucleation of carbon nanotubes [237] or the diffusion mechanism of Ni NPs on graphene [260]. Using the same model, the growth mechanism of graphene on Ni(111) has been identified to follow the sequential addition of C-hexagons, which leads to a defect-free graphene adlayer [239]. Furthermore, it turns out that defects in the graphene layer heal at faster rates thanks to the epitaxial contact with a Ni(111) surface [238]. The Ni(111) surface acts as a catalyst for the formation of graphene and up to a certain hydrocarbon pressure leading to a self limiting growth [240]. The epitaxial graphene layer in turn leads to a depletion of carbon atoms between the uppermost two Ni(111) layers. When the hydrocarbon pressure is further increased, the interaction strength of epitaxial graphene diminishes and eventually additional graphene layers may form. In the regime of high hydrocarbon pressures where the interaction with the Ni(111) is reduced, the likelihood of the formation of twisted graphene increases [240].

We use MC simulations in the canonical ensemble in order to assess the effect of temperature of epitaxial graphene on Ni(111) as well as the thermal stability of Ni adsorbates on freestanding graphene as compared to graphene/Ni(111). During all calculations, rectangular periodic boundary conditions were applied, with a simulation box size that was adjusted to fit the graphene layer without producing any strain at zero temperature. The graphene layer consisted of  $10 \times 10$  unit cells containing two carbon atoms each. In the case of epitaxial graphene three additional Ni(111) layers with 100 Ni atoms each were taken into account, with the downmost layer being kept fixed. For the simulations at finite temperature, a total of  $10^5$  MC sweeps (over each atom) were carried out while the first  $4 \times 10^4$  sweeps were disregarded as equilibration steps.

## 5.2.3 Epitaxial graphene on Ni(111)

In agreement with the above mentioned DFT-RPA calculations [255], the TB-FMA model for Ni-C predicts that the top-fcc geometry of the graphene/Ni(111) is the most stable structure [257]. Therefore the MC simulations at finite temperature have been based on this geom-

etry. In addition, we considered a graphene/Ni(111) geometry with an inplane angle of  $15.2^\circ$ . This structure contained four moiré unit cells each with 43 graphene unit cells and therefore a total of 344 C atoms, as compared to the graphene/Ni(111) geometry with zero inplane angle with 200 C atoms. In contrast to the other moirés of epitaxial graphene, the commensurability of the zero inplane structure of graphene/Ni(111) allows to construct geometries of non-zero inplane angle with the same almost vanishing strain. This makes the results on the aligned structure more comparable to the ones with twisted graphene, since no additional effect of strain comes into play. However, the system size may still have an effect, but it turned to be rather small in similar systems (see Fig. 4.10).

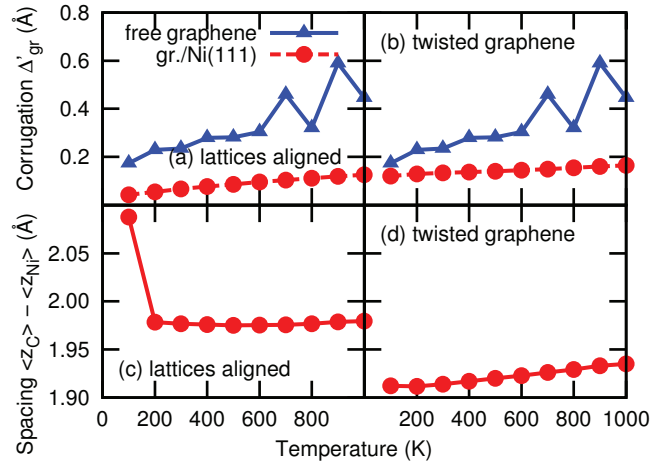


Figure 5.4: Graphene corrugation  $\Delta'_{gr}$  and graphene-Ni(111) distance  $\langle z_{C,i} \rangle - \langle z_{Ni,i} \rangle$  versus temperature for the case of aligned lattices (no moiré) and twisted graphene (moiré effect) for graphene/Ni(111). For comparison, the corrugation of free graphene with the same density is also shown (also calculated with the TB-FMA model).

During the simulations, the corrugation of the graphene layer defined as the standard deviation of the distance of the carbon atoms perpendicular to the plane of the layer was monitored as well as the average spacing of the graphene from the Ni(111) surface. The data concerning the geometry with zero inplane angle as well as the structure with an inplane angle of  $15.2^\circ$  are shown in Fig. 5.4. For comparison, the figure shows also the corrugation of a free graphene sheet with the same surface density. The epitaxial contact with Ni(111) appears to decrease the corrugation of the graphene significantly for both the aligned and twisted structures, and does not vary significantly with temperature. This is similar to the prediction that we previously obtained for graphene/Ru(0001). In addition, the spacing between the graphene layer and the Ni(111) surface depends little on temperature up to 1000 K and is for both of the structures close to 2 Å. Compared to the aligned structure, it seems though that the spacing in the case of twisted graphene is slightly reduced while its corrugation is increased, especially at low temperature. The main goal of this calculation was to find out about the effect of temperature on these two observables of epitaxial graphene on Ni(111), and it seems that it is fairly low up to 1000 K. This could indicate that the detailed calculations carried out at RPA level at zero temperature [255] can be compared directly to experimental data obtained at finite temperature.

### 5.2.4 Ni adsorbates on free and epitaxial graphene

The TB-FMA model for Ni-C was next applied to Ni NPs in contact with graphene either in its freestanding form or in epitaxy on Ni(111), *i.e.* using the system discussed above as a substrate. Supported Ni NPs on graphite may be produced experimentally with a narrow size distribution, which may be useful for the investigation on their size-dependant magnetic properties or for the catalysis for the size-selective growth of other nanomaterials [262]. It has also been shown that Ni NPs may destroy Ni supported graphene [263], most likely because the adsorbates increase the graphene-Ni(111) interaction significantly [264]. This process may find future applications in the production of nanopatterned substrates where Ni adsorbates could be used to introduce holes into the graphene layer.

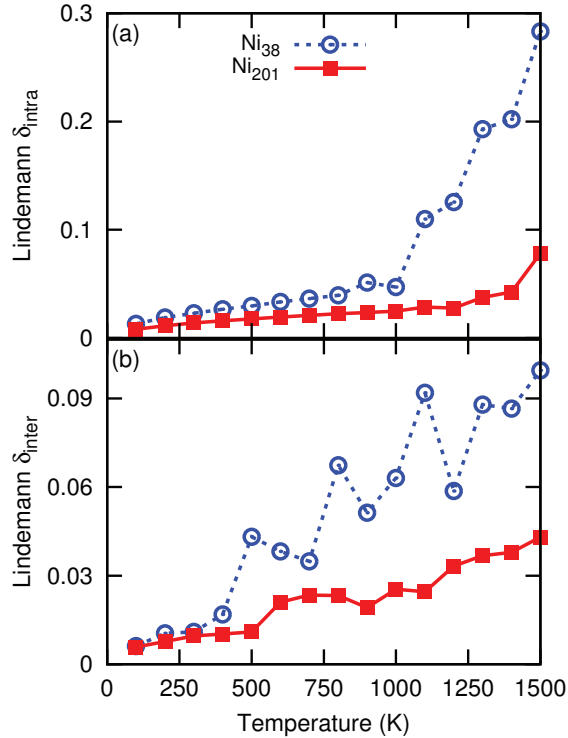


Figure 5.5: Thermal stability of  $\text{Ni}_{38}$  and  $\text{Ni}_{201}$  on graphene, quantified by (a)  $\delta_{\text{intra}}$ ; (b)  $\delta_{\text{inter}}$ , as obtained from MC simulations using the TB-FMA model for Ni-C.

MC simulations using the TB-FMA model above have been carried out on Ni NPs deposited on graphene. The two Wulff sizes of 38 and 201 atoms with truncated octahedral shapes were considered. The internal thermal stability of the adsorbates and their stability on the graphene surface has been monitored by the Lindemann indices  $\delta_{\text{intra}}$  and  $\delta_{\text{inter}}$  as defined in Eqn. (2.61) and (2.62), respectively. Fig. 5.5 shows these observables as a function of temperature for the two adsorbate sizes.

As suggested by the comparatively low values of  $\delta_{\text{inter}}$ , the center of mass of both NPs does not move significantly relative to graphene over the entire temperature range up to 1500 K. The larger adsorbate remains also internally relatively rigid, whereas the smaller  $\text{Ni}_{38}$  cluster reorganizes into a two-layer shape as the temperature exceeds about 1000 K. Fig. 5.6 shows the initial and final geometries of the  $\text{Ni}_{38}$  and the  $\text{Ni}_{201}$  on graphene for the MC simulations at 1500 K.

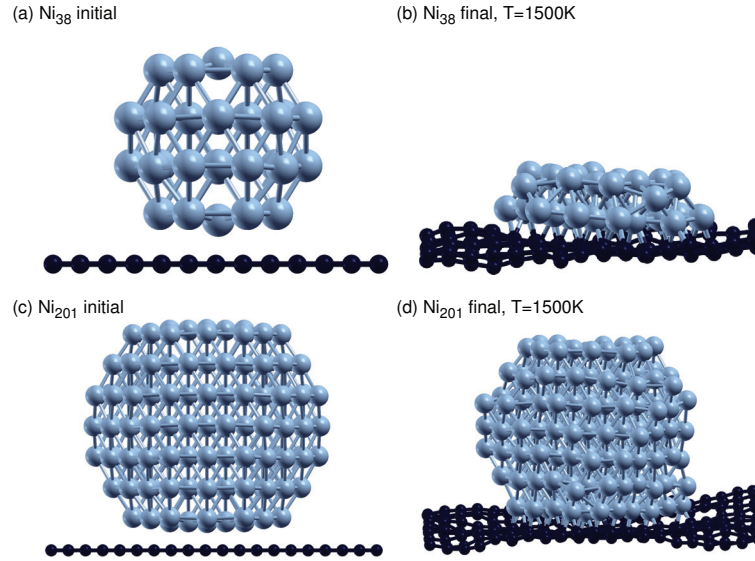


Figure 5.6: MC snapshots of truncated octahedral Ni NPs on graphene. (a) initial geometry of Ni<sub>38</sub> on graphene, (b) final geometry of Ni<sub>38</sub> on graphene at 1500 K, (c) initial geometry of Ni<sub>201</sub> on graphene, (d) final geometry of Ni<sub>201</sub> on graphene at 1500 K.

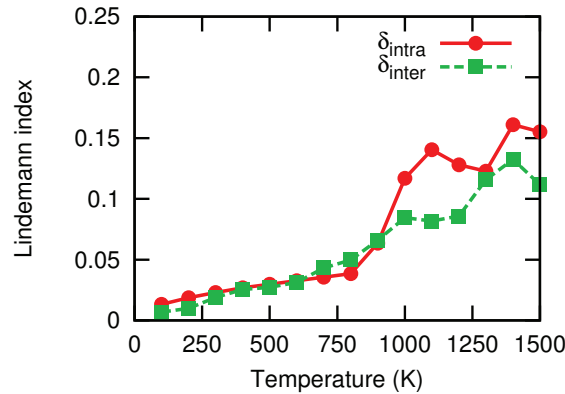


Figure 5.7: Thermal stability of the Ni<sub>38</sub> cluster deposited on epitaxial graphene on Ni(111), as quantified in the MC simulations by the Lindemann indices  $\delta_{\text{intra}}$  and  $\delta_{\text{inter}}$ .

These results are to be compared with Ni adsorbates on graphene/Ni(111). For this system, only the smaller adsorbate was examined. Fig. 5.7 shows the variation of the two Lindemann indices with temperature. Both of them show very similar trends. Comparing the stability of the cluster on graphene/Ni(111) to the previous case of bare graphene support, no major difference can be found. However, the internal stability of the cluster is enhanced with respect to the cluster on graphene. Nonetheless, the reorganization into a two-layer structure at around 1000 K still occurs. In conclusion, the alteration of the epitaxial graphene layer on Ni(111) by Ni adsorbates reported by Lahiri and Batzill [263] could not be reproduced. This might be due to too short simulation times, however a more detailed analysis in this direction would be useful as other experiments showed more interesting properties of Ni adsorbates interacting with epitaxial graphene on Ni: In particular, it has been shown that Ni NPs in contact with graphene have the property to act as a chemically driven knife that cuts graphene into ribbons or triangular patches. Furthermore, the cutting directions, along armchair or zigzag edges, are believed to be determined by the size of the NPs [265]. Although we did not seek to find

evidence for this particular mechanism here, it would be interesting to see whether the TB-FMA potential is able to model such processes.

# Chapter 6

## General conclusion

This work was concerned with nanopatterned moiré substrates of epitaxial graphene on transition metal surfaces. We have studied these materials as a support for the deposition of metallic clusters comparing their influence on the clusters to pure carbon substrates such as graphene and graphite. The research was carried on the basis of atomistic computer simulations of these systems at finite temperature. These simulations rely on the description of the atomic interactions, which have been modeled by means of bond-order potentials (BOPs). However, it turns out that dispersion forces influence significantly the structure and dynamics of epitaxial graphene on metal (GOM) and adsorbates thereon. Therefore, we added a Grimme style dispersion correction [76], commonly used in combination with DFT calculations, to the semi-empirical BOP. In terms of methodology, our contributions concern the development of a coarse-grained description of the dispersion forces in the case of semi-infinite layered substrates based on ideas of Steele [116]. Furthermore, for the modeling of Ru-C and Ir-C systems, we present parametrizations of the Brenner BOP [101] that describe the covalent and metallic interactions. Finally, these models have been successfully applied to the systems cited above. The effect of different versions of the dispersion correction was studied in detail at the example of Pt-C systems for which a Brenner BOP is available in the literature [96]. The work on Ru-C systems was more concerned with the description of the covalent and metallic interactions by the BOP, nonetheless dispersion corrections have been applied also for this type of systems. For both types of systems, Pt-C and Ru-C, the effect of temperature on epitaxial graphene and adsorbates on carbonaceous substrates has been studied revealing interesting diffusion mechanisms. Similar, yet less detailed calculations have also been carried out for Ir-C and Ni-C systems using a more precise TB model in the case of the latter. In the following, we recall the main ideas behind the coarse grained dispersion corrections, the most important properties of the BOP parametrizations and the principal results concerning GOM and metal adsorbates on carbonaceous substrates.

### Modeling dispersion in adsorption phenomena on semi-infinite substrates

London dispersion forces are an essential ingredient of sorption phenomena, and are expected to play a particularly important role for adsorbates on semi-infinite substrates. The contribution of long-range van der Waals attraction in DFT is one of the most active topics in this field, and to a large extent this issue is also problematic in atomistic simulations relying on explicit potentials that model the metallic and covalent parts of chemical bonding. We have addressed this issue in the case of transition metal NPs deposited on pure carbonaceous substrates such as graphene or graphite or epitaxial graphene on a bulk metal. This correction for a bulk

substrate is especially relevant for the non-covalent contribution to binding because the BOP ignores those contributions that lie beyond its cut-off. In the case of epitaxial graphene, the model was modified to account for possible screening effects that convey empirically the non-additive nature of the van der Waals interaction over an electronically delocalized bulk medium.

Our approach is similar to the explicit Grimme scheme that considers atom-atom van der Waals interactions that add up to the covalent and metallic part. However, in the same spirit as the Steele potential for substrate-atom interactions, we have also considered further the possibility of coarse-graining this long-range contribution by integrating them rigorously over the semi-infinite layered substrate.

The model was tested for platinum NPs on carbonaceous substrates and epitaxial graphene on Pt(111), using the BOP for the Pt-C system developed and parametrized by Albe and coworkers [96]. In the static limit for adsorption on graphite we find a good agreement between the explicit (Grimme D2) and coarse-grained implicit models for the adsorption energy of NPs containing up to several thousand atoms, and comparison with available DFT data for the smaller adsorbates is also satisfactory. When used at finite temperature with molecular dynamics (MD) simulations, the explicit and coarse-grained models exhibit some dissimilarities, with a stronger tendency for wetting in the latter case and less diffusion over the substrate. This behavior was interpreted as due to a slightly stronger physisorption in the implicit model, whereas interactions are neglected in the explicit approach beyond the simulation cell. The resulting difference between the models, which amounts to approximately 20 meV/atom in the adsorption energies, should obviously decrease in larger simulation supercells and bring the predictions of the explicit model closer to those of the coarse-grained model. The rate at which the two models converge would be worth investigating in the future, as it would also provide useful information for the DFT community about the importance of those corrections that are no longer minor once integrated over the (true) infinite substrate.

Some limitations in our modeling could be noted in the case of graphene, where for large adsorbed NPs the deformation of the carbon monolayer compromises the planar approximation employed in the integrated dispersion correction. Although large NPs deposited on pristine graphene may be more of academic interest, one possibly general way of addressing this issue could be to use the implicit model only beyond the simulation cell box, and keeping an atomistic description within it. Under such hybrid models, and as with other boundary problems in multiscale approaches the transition between the atomistic and coarse-grained contributions should be carefully chosen. In the case of bulk substrates, the implicit model seems to be generally valid, although ultimately the accuracy of its predictions should be evaluated against experiment rather than electronic structure calculations (especially those lacking screening), the underlying model being semi-empirical instead of *ab initio* based.

One immediate application of the coarse-grained model would be the determination of optimal shapes for NPs containing typically a hundred atoms and placed on the deformable carbonaceous substrate discussed in the present work. Global optimization would be useful notably for particles on epitaxial graphene, owing to promises in magnetic storage of such materials [4, 19, 47]. One other important application of the model could be to treat larger 2D assemblies of many adsorbates. At equilibrium, the stable patterns adopted by the assemblies should not only depend on the substrate (and the possible presence of a moiré nanomesh) but also on the adsorbate itself, as well as other external factors such as diffusion, adsorption or thermal desorption [15]. Long-range forces could also contribute to stabilizing the assemblies and should be incorporated in the model as well. Assemblies of NPs on surfaces could be described at a fully atomistic level, but also in a more global fashion by extracting the effective interactions between the NPs at finite temperature and plugging those into a coarse-grained model whose evolution is ruled e.g. by dissipative particle dynamics [266].

### Platinum-carbon systems

The model was used to describe epitaxial graphene on fcc platinum, and notably the moiré patterns that such two lattices produce when in contact with one another due to their incommensurability. In the case where the moiré is altered by some inplane angle, the geometric and finite temperature properties of those patterned substrates were found to depend non trivially on this angle. The corrugation of the graphene layer and its separation to the uppermost metal layer were found to be comparable to existing reference data, provided that the dispersion interactions are properly screened: An optimal screening length was evaluated to be as low as 2.9 Å. The vibrational spectra in the region of the Raman G peak of graphite, as obtained with a complete account of anharmonicities through the velocity time correlation function, were found to display also notable shifts and variations with temperature and the inplane angle. Those predictions, which should be amenable to comparison with experiment, highlight the importance of compressive or stretching strain exerted at the metal/carbon contact in the moiré pattern. Diffusion mechanisms on the graphite substrate were found to proceed via truncated Lévy flights, as previously identified in the literature [42, 155, 156].

The dynamics of Pt adsorbates on epitaxial graphene was also investigated and shown to be similar to that on graphite, again with sensible dynamical differences arising from the nature of the dispersion correction employed in the modeling. In particular, only the most realistic dispersion model that accounts for non-additive screening effects suggests that the graphene layer with the adsorbates should thermally desorb above 1000 K, the adsorbates being excessively pulled to the substrate in absence of screening.

It would also be worth extending the Pt-C model to treat additional hydrogen atoms, which would imply some further parametrization for terms involving hydrogen and platinum atoms (the Brenner model can be readily used for C-H atoms). Such an extension would pave the way to model hydrocarbon molecules on metal surfaces, for which the concerted effects of covalent and van der Waals forces have been discussed at length [267], including the specific issue of screening. It could then become necessary to account for charge transfer and polarisation effects more explicitly (at least those leading to the multipolar nature of the adsorbed molecules), which would also imply considering the possible effect of image charges.

### Ruthenium-carbon systems

We have developed an atomistic potential of the bond-order, Brenner-type family to simulate ruthenium NPs on epitaxial graphene on ruthenium, and more generally on carbonaceous substrates such as graphene or graphite. Based on existing potentials for pure carbon or ruthenium, the potential was carefully parametrized on dedicated electronic structure data for reference structures particularly including epitaxial graphene [201, 206]. Except for very small adsorbates or adatoms, the potential is accurate and can be further improved to include dispersion corrections in the empirical pairwise format made popular by Grimme [76]. Without additional fitting parameter, the dispersion-corrected BOP also reproduces existing electronic structure properties likewise evaluated by taking dispersion effects into account [67].

Also for epitaxial graphene on Ru(0001) dispersion forces turn out to be rather significant in binding the graphene layer to the Ru(0001) substrate, but also for the interaction between the NPs and the substrates, increasing the adsorption energy by a typical order of magnitude in the latter case. The thermal stability was addressed by carrying MD simulations, from which specific dynamical properties were also inferred such as the diffusion constant of adsorbates or the main vibrational frequency corresponding to the Raman G band of graphene. Ru NPs soft-landed on graphite were found to diffuse quite significantly, which agrees with earlier experiments on other NPs [41] and our own results on platinum.

Application of the present models to epitaxial graphene on Ru(0001) under different commensurate ratios reveals moiré structures that are in good agreement with existing DFT calculations or available measurements. Some properties, such as the corrugation of the upper metal layer, were found to agree best only once thermal effects were taken into account. Although size effects were not generally found as significant, the strain resulting from employing a common simulation cell for the two materials was identified as a very sensitive issue notably influencing the corrugation and the vibrational response.

Ru NPs on epitaxial graphene on ruthenium were also found to be thermally much more stable than when adsorbed on graphite. To the price of some internal structural rearrangements upon deposition, the annealed NPs diffuse less and remain solid at high temperatures under the nanosecond time scale. This observation remains valid in absence of dispersion interactions, although some differences in the internal isomerization dynamics and in the onset of global mobility were noted. Those changes in the dynamical behavior suggest different underlying energy landscapes depending on the magnitude of dispersion forces. Characterizing those landscapes could be valuable in the future in order to rationalize the simulation results. Another natural extension worth considering could be to determine the relative thermal stability of the deposited NPs on different moiré structures with different commensurabilities or originating from different relative orientations between the two lattices. In particular, it is unclear whether such strong stabilities would remain in moirés with larger periodicities associated with lesser buckling.

Additional applications of interest for the present BOP include bilayer graphene on Ru(0001), where several rotational domains with different properties have been evidenced experimentally [193, 200, 209, 210, 212]. Local defects in the substrate, especially in the case of graphite, could also alter the diffusion rates of adsorbates [141, 157], promote pinning and thus enhance their stability. This is notably relevant in the context of magnetic storage or catalysis, where coalescence between the deposited NPs should be avoided.

### Other transition metal-carbon systems

Another parametrization of the Brenner BOP has been attempted on the basis of a reference structure of epitaxial graphene on iridium obtained in dispersion corrected electronic structure calculations [235]. The reproduction of the reference structure of graphene/Ir(111) is reasonable as well as the behavior of the system in MD simulations at finite temperature. Difficulties were related to the very weak interaction of graphene with the Ir(111) support caused by dispersion forces. However the dispersion model developed in this work could not be applied in order to avoid double counting of these forces since they had already been included in the DFT calculations that served as a training set for the parametrization of the BOP. Therefore, the effect of long-range dispersion interactions could not be assessed in the case of these systems. In addition, the Ir-C BOP turned out to be less reliable for the description of Ir adsorbates, especially small ones, on carbonaceous substrates.

Epitaxial graphene on Ni(111) and Ni adsorbates thereon as well as on free graphene have been studied with the help of the TB-FMA model [237, 260] in MC simulations. In contrast to the other epitaxial graphene on transition metal structures discussed in this work, graphene on Ni(111) forms mostly (for zero inplane angle between graphene and Ni(111)) commensurate structures. Geometrically, this has the interesting effect that the artificial strain on the graphene layer exerted by the common simulation box, that had to be taken into consideration in the case of the other metals, is independent of the inplane angle. This allowed to discuss the influence of the pure moiré effect for non-zero inplane angles in comparison to the aligned commensurate structure. Furthermore, comparing the thermal stability of Ni adsorbates on free graphene

with those on epitaxial graphene on Ni(111), it was found that their internal stability may be increased due to the epitaxial contact of their supporting graphene sheet, even though the TB-FMA model lacks an explicit account for long-ranged dispersion forces.

### Perspectives

Experimentally, metal adorbates on GOM with unequal metals for the adorbates and the epitaxial support have been studied [37]. The present model could be extended to describe this type of systems. The description of the dispersion forces could be expected to be reusable simply by adjusting the dispersion coefficients, while a new parametrization for the unequal metal-metal interactions of the TB-SMA potential would be necessary. In a first attempt, such parameter sets could be obtained using combination rules for the different coefficients or in a more involved approach by carrying out full parameter optimizations on experimental or *ab initio* data.

Future work could be devoted to constructing a coarse-grained model in order to treat entire assemblies of NPs over more realistic time and length scales than those covered at the present atomistic level. Coarse graining could be attempted at different levels: Most straight forward might be the inclusion of the covalent forces into an implicit model as we did in this work for dispersion forces so that the interaction of the atoms of the nanoparticles with the substrate would be described by the coarse grained model only. In addition, the specific coalescence mechanisms could be addressed by performing biased simulations and determining the effective interactions (potential of mean force), which would subsequently feed the coarser model through stochastic dynamics.

It would also be instructive to carry out a more detailed analysis of the vibrational spectra of epitaxial graphene. In this work, we identified the G peak in the spectra and considered the effect of system size, temperature and strain on its frequency. However, graphene spectra have many other features that allow experimentally to assess graphene quality (defects) or the number of epitaxial layers [171]. It would be interesting to identify other peaks and study the dependency as a function of these system features with the present model.



# Bibliography

- [1] H. W. Kroto, J. R. Heath, S. C. O'Brien, R. F. Curl, and R. E. Smalley, "C<sub>60</sub>: Buckminsterfullerene," *Nature (London)* **318**, 162 (1985).
- [2] E. T. Thostenson, Z. Ren, and T.-W. Chou, "Advances in the science and technology of carbon nanotubes and their composites: A review," *Compos. Sci. Technol.* **61**, 1899 (2001).
- [3] K. S. Novoselov, A. K. Geim, S. V. Morozov, D. Jiang, Y. Zhang, S. V. Dubonos, I. V. Grigorieva, and A. A. Firsov, "Electric field effect in atomically thin carbon films," *Science* **306**, 666 (2004).
- [4] K.-L. Wu, X.-Z. Li, X.-W. Wei, T.-H. Ding, M. Jiang, W.-J. Zhang, and Y. Ye, "Controllable synthesis and property of graphene-based magnetic metal nanostructures," *Solid State Sci.* **38**, 90 (2014).
- [5] I. A. Aksay, M. Trau, S. Manne, I. Honma, N. Yao, L. Zhou, P. Fenter, P. M. Eisenberger, and S. M. Gruner, "Biomimetic pathways for assembling inorganic thin films," *Science* **273**, 892 (1996).
- [6] S. Utamapanya, K. J. Klabunde, and J. R. Schlup, "Nanoscale metal oxide particles/clusters as chemical reagents. Synthesis and properties of ultrahigh surface area magnesium hydroxide and magnesium oxide," *Chem. Mater.* **3**, 175 (1991).
- [7] J. P. Rao and K. E. Geckeler, "Polymer nanoparticles: Preparation techniques and size-control parameters," *Prog. Polym. Sci.* **36**, 887 (2011).
- [8] R. D. Handy, R. Owen, and E. Valsami-Jones, "The ecotoxicology of nanoparticles and nanomaterials: Current status, knowledge gaps, challenges, and future needs," *Ecotoxicology* **17**, 315 (2008).
- [9] F. D. Sikkema, M. Comellas-Aragones, R. G. Fokkink, B. J. M. Verduin, J. J. L. M. Cornelissen, and R. J. M. Nolte, "Monodisperse polymer-virus hybrid nanoparticles," *Org. Biomol. Chem.* **5**, 54 (2007).
- [10] L. M. Liz-Marzán, "Nanometals: Formation and color," *Mater. Today* **7**, 26 (2004).
- [11] J. B. Donnet, *Carbon Black: Science and Technology, Second Edition* (Taylor & Francis, 1993).
- [12] M. Rai, A. Yadav, and A. Gade, "Silver nanoparticles as a new generation of antimicrobials," *Biotechnol. Adv.* **27**, 76 (2009).
- [13] F. Vines, J. R. B. Gomes, and F. Illas, "Understanding the reactivity of metallic nanoparticles: Beyond the extended surface model for catalysis," *Chem. Soc. Rev.* **43**, 4922 (2014).

- [14] R. Singh and J. W. Lillard, Jr., “Nanoparticle-based targeted drug delivery,” *Exp. Mol. Pathol.* **86**, 215 (2009).
- [15] P. Jensen, “Growth of nanostructures by cluster deposition: Experiments and simple models,” *Rev. Mod. Phys.* **71**, 1695 (1999).
- [16] S. M. Davis, F. Zaera, and G. A. Somorjai, “Surface structure and temperature dependence of n-hexane skeletal rearrangement reactions catalyzed over platinum single crystal surfaces: Marked structure sensitivity of aromatization,” *J. Catal.* **85**, 206 (1984).
- [17] R. Ferrando, J. Jellinek, and R. L. Johnston, “Nanoalloys: From theory to applications of alloy clusters and nanoparticles,” *Chem. Rev.* **108**, 845 (2008).
- [18] G. D. Förster, Y. Magnin, F. Rabilloud, and F. Calvo, “Effective embedded-atom potential for metallic adsorbates on crystalline surfaces,” *Modell. Simul. Mater. Sci. Eng.* **22**, 035015 (2014).
- [19] A. T. N’Diaye, S. Bleikamp, P. J. Feibelman, and T. Michely, “Two-dimensional Ir cluster lattice on a graphene moiré on Ir(111),” *Phys. Rev. Lett.* **97**, 215501 (2006).
- [20] D. L. Feldheim and C. A. Foss Jr., *Metal Nanoparticles: Synthesis Characterization and Applications* (Marcel Dekker, New York, 2002).
- [21] I. Fernandez-Torrente, S. Monturet, K. J. Franke, J. Fraxedas, N. Lorente, and J. I. Pascual, “Long-range repulsive interaction between molecules on a metal surface induced by charge transfer,” *Phys. Rev. Lett.* **99**, 176103 (2007).
- [22] S. Kinge, M. Crego-Calama, and D. N. Reinhoudt, “Self-assembling nanoparticles at surfaces and interfaces,” *ChemPhysChem* **9**, 20 (2008).
- [23] L. Bardotti, F. Tournus, P. Mélinon, M. Pellarin, and M. Broyer, “Mass-selected clusters deposited on graphite: Spontaneous organization controlled by cluster surface reaction,” *Phys. Rev. B* **83**, 035425 (2011).
- [24] J. Coraux, A. T. N’Diaye, N. Rougemaille, C. Vo-Van, A. Kimouche, H.-X. Yang, M. Chshiev, N. Bendiab, O. Fruchart, and A. K. Schmid, “Air-protected epitaxial graphene/ferromagnet hybrids prepared by chemical vapor deposition and intercalation,” *J. Phys. Chem. Lett.* **3**, 2059 (2012).
- [25] A. Cavallin, M. Pozzo, C. Africh, A. Baraldi, E. Vesselli, C. Dri, G. Comelli, R. Larciprete, P. Lacovig, S. Lizzit, and D. Alfè, “Local electronic structure and density of edge and facet atoms at Rh nanoclusters self-assembled on a graphene template,” *ACS Nano* **6**, 3034 (2012).
- [26] K. Yamamoto, T. Imaoka, W.-J. Chun, O. Enoki, H. Katoh, M. Takenaga, and A. Sonoi, “Size-specific catalytic activity of platinum clusters enhances oxygen reduction reactions,” *Nat. Chem.* **1**, 397 (2009).
- [27] R. Siburian, T. Kondo, and J. Nakamura, “Size control to a sub-nanometer scale in platinum catalysts on graphene,” *J. Phys. Chem. C* **117**, 3635 (2013).
- [28] Y. Shen, Z. Zhang, K. Xiao, and J. Xi, “Electrocatalytic activity of Pt sub-nano/nanoclusters stabilized by pristine graphene nanosheets,” *Phys. Chem. Chem. Phys.* **16**, 21609 (2014).

- [29] P. R. Wallace, "The band theory of graphite," *Phys. Rev.* **71**, 622 (1947).
- [30] S.-J. Han, A. V. Garcia, S. Oida, K. A. Jenkins, and W. Haensch, "Graphene radio frequency receiver integrated circuit," *Nat. Commun.* **5**, 3806 (2014).
- [31] S. Iijima, "Helical microtubules of graphitic carbon," *Nature (London)* **354**, 56 (1991).
- [32] H. Tetlow, J. Posthuma de Boer, I. J. Ford, D. D. Vvedensky, J. Coraux, and L. Kantorovich, "Growth of epitaxial graphene: Theory and experiment," *Phys. Rep.* **542**, 195 (2014).
- [33] K. S. Novoselov, A. K. Geim, S. V. Morozov, D. Jiang, M. I. Katsnelson, I. V. Grigorieva, S. V. Dubonos, and A. A. Firsov, "Two-dimensional gas of massless dirac fermions in graphene," *Nature (London)* **438**, 197 (2005).
- [34] R. R. Nair, P. Blake, A. N. Grigorenko, K. S. Novoselov, T. J. Booth, T. Stauber, N. M. R. Peres, and A. K. Geim, "Fine structure constant defines visual transparency of graphene," *Science* **320**, 1308 (2008).
- [35] C. Lee, X. Wei, J. W. Kysar, and J. Hone, "Measurement of the elastic properties and intrinsic strength of monolayer graphene," *Science* **321**, 385 (2008).
- [36] Y. Magnin, G. D. Förster, F. Rabilloud, F. Calvo, A. Zappelli, and C. Bichara, "Thermal expansion of free-standing graphene: Benchmarking semi-empirical potentials," *J. Phys.: Condens. Matter* **26**, 185401 (2014).
- [37] S. Linas, F. Jean, T. Zhou, C. Albin, G. Renaud, L. Bardotti, and F. Tournus, "Moiré induced organization of size-selected Pt clusters soft landed on epitaxial graphene," *Sci. Rep.* **5**, 13053 (2015).
- [38] D. D. L. Chung, "Review graphite," *J. Mater. Sci.* **37**, 1475 (2002).
- [39] G. Ramos-Sanchez and P. B. Balbuena, "Interactions of platinum clusters with a graphite substrate," *Phys. Chem. Chem. Phys.* **15**, 11950 (2013).
- [40] R. P. Galhenage, K. Xie, W. Diao, J. M. M. Tengco, G. S. Seuser, J. R. Monnier, and D. A. Chen, "Platinum-ruthenium bimetallic clusters on graphite: A comparison of vapor deposition and electroless deposition methods," *Phys. Chem. Chem. Phys.* (2015), 10.1039/C5CP00075K.
- [41] L. Bardotti, P. Jensen, A. Hoareau, M. Treilleux, and B. Cabaud, "Experimental observation of fast diffusion of large antimony clusters on graphite surfaces," *Phys. Rev. Lett.* **74**, 4694 (1995).
- [42] Y. Maruyama, "Temperature dependence of Lévy-type stick-slip diffusion of a gold nanocluster on graphite," *Phys. Rev. B* **69**, 245408 (2004).
- [43] S. Hagstrom, H. B. Lyon, and G. A. Somorjai, "Surface structures on the clean platinum (100) surface," *Phys. Rev. Lett.* **15**, 491 (1965).
- [44] J. T. Grant and T. W. Haas, "A study of Ru(0001) and Rh(111) surfaces using LEED and Auger electron spectroscopy," *Surf. Sci.* **21**, 76 (1970).
- [45] J. Wintterlin and M.-L. Bocquet, "Graphene on metal surfaces," *Surf. Sci.* **603**, 1841 (2009).

- [46] E. Sutter, P. Albrecht, F. E. Camino, and P. Sutter, “Monolayer graphene as ultimate chemical passivation layer for arbitrarily shaped metal surfaces,” *Carbon* **48**, 4414 (2010).
- [47] S. P. Gubin, Y. I. Spichkin, G. Y. Yurkov, and A. M. Tishin, “Nanomaterial for high-density magnetic data storage,” *Russ. J. Inorg. Chem.* **47**, S32 (2002).
- [48] K. Donner and P. Jakob, “Structural properties and site specific interactions of Pt with the graphene/Ru(0001) moiré overlayer,” *J. Chem. Phys.* **131**, 164701 (2009).
- [49] Y. Pan, M. Gao, L. Huang, F. Liu, and H.-J. Gao, “Directed self-assembly of monodispersed platinum nanoclusters on graphene moiré template,” *Appl. Phys. Lett.* **95**, 093106 (2009).
- [50] H. Zhang, Q. Fu, Y. Cui, D. L. Tan, and X. H. Bao, “Fabrication of metal nanoclusters on graphene grown on Ru(0001),” *Chin. Sci. Bull.* **54**, 2446 (2009).
- [51] Z. Zhou, F. Gao, and D. W. Goodman, “Deposition of metal clusters on single-layer graphene/Ru(0001): Factors that govern cluster growth,” *Surf. Sci.* **604**, L31 (2010).
- [52] A. K. Engstfeld, S. Beckord, C. D. Lorenz, and R. J. Behm, “Growth of PtRu clusters on Ru(0001)-supported monolayer graphene films,” *ChemPhysChem* **13**, 3313 (2012).
- [53] Y. Han, A. K. Engstfeld, C.-Z. Wang, L. D. Roelofs, R. J. Behm, and J. W. Evans, “Atomistic modeling of Ru nanocluster formation on graphene/Ru(0001): Thermodynamically versus kinetically directed-assembly,” *MRS Online Proc. Libr.* **1498**, 249 (2013).
- [54] A. K. Engstfeld, H. E. Hoster, R. J. Behm, L. D. Roelofs, X. Liu, C.-Z. Wang, Y. Han, and J. W. Evans, “Directed assembly of Ru nanoclusters on Ru(0001)-supported graphene: STM studies and atomistic modeling,” *Phys. Rev. B* **86**, 085442 (2012).
- [55] N. Blanc, J. Coraux, C. Vo-Van, A. T. N’Diaye, O. Geaymond, and G. Renaud, “Local deformations and incommensurability of high-quality epitaxial graphene on a weakly interacting transition metal,” *Phys. Rev. B* **86**, 235439 (2012).
- [56] P. J. Feibelman, “Pinning of graphene to Ir(111) by flat Ir dots,” *Phys. Rev. B* **77**, 165419 (2008).
- [57] G. D. Förster, F. Rabilloud, and F. Calvo, “Adsorption of metal nanoparticles on carbon substrates and epitaxial graphene: Assessing models for dispersion forces,” *Phys. Rev. B* **91**, 245433 (2015).
- [58] P. Hohenberg and W. Kohn, “Inhomogeneous electron gas,” *Phys. Rev.* **136**, B864 (1964).
- [59] W. Kohn and L. J. Sham, “Self-consistent equations including exchange and correlation effects,” *Phys. Rev.* **140**, A1133 (1965).
- [60] P. Sony, P. Puschnig, D. Nabok, and C. Ambrosch-Draxl, “Importance of van der Waals interaction for organic molecule-metal junctions: Adsorption of thiophene on Cu(110) as a prototype,” *Phys. Rev. Lett.* **99**, 176401 (2007).
- [61] G. Mercurio, E. R. McNellis, I. Martin, S. Hagen, F. Leyssner, S. Soubatch, J. Meyer, M. Wolf, P. Tegeder, F. S. Tautz, and K. Reuter, “Structure and energetics of azobenzene on Ag(111): Benchmarking semiempirical dispersion correction approaches,” *Phys. Rev. Lett.* **104**, 036102 (2010).

- [62] N. Atodiresei, V. Caciuc, P. Lazić, and S. Blügel, “Chemical versus van der Waals interaction: The role of the heteroatom in the flat absorption of aromatic molecules  $C_6H_6$ ,  $C_5NH_5$ , and  $C_4N_2H_4$  on the Cu(110) surface,” *Phys. Rev. Lett.* **102**, 136809 (2009).
- [63] J. Brede, N. Atodiresei, S. Kuck, P. Lazić, V. Caciuc, Y. Morikawa, G. Hoffmann, S. Blügel, and R. Wiesendanger, “Spin- and energy-dependent tunneling through a single molecule with intramolecular spatial resolution,” *Phys. Rev. Lett.* **105**, 047204 (2010).
- [64] E. R. McNellis, C. Bronner, J. Meyer, M. Weinelt, P. Tegeder, and K. Reuter, “Azobenzene versus 3,3',5,5'-tetra-tert-butyl-azobenzene (TBA) at Au(111): Characterizing the role of spacer groups,” *Phys. Chem. Chem. Phys.* **12**, 6404 (2010).
- [65] M. Mura, A. Gulans, T. Thonhauser, and L. Kantorovich, “Role of van der Waals interaction in forming molecule-metal junctions: Flat organic molecules on the Au(111) surface,” *Phys. Chem. Chem. Phys.* **12**, 4759 (2010).
- [66] A. Tkatchenko, “Current understanding of van der Waals effects in realistic materials,” *Adv. Funct. Mater.* **25**, 2054 (2015).
- [67] D. Stradi, S. Barja, C. Díaz, M. Garnica, B. Borca, J. J. Hinarejos, D. Sánchez-Portal, M. Alcamí, A. Arnau, A. L. Vázquez de Parga, R. Miranda, and F. Martín, “Role of dispersion forces in the structure of graphene monolayers on Ru surfaces,” *Phys. Rev. Lett.* **106**, 186102 (2011).
- [68] P. Janthon, F. Viñes, S. M. Kozlov, J. Limtrakul, and F. Illas, “Theoretical assessment of graphene-metal contacts,” *J. Chem. Phys.* **138**, 244701 (2013).
- [69] M. P. Andersson, “Density functional theory with modified dispersion correction for metals applied to self-assembled monolayers of thiols on Au(111),” *J. Theor. Chem.* **2013**, 327839 (2013).
- [70] S. Grimme, “Density functional theory with London dispersion corrections,” *Wiley Interdiscip. Rev.: Comput. Mol. Sci.* **1**, 211 (2011).
- [71] M. Dion, H. Rydberg, E. Schröder, D. C. Langreth, and B. I. Lundqvist, “Van der Waals density functional for general geometries,” *Phys. Rev. Lett.* **92**, 246401 (2004).
- [72] K. Lee, E. D. Murray, L. Kong, B. I. Lundqvist, and D. C. Langreth, “Higher-accuracy van der Waals density functional,” *Phys. Rev. B* **82**, 081101 (2010).
- [73] Y. Zhao and D. G. Truhlar, “Density functionals with broad applicability in chemistry,” *Acc. Chem. Res.* **41**, 157 (2008).
- [74] L. Ferrighi, Y.-X. Pan, H. Grönbeck, and B. Hammer, “Study of alkylthiolate self-assembled monolayers on Au(111) using a semilocal meta-GGA density functional,” *J. Phys. Chem. C* **116**, 7374 (2012).
- [75] S. Grimme, “Accurate description of van der Waals complexes by density functional theory including empirical corrections,” *J. Comput. Chem.* **25**, 1463 (2004).
- [76] S. Grimme, “Semiempirical GGA-type density functional constructed with a long-range dispersion correction,” *J. Comput. Chem.* **27**, 1787 (2006).

- [77] S. Grimme, J. Antony, S. Ehrlich, and H. Krieg, “A consistent and accurate ab initio parametrization of density functional dispersion correction (DFT-D) for the 94 elements H-Pu,” *J. Chem. Phys.* **132**, 154104 (2010).
- [78] S. Grimme, S. Ehrlich, and L. Goerigk, “Effect of the damping function in dispersion corrected density functional theory,” *J. Comput. Chem.* **32**, 1456 (2011).
- [79] P. Jurečka, J. Černý, P. Hobza, and D. R. Salahub, “Density functional theory augmented with an empirical dispersion term. Interaction energies and geometries of 80 noncovalent complexes compared with ab initio quantum mechanics calculations,” *J. Comput. Chem.* **28**, 555 (2007).
- [80] P. L. Silvestrelli, “Van der Waals interactions in DFT made easy by Wannier functions,” *Phys. Rev. Lett.* **100**, 053002 (2008).
- [81] A. Tkatchenko and M. Scheffler, “Accurate molecular van der Waals interactions from ground-state electron density and free-atom reference data,” *Phys. Rev. Lett.* **102**, 073005 (2009).
- [82] R. Podgornik, R. H. French, and V. A. Parsegian, “Nonadditivity in van der Waals interactions within multilayers,” *J. Chem. Phys.* **124**, 044709 (2006).
- [83] B. E. Sernelius and C. E. Román-Velázquez, “Beyond the simple proximity force approximation: Geometrical effects on the nonretarded Casimir interaction,” *Phys. Rev. A* **78**, 032111 (2008).
- [84] J. Sarabadani, A. Naji, R. Asgari, and R. Podgornik, “Many-body effects in the van der Waals–Casimir interaction between graphene layers,” *Phys. Rev. B* **84**, 155407 (2011).
- [85] C. Wagner, N. Fournier, V. G. Ruiz, C. Li, K. Müllen, M. Rohlfing, A. Tkatchenko, R. Temirov, and F. S. Tautz, “Non-additivity of molecule-surface van der Waals potentials from force measurements,” *Nat. Commun.* **5**, 5568 (2014).
- [86] C. F. A. Negre and C. G. Sánchez, *Optical Properties of Metal Nanoclusters from an Atomistic Point of View*, Nanostructure Science and Technology (Springer New York, 2013).
- [87] N. W. Ashcroft and N. D. Mermin, *Solid State Physics* (Holt, Rinehart and Winston, 1976).
- [88] C. M. Goringe, D. R. Bowler, and E. Hernández, “Tight-binding modelling of materials,” *Rep. Prog. Phys.* **60**, 1447 (1997).
- [89] K. Saitoh and H. Hayakawa, “Simulation of depositions of a Lennard-Jones cluster on a crystalline surface,” *Prog. Theor. Phys.* **122**, 1081 (2009).
- [90] J. E. Jones, “On the determination of molecular fields. II. From the equation of state of a gas,” *Proc. R. Soc. London, Ser. A* **106**, 463 (1924).
- [91] M. S. Daw and M. I. Baskes, “Semiempirical, quantum mechanical calculation of hydrogen embrittlement in metals,” *Phys. Rev. Lett.* **50**, 1285 (1983).
- [92] M. S. Daw and M. I. Baskes, “Embedded-atom method: Derivation and application to impurities, surfaces, and other defects in metals,” *Phys. Rev. B* **29**, 6443 (1984).

- [93] J. Tersoff, “New empirical model for the structural properties of silicon,” *Phys. Rev. Lett.* **56**, 632 (1986).
- [94] F. Cleri and V. Rosato, “Tight-binding potentials for transition metals and alloys,” *Phys. Rev. B* **48**, 22 (1993).
- [95] F. Cyrot-Lackmann, “On the calculation of surface tension in transition metals,” *Surf. Sci.* **15**, 535 (1969).
- [96] K. Albe, K. Nordlund, and R. S. Averback, “Modeling the metal-semiconductor interaction: Analytical bond-order potential for platinum-carbon,” *Phys. Rev. B* **65**, 195124 (2002).
- [97] D. W. Brenner, “Relationship between the embedded-atom method and Tersoff potentials,” *Phys. Rev. Lett.* **63**, 1022 (1989).
- [98] L. Pauling, “The nature of the chemical bond. Application of results obtained from the quantum mechanics and from a theory of paramagnetic susceptibility to the structure of molecules,” *J. Am. Chem. Soc.* **53**, 1367 (1931).
- [99] G. C. Abell, “Empirical chemical pseudopotential theory of molecular and metallic bonding,” *Phys. Rev. B* **31**, 6184 (1985).
- [100] F. H. Stillinger and T. A. Weber, “Computer simulation of local order in condensed phases of silicon,” *Phys. Rev. B* **31**, 5262 (1985).
- [101] D. W. Brenner, “Empirical potential for hydrocarbons for use in simulating the chemical vapor deposition of diamond films,” *Phys. Rev. B* **42**, 9458 (1990).
- [102] P. Erhart and K. Albe, “Analytical potential for atomistic simulations of silicon, carbon, and silicon carbide,” *Phys. Rev. B* **71**, 035211 (2005).
- [103] P. Erhart, N. Juslin, O. Goy, K. Nordlund, R. Müller, and K. Albe, “Analytic bond-order potential for atomistic simulations of zinc oxide,” *J. Phys.: Condens. Matter* **18**, 6585 (2006).
- [104] K. O. E. Henriksson and K. Nordlund, “Simulations of cementite: An analytical potential for the Fe-C system,” *Phys. Rev. B* **79**, 144107 (2009).
- [105] C. Björkas, K. O. E. Henriksson, M. Probst, and K. Nordlund, “A Be-W interatomic potential,” *J. Phys.: Condens. Matter* **22**, 352206 (2010).
- [106] S. Agostinelli, J. Allison, K. Amako, J. Apostolakis, H. Araujo, P. Arce, M. Asai, D. Axen, S. Banerjee, G. Barrand, *et al.*, “Geant4-a simulation toolkit,” *Nucl. Instrum. Methods Phys. Res., Sect. A* **506**, 250 (2003).
- [107] E. S. Epstein, “Stochastic dynamic prediction,” *Tellus* **21**, 739 (1969).
- [108] N. Metropolis, A. W. Rosenbluth, M. N. Rosenbluth, A. H. Teller, and E. Teller, “Equation of state calculations by fast computing machines,” *J. Chem. Phys.* **21**, 1087 (1953).
- [109] W. K. Hastings, “Monte Carlo sampling methods using markov chains and their applications,” *Biometrika* **57**, 97 (1970).

- [110] P. Allen and D. J. Tildesley, *Computer Simulation of Liquids*, Oxford Science Publications (Clarendon Press, 1989).
- [111] D. Frenkel and B. Smit, *Understanding molecular simulation: From algorithms to applications* (Academic Press, 1996).
- [112] S. Kirkpatrick, C. D. Gelatt, and M. P. Vecchi, "Optimization by simulated annealing," *Science* **220**, 671 (1983).
- [113] V. Černý, "Thermodynamical approach to the traveling salesman problem: An efficient simulation algorithm," *J. Optim. Theory Appl.* **45**, 41 (1985).
- [114] R. H. Swendsen and J.-S. Wang, "Replica Monte Carlo simulation of spin-glasses," *Phys. Rev. Lett.* **57**, 2607 (1986).
- [115] D. J. Earl and M. W. Deem, "Parallel tempering: Theory, applications, and new perspectives," *Phys. Chem. Chem. Phys.* **7**, 3910 (2005).
- [116] W. A. Steele, "The physical interaction of gases with crystalline solids: I. Gas-solid energies and properties of isolated adsorbed atoms," *Surf. Sci.* **36**, 317 (1973).
- [117] P. Pyykkö and M. Atsumi, "Molecular double-bond covalent radii for elements Li–E112," *Chem. - Eur. J.* **15**, 12770 (2009).
- [118] J. Che, T. Çağın, and W. A. Goddard III, "Generalized extended empirical bond-order dependent force fields including nonbond interactions," *Theor. Chem. Acc.* **102**, 346 (1999).
- [119] T. Gould, S. Lebègue, and J. F. Dobson, "Dispersion corrections in graphenic systems: A simple and effective model of binding," *J. Phys.: Condens. Matter* **25**, 445010 (2013).
- [120] B. G. Janesko, T. M. Henderson, and G. E. Scuseria, "Screened hybrid density functionals for solid-state chemistry and physics," *Phys. Chem. Chem. Phys.* **11**, 443 (2009).
- [121] P. L. Silvestrelli, A. Ambrosetti, S. Grubisić, and F. Ancilotto, "Adsorption of rare-gas atoms on Cu(111) and Pb(111) surfaces by van der Waals corrected density functional theory," *Phys. Rev. B* **85**, 165405 (2012).
- [122] P. L. Silvestrelli and A. Ambrosetti, "Inclusion of screening effects in the van der Waals corrected DFT simulation of adsorption processes on metal surfaces," *Phys. Rev. B* **87**, 075401 (2013).
- [123] P. L. Silvestrelli and A. Ambrosetti, "Including screening in van der Waals corrected density functional theory calculations: The case of atoms and small molecules physisorbed on graphene," *J. Chem. Phys.* **140**, 124107 (2014).
- [124] E. W. Weisstein, *CRC Concise Encyclopedia of Mathematics, Second Edition* (CRC Press, 2002).
- [125] M. Gao, Y. Pan, L. Huang, H. Hu, L. Z. Zhang, H. M. Guo, S. X. Du, and H.-J. Gao, "Epitaxial growth and structural property of graphene on Pt(111)," *Appl. Phys. Lett.* **98**, 033101 (2011).
- [126] P. Merino, M. Švec, A. L. Pinardi, G. Otero, and J. A. Martín-Gago, "Strain-driven moiré superstructures of epitaxial graphene on transition metal surfaces," *ACS Nano* **5**, 5627 (2011).

- [127] L. Meng, R. Wu, L. Zhang, L. Li, S. Du, Y. Wang, and H.-J. Gao, “Multi-oriented moiré superstructures of graphene on Ir(111): Experimental observations and theoretical models,” *J. Phys.: Condens. Matter* **24**, 314214 (2012).
- [128] K. Hermann, “Periodic overlayers and moiré patterns: Theoretical studies of geometric properties,” *J. Phys.: Condens. Matter* **24**, 314210 (2012).
- [129] P. Zeller and S. Günther, “What are the possible moiré patterns of graphene on hexagonally packed surfaces? Universal solution for hexagonal coincidence lattices, derived by a geometric construction,” *New J. Phys.* **16**, 083028 (2014).
- [130] E. A. Wood, “Vocabulary of surface crystallography,” *J. Appl. Phys.* **35**, 1306 (1964).
- [131] D. J. Wales and J. P. K. Doye, “Global optimization by basin-hopping and the lowest energy structures of Lennard Jones clusters containing up to 110 atoms,” *J. Phys. Chem. A* **101**, 5111 (1997).
- [132] H. Mühlenbein, M. Schomisch, and J. Born, “The parallel genetic algorithm as function optimizer,” *Parallel Comput.* **17**, 619 (1991).
- [133] W. H. Press, *Numerical Recipes in FORTRAN 90: The Art of Scientific Computing*, Fortran numerical recipes (Cambridge University Press, 1992).
- [134] G. J. Martyna, M. L. Klein, and M. Tuckerman, “Nosé-hoover chains: The canonical ensemble via continuous dynamics,” *J. Chem. Phys.* **97**, 2635 (1992).
- [135] Y. Si and E. T. Samulski, “Exfoliated graphene separated by platinum nanoparticles,” *Chem. Mater.* **20**, 6792 (2008).
- [136] L. Wang and R. T. Yang, “Hydrogen storage properties of carbons doped with ruthenium, platinum, and nickel nanoparticles,” *J. Phys. Chem. C* **112**, 12486 (2008).
- [137] D.-H. Lim and J. Wilcox, “Mechanisms of the oxygen reduction reaction on defective graphene-supported Pt nanoparticles from first-principles,” *J. Phys. Chem. C* **116**, 3653 (2012).
- [138] S. Hu, M. Lozada-Hidalgo, F. C. Wang, A. Mishchenko, F. Schedin, R. R. Nair, E. W. Hill, D. W. Boukhvalov, M. I. Katsnelson, R. A. W. Dryfe, I. V. Grigorieva, H. A. Wu, and A. K. Geim, “Proton transport through one-atom-thick crystals,” *Nature (London)* **516**, 227 (2014).
- [139] A. I. Frenkel, C. W. Hills, and R. G. Nuzzo, “A view from the inside: Complexity in the atomic scale ordering of supported metal nanoparticles,” *J. Phys. Chem. B* **105**, 12689 (2001).
- [140] D. Franz, S. Runte, C. Busse, S. Schumacher, T. Gerber, T. Michely, M. Mantilla, V. Kilic, J. Zegenhagen, and A. Stierle, “Atomic structure and crystalline order of graphene-supported Ir nanoparticle lattices,” *Phys. Rev. Lett.* **110**, 065503 (2013).
- [141] M. Bassioui, E. Álvarez Zauco, and V. A. Basiuk, “Theoretical analysis of the effect of surface defects on porphyrin adsorption and self-assembly on graphite,” *J. Comput. Theor. Nanosci.* **9**, 532 (2012).

- [142] A. Perez, L. Bardotti, B. Prevel, P. Jensen, M. Treilleux, P. Mélinon, J. Gierak, G. Faini, and D. Mailly, “Quantum-dot systems prepared by 2D organization of nanoclusters performed in the gas phase on functionalized substrates,” *New J. Phys.* **4**, 76 (2002).
- [143] X. Tang, X. Li, Y. Wang, K. Wepasnick, A. Lim, D. H. Fairbrother, K. H. Bowen, T. Mangler, S. Noessner, C. Wolke, M. Grossmann, A. Koop, G. Gantefoer, B. Kiran, and A. K. Kandalam, “Size selected clusters on surfaces,” *J. Phys.: Conf. Ser.* **438**, 012005 (2013).
- [144] X. Li, K. Wepasnick, X. Tang, D. H. Fairbrother, K. H. Bowen, A. Dollinger, C. H. Strobel, J. Huber, T. Mangler, Y. Luo, S. Proch, and G. Gantefoer, “A new nanomaterial synthesized from size-selected, ligand-free metal clusters,” *J. Appl. Phys.* **115**, 104304 (2014).
- [145] F. Baletto and R. Ferrando, “Structural properties of nanoclusters: Energetic, thermodynamic, and kinetic effects,” *Rev. Mod. Phys.* **77**, 371 (2005).
- [146] M. N. Groves, C. Malardier-Jugroot, and M. Jugroot, “Improving platinum catalyst durability with a doped graphene support,” *J. Phys. Chem. C* **116**, 10548 (2012).
- [147] G. Kim, Y. Kawazoe, and K.-R. Lee, “Controlled catalytic properties of platinum clusters on strained graphene,” *J. Phys. Chem. Lett.* **3**, 1989 (2012).
- [148] I. Fampiou and A. Ramasubramaniam, “Binding of Pt nanoclusters to point defects in graphene: Adsorption, morphology, and electronic structure,” *J. Phys. Chem. C* **116**, 6543 (2012).
- [149] K.-J. Kong, Y. Choi, B.-H. Ryu, J.-O. Lee, and H. Chang, “Investigation of metal/carbon-related materials for fuel cell applications by electronic structure calculations,” *J. Mater. Sci. Eng. C* **26**, 1207 (2006).
- [150] K. Okazaki-Maeda, Y. Morikawa, S. Tanaka, and M. Kohyama, “Structures of Pt clusters on graphene by first-principles calculations,” *Surf. Sci.* **604**, 144 (2010).
- [151] A. Rochefort, D.-Q. Yang, and E. Sacher, “Stabilization of platinum nanoparticles on graphene by non-invasive functionalization,” *Carbon* **47**, 2233 (2009).
- [152] Y. Okamoto, “Density-functional calculations of icosahedral  $M_{13}$  ( $M = \text{Pt}$  and  $\text{Au}$ ) clusters on graphene sheets and flakes,” *Chem. Phys. Lett.* **420**, 382 (2006).
- [153] Q. Qi, H. Liu, W. Feng, H. Tian, H. Xu, and X. Huang, “Theoretical investigation on the interaction of subnano platinum clusters with graphene using DFT methods,” *Comput. Mater. Sci.* **96**, 268 (2015).
- [154] R. N. Mantegna and H. E. Stanley, “Stochastic process with ultraslow convergence to a Gaussian: The truncated Lévy flight,” *Phys. Rev. Lett.* **73**, 2946 (1994).
- [155] W. D. Luedtke and U. Landman, “Slip diffusion and Lévy flights of an adsorbed gold nanocluster,” *Phys. Rev. Lett.* **82**, 3835 (1999).
- [156] Y. Maruyama and J. Murakami, “Truncated Lévy walk of a nanocluster bound weakly to an atomically flat surface: Crossover from superdiffusion to normal diffusion,” *Phys. Rev. B* **67**, 085406 (2003).

- [157] O. Stein, J. Ankri, and M. Asscher, "Surface diffusion of gold nanoclusters on Ru(0001): Effects of cluster size, surface defects and adsorbed oxygen atoms," *Phys. Chem. Chem. Phys.* **15**, 13506 (2013).
- [158] M. Enachescu, D. Schleef, D. F. Ogletree, and M. Salmeron, "Integration of point-contact microscopy and atomic-force microscopy: Application to characterization of graphite/Pt(111)," *Phys. Rev. B* **60**, 16913 (1999).
- [159] T. A. Land, T. Michely, R. J. Behm, J. C. Hemminger, and G. Comsa, "STM investigation of single layer graphite structures produced on Pt(111) by hydrocarbon decomposition," *Surf. Sci.* **264**, 261 (1992).
- [160] B. J. Kang, J. H. Mun, C. Y. Hwang, and B. J. Cho, "Monolayer graphene growth on sputtered thin film platinum," *J. Appl. Phys.* **106**, 104309 (2009).
- [161] M. Sasaki, Y. Yamada, Y. Ogiwara, S. Yagyu, and S. Yamamoto, "Moiré contrast in the local tunneling barrier height images of monolayer graphite on Pt(111)," *Phys. Rev. B* **61**, 15653 (2000).
- [162] G. W. Cushing, V. Johánek, J. K. Navin, and I. Harrison, "Graphene growth on Pt(111) by ethylene chemical vapor deposition at surface temperatures near 1000 K," *J. Phys. Chem. C* **119**, 4759 (2015).
- [163] H. Ueta, M. Saida, C. Nakai, Y. Yamada, M. Sasaki, and S. Yamamoto, "Highly oriented monolayer graphite formation on Pt(111) by a supersonic methane beam," *Surf. Sci.* **560**, 183 (2004).
- [164] P. Sutter, J. T. Sadowski, and E. Sutter, "Graphene on Pt(111): Growth and substrate interaction," *Phys. Rev. B* **80**, 245411 (2009).
- [165] S. Grandthyll, S. Gsell, M. Weinl, M. Schreck, S. Hübner, and F. Müller, "Epitaxial growth of graphene on transition metal surfaces: Chemical vapor deposition versus liquid phase deposition," *J. Phys.: Condens. Matter* **24**, 314204 (2012).
- [166] P. A. Khomyakov, G. Giovannetti, P. C. Rusu, G. Brocks, J. van den Brink, and P. J. Kelly, "First-principles study of the interaction and charge transfer between graphene and metals," *Phys. Rev. B* **79**, 195425 (2009).
- [167] M. Vanin, J. J. Mortensen, A. K. Kelkkanen, J. M. Garcia-Lastra, K. S. Thygesen, and K. W. Jacobsen, "Graphene on metals: A van der Waals density functional study," *Phys. Rev. B* **81**, 081408 (2010).
- [168] F. Hanke, M. S. Dyer, J. Björk, and M. Persson, "Structure and stability of weakly chemisorbed ethene adsorbed on low-index Cu surfaces: Performance of density functionals with van der Waals interactions," *J. Phys.: Condens. Matter* **24**, 424217 (2012).
- [169] G. Tsoukleri, J. Parthenios, K. Papagelis, R. Jalil, A. C. Ferrari, A. K. Geim, K. S. Novoselov, and C. Galiotis, "Subjecting a graphene monolayer to tension and compression," *Small* **5**, 2397 (2009).
- [170] F. Tuinstra and J. L. Koenig, "Raman spectrum of graphite," *J. Chem. Phys.* **53**, 1126 (1970).

- [171] T. M. G. Mohiuddin, A. Lombardo, R. R. Nair, A. Bonetti, G. Savini, R. Jalil, N. Bonini, D. M. Basko, C. Galiotis, N. Marzari, K. S. Novoselov, A. K. Geim, and A. C. Ferrari, “Uniaxial strain in graphene by Raman spectroscopy:  $G$  peak splitting, Grüneisen parameters, and sample orientation,” *Phys. Rev. B* **79**, 205433 (2009).
- [172] D. Yoon, Y.-W. Son, and H. Cheong, “Strain-dependent splitting of the double-resonance Raman scattering band in graphene,” *Phys. Rev. Lett.* **106**, 155502 (2011).
- [173] K. Hiroyuki, T. Ikari, W. Masao, T. Kazuya, K. Nao, I. Keisuke, and W. Hideki, “Proper understanding of down-shifted Raman spectra of natural graphite: Direct estimation of laser-induced rise in sample temperature,” *Geochim. Cosmochim. Acta* **58**, 3527 (1994).
- [174] P. H. Tan, Y. M. Deng, Q. Zhao, and W. C. Cheng, “The intrinsic temperature effect of the Raman spectra of graphite,” *Appl. Phys. Lett.* **74**, 1818 (1999).
- [175] N. Bonini, M. Lazzeri, N. Marzari, and F. Mauri, “Phonon anharmonicities in graphite and graphene,” *Phys. Rev. Lett.* **99**, 176802 (2007).
- [176] I. Calizo, A. A. Balandin, W. Bao, F. Miao, and C. N. Lau, “Temperature dependence of the Raman spectra of graphene and graphene multilayers,” *Nano Lett.* **7**, 2645 (2007).
- [177] D. Yoon, Y.-W. Son, and H. Cheong, “Negative thermal expansion coefficient of graphene measured by Raman spectroscopy,” *Nano Lett.* **11**, 3227 (2011).
- [178] S. Linas, Y. Magnin, B. Poinsot, O. Boisron, G. D. Förster, V. Martinez, R. Fulcrand, F. Tournus, V. Dupuis, F. Rabilloud, L. Bardotti, Z. Han, D. Kalita, V. Bouchiat, and F. Calvo, “Interplay between Raman shift and thermal expansion in graphene: Temperature-dependent measurements and analysis of substrate corrections,” *Phys. Rev. B* **91**, 075426 (2015).
- [179] A. B. Preobrajenski, M. L. Ng, A. S. Vinogradov, and N. Mårtensson, “Controlling graphene corrugation on lattice-mismatched substrates,” *Phys. Rev. B* **78**, 073401 (2008).
- [180] M.-C. Wu, Q. Xu, and D. W. Goodman, “Investigations of graphitic overlayers formed from methane decomposition on Ru(0001) and Ru(11 $\bar{2}$ 0) catalysts with scanning tunneling microscopy and high-resolution electron energy loss spectroscopy,” *J. Phys. Chem.* **98**, 5104 (1994).
- [181] D. Martoccia, P. R. Willmott, T. Brugger, M. Björck, S. Günther, C. M. Schlepütz, A. Cervellino, S. A. Pauli, B. D. Patterson, S. Marchini, J. Winterlin, W. Moritz, and T. Greber, “Graphene on Ru(0001): A  $25 \times 25$  supercell,” *Phys. Rev. Lett.* **101**, 126102 (2008).
- [182] B. Borca, F. Calleja, J. J. Hinarejos, A. L. Vázquez de Parga, and R. Miranda, “Reactivity of periodically rippled graphene grown on Ru(0001),” *J. Phys.: Condens. Matter* **21**, 134002 (2009).
- [183] E. Loginova, N. C. Bartelt, P. J. Feibelman, and K. F. McCarty, “Factors influencing graphene growth on metal surfaces,” *New J. Phys.* **11**, 063046 (2009).
- [184] Y. Cui, Q. Fu, H. Zhang, D. Tan, and X. Bao, “Dynamic characterization of graphene growth and etching by oxygen on Ru(0001) by photoemission electron microscopy,” *J. Phys. Chem. C* **113**, 20365 (2009).

- [185] D. Martoccia, M. Björck, C. M. Schlepütz, T. Brugger, S. A. Pauli, B. D. Patterson, T. Greber, and P. R. Willmott, “Graphene on Ru(0001): A corrugated and chiral structure,” *New J. Phys.* **12**, 043028 (2010).
- [186] B. Borca, S. Barja, M. Garnica, M. Minniti, A. Politano, J. M. Rodriguez-García, J. J. Hinarejos, D. Farías, A. L. Vázquez de Parga, and R. Miranda, “Electronic and geometric corrugation of periodically rippled, self-nanostructured graphene epitaxially grown on Ru(0001),” *New J. Phys.* **12**, 093018 (2010).
- [187] M. Gao, Y. Pan, C. Zhang, H. Hu, R. Yang, H. Lu, J. Cai, S. Du, F. Liu, and H.-J. Gao, “Tunable interfacial properties of epitaxial graphene on metal substrates,” *Appl. Phys. Lett.* **96**, 053109 (2010).
- [188] W. Moritz, B. Wang, M.-L. Bocquet, T. Brugger, T. Greber, J. Wintterlin, and S. Günther, “Structure determination of the coincidence phase of graphene on Ru(0001),” *Phys. Rev. Lett.* **104**, 136102 (2010).
- [189] S. Günther, S. Dänhardt, B. Wang, M.-L. Bocquet, S. Schmitt, and J. Wintterlin, “Single terrace growth of graphene on a metal surface,” *Nano Lett.* **11**, 1895 (2011).
- [190] S. Günther, S. Dänhardt, M. Ehrensperger, P. Zeller, S. Schmitt, and J. Wintterlin, “High-temperature scanning tunneling microscopy study of the ordering transition of an amorphous carbon layer into graphene on ruthenium(0001),” *ACS Nano* **7**, 154 (2013).
- [191] S. Marchini, S. Günther, and J. Wintterlin, “Scanning tunneling microscopy of graphene on Ru(0001),” *Phys. Rev. B* **76**, 075429 (2007).
- [192] Y. Pan, D.-X. Shi, and H.-J. Gao, “Formation of graphene on Ru(0001) surface,” *Chin. Phys.* **16**, 3151 (2007).
- [193] P. W. Sutter, J.-I. Flege, and E. A. Sutter, “Epitaxial graphene on ruthenium,” *Nat. Mater.* **7**, 406 (2008).
- [194] Y. Pan, H. Zhang, D. Shi, J. Sun, S. Du, F. Liu, and H. Gao, “Highly ordered, millimeter-scale, continuous, single-crystalline graphene monolayer formed on Ru (0001),” *Adv. Mater.* **21**, 2777 (2009).
- [195] E. Starodub, S. Maier, I. Stass, N. C. Bartelt, P. J. Feibelman, M. Salmeron, and K. F. McCarty, “Graphene growth by metal etching on Ru(0001),” *Phys. Rev. B* **80**, 235422 (2009).
- [196] K. F. McCarty, P. J. Feibelman, E. Loginova, and N. C. Bartelt, “Kinetics and thermodynamics of carbon segregation and graphene growth on Ru(0001),” *Carbon* **47**, 1806 (2009).
- [197] Y. Cui, Q. Fu, D. Tan, and X. Bao, “Temperature dependence of the formation of graphene and subsurface carbon on Ru(0001) and its effect on surface reactivity,” *ChemPhysChem* **11**, 995 (2010).
- [198] E. Loginova, N. C. Bartelt, P. J. Feibelman, and K. F. McCarty, “Evidence for graphene growth by C cluster attachment,” *New J. Phys.* **10**, 093026 (2008).
- [199] B. Wang, M.-L. Bocquet, S. Marchini, S. Gunther, and J. Wintterlin, “Chemical origin of a graphene moire overlayer on Ru(0001),” *Phys. Chem. Chem. Phys.* **10**, 3530 (2008).

- [200] B. Wang and M.-L. Bocquet, “Interfacial coupling in rotational monolayer and bilayer graphene on Ru(0001) from first principles,” *Nanoscale* **4**, 4687 (2012).
- [201] E. Sutter, B. Wang, P. Albrecht, J. Lahiri, M.-L. Bocquet, and P. Sutter, “Templating of arrays of Ru nanoclusters by monolayer graphene/Ru moirés with different periodicities,” *J. Phys.: Condens. Matter* **24**, 314201 (2012).
- [202] M. Iannuzzi and J. Hutter, “Comparative study of the nature of chemical bonding of corrugated graphene on Ru(0001) and Rh(111) by electronic structure calculations,” *Surf. Sci.* **605**, 1360 (2011).
- [203] M. Iannuzzi, I. Kalichava, H. Ma, S. J. Leake, H. Zhou, G. Li, Y. Zhang, O. Bunk, H. Gao, J. Hutter, P. R. Willmott, and T. Greber, “Moiré beatings in graphene on Ru(0001),” *Phys. Rev. B* **88**, 125433 (2013).
- [204] A. L. Vázquez de Parga, F. Calleja, B. Borca, M. C. G. Passeggi, J. J. Hinarejos, F. Guinea, and R. Miranda, “Periodically rippled graphene: Growth and spatially resolved electronic structure,” *Phys. Rev. Lett.* **100**, 056807 (2008).
- [205] D. Jiang, M.-H. Du, and S. Dai, “First principles study of the graphene/Ru(0001) interface,” *J. Chem. Phys.* **130**, 074705 (2009).
- [206] B. Wang, S. Günther, J. Wintterlin, and M.-L. Bocquet, “Periodicity, work function and reactivity of graphene on Ru(0001) from first principles,” *New J. Phys.* **12**, 043041 (2010).
- [207] E. Sutter, P. Albrecht, and P. Sutter, “Graphene growth on polycrystalline Ru thin films,” *Appl. Phys. Lett.* **95**, 133109 (2009).
- [208] E. Sutter, D. P. Acharya, J. T. Sadowski, and P. Sutter, “Scanning tunneling microscopy on epitaxial bilayer graphene on ruthenium (0001),” *Appl. Phys. Lett.* **94**, 133101 (2009).
- [209] P. Sutter, M. S. Hybertsen, J. T. Sadowski, and E. Sutter, “Electronic structure of few-layer epitaxial graphene on Ru(0001),” *Nano Lett.* **9**, 2654 (2009).
- [210] Y. Cui, Q. Fu, and X. Bao, “Dynamic observation of layer-by-layer growth and removal of graphene on Ru(0001),” *Phys. Chem. Chem. Phys.* **12**, 5053 (2010).
- [211] X. Peng and R. Ahuja, “Epitaxial graphene monolayer and bilayers on Ru(0001): *Ab initio* calculations,” *Phys. Rev. B* **82**, 045425 (2010).
- [212] M. Papagno, D. Pacilé, D. Topwal, P. Moras, P. M. Sheverdyaeva, F. D. Natterer, A. Lehnert, S. Rusponi, Q. Dubout, F. Calleja, E. Frantzeskakis, S. Pons, J. Fujii, I. Vobornik, M. Grioni, C. Carbone, and H. Brune, “Two distinct phases of bilayer graphene films on Ru(0001),” *ACS Nano* **6**, 9299 (2012).
- [213] M. I. Baskes and R. A. Johnson, “Modified embedded atom potentials for HCP metals,” *Modell. Simul. Mater. Sci. Eng.* **2**, 147 (1994).
- [214] W. Hu, B. Zhang, B. Huang, F. Gao, and D. J. Bacon, “Analytic modified embedded atom potentials for HCP metals,” *J. Phys.: Condens. Matter* **13**, 1193 (2001).
- [215] J. H. Li, L. T. Kong, and B. X. Liu, “Proposed definition of microchemical inhomogeneity and application to characterize some selected miscible/immiscible binary metal systems,” *J. Phys. Chem. B* **108**, 16071 (2004).

- [216] J. H. Li, H. B. Guo, L. T. Kong, and B. X. Liu, "Metastable isomorphous phase diagram of the peritectic Ni-Ru system predicted by *ab initio* and molecular dynamics calculations," *Phys. Rev. B* **71**, 014107 (2005).
- [217] X. He, S.-H. Liang, J.-H. Li, and B.-X. Liu, "Atomistic mechanism of interfacial reaction and asymmetric growth kinetics in an immiscible Cu-Ru system at equilibrium," *Phys. Rev. B* **75**, 045431 (2007).
- [218] A. Fortini, M. I. Mendeleev, S. Buldyrev, and D. Srolovitz, "Asperity contacts at the nanoscale: Comparison of Ru and Au," *J. Appl. Phys.* **104**, 074320 (2008).
- [219] B. Lin, K. Wei, J. Ni, and J. Lin, "KOH activation of thermally modified carbon as a support of Ru catalysts for ammonia synthesis," *ChemCatChem* **5**, 1941 (2013).
- [220] Y. Gao, K. Xie, S. Mi, N. Liu, W. Wang, and W. Huang, "Preferential oxidation of CO in a H<sub>2</sub>-rich stream over multi-walled carbon nanotubes confined Ru catalysts," *Int. J. Hydrogen Energy* **38**, 16665 (2013).
- [221] M. Gopiraman, B. S. Ganesh Babu, Z. Khatri, W. Kai, Y. A. Kim, M. Endo, R. Karvembu, and I. S. Kim, "Dry synthesis of easily tunable nano ruthenium supported on graphene: Novel nanocatalysts for aerial oxidation of alcohols and transfer hydrogenation of ketones," *J. Phys. Chem. C* **117**, 23582 (2013).
- [222] B. Wang and M.-L. Bocquet, "Monolayer graphene and h-BN on metal substrates as versatile templates for metallic nanoclusters," *J. Phys. Chem. Lett.* **2**, 2341 (2011).
- [223] D. Tománek, A. A. Aligia, and C. A. Balseiro, "Calculation of elastic strain and electronic effects on surface segregation," *Phys. Rev. B* **32**, 5051 (1985).
- [224] R. S. DaBell, R. G. Meyer, and M. D. Morse, "Electronic structure of the 4d transition metal carbides: Dispersed fluorescence spectroscopy of MoC, RuC, and PdC," *J. Chem. Phys.* **114**, 2938 (2001).
- [225] R. Guo and K. Balasubramanian, "Spectroscopic properties and potential energy curves of low-lying electronic states of RuC," *J. Chem. Phys.* **120**, 7418 (2004).
- [226] E. Zhao, J. Wang, and Z. Wu, "Structural stability and phase transition in OsC and RuC," *J. Comput. Chem.* **31**, 2883 (2010).
- [227] H. Gao and J. Zhao, "First-principles study of Ru atoms and clusters adsorbed outside and inside carbon nanotubes," *J. Chem. Phys.* **132**, 234704 (2010).
- [228] A. Ishii, M. Yamamoto, H. Asano, and K. Fujiwara, "DFT calculation for adatom adsorption on graphene sheet as a prototype of carbon nanotube functionalization," *J. Phys.: Conf. Ser.* **100**, 052087 (2008).
- [229] K. Nakada and A. Ishii, "Migration of adatom adsorption on graphene using DFT calculation," *Solid State Commun.* **151**, 13 (2011).
- [230] K. L. Man and M. S. Altman, "Small-angle lattice rotations in graphene on Ru(0001)," *Phys. Rev. B* **84**, 235415 (2011).

- [231] R. M. Nielsen, S. Murphy, C. Strebel, M. Johansson, J. H. Nielsen, and I. Chorkendorff, "A comparative STM study of Ru nanoparticles deposited on HOPG by mass-selected gas aggregation versus thermal evaporation," *Surf. Sci.* **603**, 3420 (2009).
- [232] E. H. Martins Ferreira, M. V. O. Moutinho, F. Stavale, M. M. Lucchese, R. B. Capaz, C. A. Achete, and A. Jorio, "Evolution of the Raman spectra from single-, few-, and many-layer graphene with increasing disorder," *Phys. Rev. B* **82**, 125429 (2010).
- [233] E. Sutter, P. Albrecht, B. Wang, B. M.-L., W. L., Z. Y., and S. P., "Arrays of Ru nanoclusters with narrow size distribution templated by monolayer graphene on Ru," *Surf. Sci.* **605**, 1676 (2011).
- [234] B. Wang, B. Yoon, M. König, Y. Fukamori, F. Esch, U. Heiz, and U. Landman, "Size-selected monodisperse nanoclusters on supported graphene: Bonding, isomerism, and mobility," *Nano Lett.* **12**, 5907 (2012).
- [235] N. Atodiresei, "Private communications," (2014).
- [236] F. Jean, T. Zhou, N. Blanc, R. Felici, J. Coraux, and G. Renaud, "Topography of the graphene/Ir(111) moiré studied by surface x-ray diffraction," *Phys. Rev. B* **91**, 245424 (2015).
- [237] H. Amara, J.-M. Roussel, C. Bichara, J.-P. Gaspard, and F. Ducastelle, "Tight-binding potential for atomistic simulations of carbon interacting with transition metals: Application to the NI-C system," *Phys. Rev. B* **79**, 014109 (2009).
- [238] S. Karoui, H. Amara, C. Bichara, and F. Ducastelle, "Nickel-assisted healing of defective graphene," *ACS Nano* **4**, 6114 (2010).
- [239] S. Haghighatpanah, A. Börjesson, H. Amara, C. Bichara, and K. Bolton, "Computational studies of graphene growth mechanisms," *Phys. Rev. B* **85**, 205448 (2012).
- [240] R. S. Weatherup, H. Amara, R. Blume, B. Dlubak, B. C. Bayer, M. Diarra, M. Bahri, A. Cabrero-Vilatela, S. Caneva, P. R. Kidambi, M.-B. Martin, C. Deranlot, P. Seneor, R. Schloegl, F. Ducastelle, C. Bichara, and S. Hofmann, "Interdependency of subsurface carbon distribution and graphene-catalyst interaction," *J. Am. Chem. Soc.* **136**, 13698 (2014).
- [241] H. Amara, C. Bichara, and F. Ducastelle, "Understanding the nucleation mechanisms of carbon nanotubes in catalytic chemical vapor deposition," *Phys. Rev. Lett.* **100**, 056105 (2008).
- [242] Y. Murata, V. Petrova, B. B. Kappes, A. Ebnonnasir, I. Petrov, Y.-H. Xie, C. V. Ciobanu, and S. Kodambaka, "Moiré superstructures of graphene on faceted nickel islands," *ACS Nano* **4**, 6509 (2010).
- [243] J. Coraux, A. T. N'Diaye, M. Engler, C. Busse, D. Wall, N. Buckanie, F.-J. M. Meyer zu Heringdorf, R. van Gastel, B. Poelsema, and T. Michely, "Growth of graphene on Ir(111)," *New J. Phys.* **11**, 023006 (2009).
- [244] E. Starodub, A. Bostwick, L. Moreschini, S. Nie, F. E. Gabaly, K. F. McCarty, and E. Rotenberg, "In-plane orientation effects on the electronic structure, stability, and Raman scattering of monolayer graphene on Ir(111)," *Phys. Rev. B* **83**, 125428 (2011).

- [245] F. Jean, T. Zhou, N. Blanc, R. Felici, J. Coraux, and G. Renaud, “Effect of preparation on the commensurabilities and thermal expansion of graphene on Ir(111) between 10 and 1300 K,” *Phys. Rev. B* **88**, 165406 (2013).
- [246] C. Busse, P. Lazić, R. Djemour, J. Coraux, T. Gerber, N. Atodiresei, V. Caciuc, R. Brako, A. T. N’Diaye, S. Blügel, J. Zegenhagen, and T. Michely, “Graphene on Ir(111): Physisorption with chemical modulation,” *Phys. Rev. Lett.* **107**, 036101 (2011).
- [247] J. Knudsen, P. J. Feibelman, T. Gerber, E. Grånäs, K. Schulte, P. Stratmann, J. N. Andersen, and T. Michely, “Clusters binding to the graphene moiré on Ir(111): X-ray photoemission compared to density functional calculations,” *Phys. Rev. B* **85**, 035407 (2012).
- [248] Z. Sun, S. K. Hämäläinen, J. Sainio, J. Lahtinen, D. Vanmaekelbergh, and P. Liljeroth, “Topographic and electronic contrast of the graphene moiré on Ir(111) probed by scanning tunneling microscopy and noncontact atomic force microscopy,” *Phys. Rev. B* **83**, 081415 (2011).
- [249] S. K. Hämäläinen, M. P. Boneschanscher, P. H. Jacobse, I. Swart, K. Pussi, W. Moritz, J. Lahtinen, P. Liljeroth, and J. Sainio, “Structure and local variations of the graphene moiré on Ir(111),” *Phys. Rev. B* **88**, 201406 (2013).
- [250] Y. Gamo, A. Nagashima, M. Wakabayashi, M. Terai, and C. Oshima, “Atomic structure of monolayer graphite formed on Ni(111),” *Surf. Sci.* **374**, 61 (1997).
- [251] J. Wang, X. Sun, and Z. Wu, “Theoretical investigation of 5d-metal monocarbides,” *J. Cluster Sci.* **18**, 333 (2007).
- [252] A. F. Guillermet, J. Häglund, and G. Grimvall, “Cohesive properties and electronic structure of 5 *d* -transition-metal carbides and nitrides in the NaCl structure,” *Phys. Rev. B* **48**, 11673 (1993).
- [253] D. W. Brenner, “The art and science of an analytic potential,” *Phys. Status Solidi B* **217**, 23 (2000).
- [254] F. Jean, T. Zhou, N. Blanc, R. Felici, J. Coraux, and G. Renaud, “Erratum: Effect of preparation on the commensurabilities and thermal expansion of graphene on Ir(111) between 10 and 1300 K [Phys. Rev. B **88** , 165406 (2013)],” *Phys. Rev. B* **90**, 239901 (2014).
- [255] F. Mittendorfer, A. Garhofer, J. Redinger, J. Klimeš, J. Harl, and G. Kresse, “Graphene on Ni(111): Strong interaction and weak adsorption,” *Phys. Rev. B* **84**, 201401 (2011).
- [256] Y. S. Dedkov and M. Fonin, “Electronic and magnetic properties of the graphene–ferromagnet interface,” *New J. Phys.* **12**, 125004 (2010).
- [257] J. A. Elliott, Y. Shibuta, H. Amara, C. Bichara, and E. C. Neyts, “Atomistic modelling of CVD synthesis of carbon nanotubes and graphene,” *Nanoscale* **5**, 6662 (2013).
- [258] W. Zhao, S. M. Kozlov, O. Höfert, K. Gotterbarm, M. P. A. Lorenz, F. Viñes, C. Papp, A. Görling, and H.-P. Steinrück, “Graphene on Ni(111): Coexistence of different surface structures,” *J. Phys. Chem. Lett.* **2**, 759 (2011).

- [259] A. Dahal and M. Batzill, “Graphene-nickel interfaces: A review,” *Nanoscale* **6**, 2548 (2014).
- [260] J. H. Los, C. Bichara, and R. J. M. Pellenq, “Tight binding within the fourth moment approximation: Efficient implementation and application to liquid Ni droplet diffusion on graphene,” *Phys. Rev. B* **84**, 085455 (2011).
- [261] J. C. Slater and G. F. Koster, “Simplified LCAO method for the periodic potential problem,” *Phys. Rev.* **94**, 1498 (1954).
- [262] M. P. Zach and R. M. Penner, “Nanocrystalline nickel nanoparticles,” *Adv. Mater.* **12**, 878 (2000).
- [263] J. Lahiri and M. Batzill, “Graphene destruction by metal-carbide formation: An approach for patterning of metal-supported graphene,” *Appl. Phys. Lett.* **97**, 023102 (2010).
- [264] J. Lahiri, T. S. Miller, A. J. Ross, L. Adamska, I. I. Oleynik, and M. Batzill, “Graphene growth and stability at nickel surfaces,” *New J. Phys.* **13**, 025001 (2011).
- [265] L. Ci, Z. Xu, L. Wang, W. Gao, F. Ding, K. F. Kelly, B. I. Yakobson, and P. M. Ajayan, “Controlled nanocutting of graphene,” *Nano Res.* **1**, 116 (2008).
- [266] P. J. Hoogerbrugge and J. M. V. A. Koelman, “Simulating microscopic hydrodynamic phenomena with dissipative particle dynamics,” *Europhys. Lett.* **19**, 155 (1992).
- [267] W. Liu, J. Carrasco, B. Santra, A. Michaelides, M. Scheffler, and A. Tkatchenko, “Benzene adsorbed on metals: Concerted effect of covalency and van der Waals bonding,” *Phys. Rev. B* **86**, 245405 (2012).



## **Modélisation atomique de nanoparticules métalliques sur substrats carbonés et graphène épitaxié sur métaux**

Les applications des nanoparticules métalliques nécessitent des assemblées monodisperses et stables sur un substrat tel que le graphène ou le graphite. Le graphène épitaxié sur métal (GEM) est étudié, car il facilite l'auto-organisation des adsorbats. La différence entre les mailles du graphène et du métal conduit à un effet de moiré contenant certaines régions favorables de l'adsorption. Ce travail est consacré surtout aux systèmes Ru-C et Pt-C où nous sommes intéressés au substrat du GEM nu, des agrégats y étant déposés et des agrégats métalliques sur graphite.

Les potentiels d'ordre de liaison permettent de mener des études en dynamique moléculaire sur des systèmes de taille réaliste à température finie. Dans le cas du système Pt-C une paramétrisation est disponible dans la littérature. Cependant, pour le système du Ru-C une paramétrisation sur la base de données DFT était nécessaire. Ce modèle atomistique néglige les forces de dispersion importantes pour des milieux étendus. Basé sur les modèles de Grimme, nous avons développé une description implicite tenant compte de la structure du substrat et son extension semi-infinie. De plus les effets d'écrantage importants pour des milieux métalliques sont pris en compte.

Basé sur ce champ de force nous montrons des propriétés des adsorbats sur des substrats carbonés où nous évaluons le modèle de forces de dispersion. Grâce à des simulations de dynamique moléculaire, la stabilité des adsorbats et du graphène a été étudiée dans le contexte de la dynamique vibrationnelle et de diffusion. En accord avec les expériences, la mobilité des adsorbats sur graphite s'avère élevée en comparaison avec des adsorbats sur GEM.

## **Atomistic modeling of metallic nanoparticles on carbonaceous substrates and epitaxial graphene on metals**

Applications of metal nanoparticles require monodisperse and stable assemblies on a substrate such as graphene or graphite. Epitaxial graphene on metal (GOM) has attracted research interest because it contributes to the self-organisation of adsorbates. The difference in the lattice constants of graphene and metal leads to a moiré that contains certain regions that are favorable for adsorption. This work is mainly concerned with the Ru-C and Pt-C systems where we were interested in the bare substrate of GOM, adsorbates deposited thereon and metal clusters on graphite.

Bond order potentials allow to carry out molecular dynamics studies for systems of realistic size and at finite temperature. In the case of the Pt-C, a parametrization is available in the literature. However, for Ru-C systems a custom parametrization effort based on data from electronic structure calculations was necessary. This atomistic model neglects long ranged dispersion forces that are important for adsorption phenomena on extended substrates. Based on the Grimme models, we developed an implicit description that takes the layered structure and the semi-infinite extension of the substrate into account. Also, screening effects that are important for metal materials are taken into account.

Based on this force field, we show results concerning the properties of adsorbates on carbon substrates while evaluating the dispersion model. With the help of molecular dynamics simulations, the stability of adsorbates and graphene has been studied in the context of vibrational and diffusion dynamics. In agreement with experiments, the mobility of the adsorbates on graphite is high in comparison with adsorbates on GOM.